RAPIDITY GAPS BETWEEN JETS IN $p\bar{p}$ COLLISIONS AT $\sqrt{s} = 1.8$ TeV

by

Brent Joseph May

A Dissertation Submitted to the Faculty of the

DEPARTMENT OF PHYSICS

In Partial Fulfillment of the Requirements
For the Degree of

DOCTOR OF PHILOSOPHY

In the Graduate College

THE UNIVERSITY OF ARIZONA

1 9 9 4

(Final Examining Committee Approval Form)

STATEMENT BY AUTHOR

This dissertation has been submitted in partial fulfillment of requirements for an advanced degree at The University of Arizona and is deposited in the University Library to be made available to borrowers under rules of the Library.

Brief quotations from this dissertation are allowable without special permission, provided that accurate acknowledgement of source is made. Requests for permission for extended quotation from or reproduction of this manuscript in whole or in part may be granted by the head of the major department or the Dean of the Graduate College when in his or her judgement the proposed use of the material is in the interests of scholarship. In all other instances, however, permission must be obtained from the author.

SIGNED: _____

ACKNOWLEDGEMENTS

I greatly appreciate the support of the many people who have made this dissertation possible. In particular, I would like to thank my advisor Geoff Forden, who hired me as a starving grad student, provided support and advice, and allowed me the freedom to pursue my own physics interests. I also must thank my fellow rap gapper Andrew Brandt, who throughout provided advice, support, and friendship. Andrew and I formed an impressive analysis team and published the first paper on this topic. I also greatly appreciate the help of Tracy Taylor, who is certainly more than qualified to take the reigns of the analysis. In addition, I wish to extend my gratitude to the faculty, staff, and students in the EEPP group at the University Arizona for their support and assistance. I am also indebted to the multitude of people at DØ who designed, built, and ran the detector, and without their work this dissertation would not have been possible.

I want to thank Harry Weerts for suggesting this topic to me, taking the time to listen to my concerns, and providing guidance. I also owe Jerry Blazey thanks for his support and advice, and for never leaving our heels while writing the PRL paper. I must acknowledge Paul Grannis for first supporting this novel analysis and having confidence in us. I also wish to thank many others in the QCD group who helped out, especially Rich Astur, Bob Kehoe and Daniel Elvira for their jet expertise. I appreciate the feedback of those who have witnessed the humble beginnings of the analysis and have seen it mature and grow beyond the scope of this dissertation.

I owe a special thanks to Ina Sarcevic and Bob Fletcher for their insight, advice, and many helpful discussions on the theoretical aspects of the analysis. I also thank Dieter Zeppenfeld, Vittorio Del Duca and Wai-Keung Tang for their suggestions and comments. I acknowledge James Bjorken for his insight into this topic and for encouraging DØ to pursue this analysis.

I greatly appreciate the support of my friends at DØ, especially Sal Fahey, Kathy Fatyga, Kate Frame, Terry Heuring, Bob Hirosky, Steve Jerger, and the football guys. I also must thank my best friends in Arizona, Steve Gilbert, Pete Scatena, Sidney, and Teva for their unconditional support and friendship. Finally, I wish to thank my family for their long-distance love and support, and my best friend Heather Hodel for enduring life with a sometimes trying graduate student.

To Heather.

TABLE OF CONTENTS

LIST OF FIGURES **11**

LIST OF TABLES **15**

ABSTRACT **16**

1 Introduction **17**

2 Theory **22**

2.1 The Quark-Parton Model 23

2.2 Perturbative QCD 26

2.2.1 The Running Coupling Constant 27

2.3 Jet and Particle Production 29

2.3.1 Hard Scattering 29

2.3.2 Parton Showering and Evolution 31

2.3.3 Color Coherence 32

2.3.4 Hadronization 35

2.3.5 Spectator Interactions 36

2.4 The Monte Carlo Event Generator 37

2.5 Theoretical and Experimental Conventions 38

2.5.1 Invariant Phase Space and Transverse Momentum 38

2.5.2 Jet Definition 39

2.6 Color and Particle Flow in Jet Events 41

2.6.1 The String Model 42
2.6.2 The Color Dipole Model 44
2.6.3 Strings and the Rapidity Plateau 46
2.7 Elastic and Diffractive Scattering: Rapidity Gaps 48
2.7.1 The Pomeron and Rapidity Gaps 49
2.7.2 The Hard Pomeron and Jet Production 50
2.7.3 Nondiffractive Inelastic Scattering 50
2.7.4 Minimum Bias Events 51
2.8 Rapidity Gaps in Hard Scattering 51
2.8.1 The Electroweak Color-Singlet Radiation Pattern 53
2.8.2 The QCD Color-Singlet Radiation Pattern 54
2.8.3 Out-of-cone Radiation in Color-Singlet Exchange 56
2.9 Rapidity Gap "Production" Rates 58
2.9.1 Electroweak Color-Singlet 59
2.9.2 QCD Color-Singlet 59
2.9.3 Color Octet/Triplet Production 60
2.9.4 Inclusive Gap Production 64
2.9.5 Spectator Interactions and Survival of the Gap 65
2.10 The Rapidity Gap Fraction 67
2.10.1 Qualitative Expectation 68
2.10.2 QCD Prediction 70

3 The DØ Experiment **74**
3.1 The Fermilab Tevatron $p\bar{p}$ Collider 74
3.2 The DØ Detector 76
3.2.1 The Central Detector 76
3.2.2 The Calorimeter 79
3.2.3 Massless Gaps and Inner Cryostat Detectors 88

3.2.4 DØGEANT Detector Simulator 89
3.2.5 The Trigger System 90

4 Jet Reconstruction 92

4.1 Vertex Position Measurement 92
4.2 The Cone Algorithm 94
4.3 Cone Algorithm Performance 96
4.4 Removal of Spurious Jets 97
4.5 Jet Energy Scale Correction 99
4.6 Jet Energy Resolution 104

5 Triggers and Data Selection 106

5.1 Jet Triggers 106
5.2 Description of Triggers 107
5.3 Trigger Sample 108
5.3.1 Dijet Trigger Efficiencies 113
5.3.2 Trigger Biases 115
5.4 Event Selection 118
5.4.1 Removal of Bad Data Runs 119
5.4.2 Removal of Events with Spurious Jets 119
5.4.3 Rejection of Multiple Interactions 119
5.4.4 Final Cuts and Data Sample 120

6 Experimental Rapidity Gap Definition and Sample 124

6.1 Tagging Particles with the Calorimeter 125
6.2 Tagging Efficiency 127
6.2.1 Test Beam Efficiency 127
6.2.2 DØGEANT Efficiency 129
6.2.3 Particle Response in Minimum Bias Events 129

6.2.4 Response to Noise 132
6.3 Removal of Noisy Calorimeter Channels 135
6.4 Experimental Rapidity Gap Sample 136
6.4.1 Comparison of Inclusive and Rapidity Gap Samples 137

7 Rapidity Gap Fraction Measurement 143
7.1 Experimental Rapidity Gap Fraction 143
7.1.1 "Inclusive" Gap Fraction Measurement 144
7.1.2 Uncorrected Experimental Gap Fraction 144
7.1.3 Interpretation of Experimental Gap Fraction 144
7.1.4 "Color-Octet" Gap Fraction Measurement 145
7.1.5 Upper Limit Considerations 147
7.2 Systematic Biases 147
7.2.1 Particle Tagging Inefficiency 148
7.2.2 Trigger Biases 150
7.2.3 Jet E_T Effects 153
7.2.4 Jet Reconstruction Biases 156
7.2.5 Multiple Interaction Contamination 158
7.2.6 Calorimeter Noise Contamination 159
7.2.7 Out-of-cone Effects 160
7.2.8 Summary of Biases 166

8 Results 168
8.1 Corrected Experimental Gap Fraction 168
8.2 Upper Limit 169
8.3 Interpretation of Upper Limit 170

9 Conclusions 171

A Possible Trigger Biases in the Gap Fraction Measurement **174**

A.1 Parton Distribution Functions 175

A.2 Trigger Biases 175

A.2.1 Level 1 Trigger Bias 176

A.2.2 High-$\Delta\eta$ Trigger η_{boost} Bias 178

REFERENCES **180**

LIST OF FIGURES

2-1 Parton distribution functions for the proton 25

2-2 Feynman diagram of quark scattering via exchange of a gluon 27

2-3 Behavior of the strong coupling constant $\alpha_s(Q)$ 28

2-4 Examples of LO (α_s^2) Feynman diagrams for jet production 30

2-5 Examples of NLO (α_s^3) Feynman diagrams for jet production 31

2-6 Schematic evolution of a parton shower 33

2-7 Angular ordering of parton radiation 35

2-8 The "string effect" in $e^+e^- \to q\bar{q}g$ 44

2-9 Examples of color flow in hard $p\bar{p}$ collisions 45

2-10 Single diffraction via Pomeron exchange 48

2-11 Color flow in a nondiffractive inelastic interaction 51

2-12 Color flow in hard scattering color-singlet exchange 52

2-13 Representation in η-ϕ space of the distribution of particles in a typical two-jet event containing a rapidity gap 53

2-14 Electroweak color-singlet radiation pattern 54

2-15 Radiation pattern from two-gluon Pomeron exchange 55

2-16 Angular ordering constraint on radiation as a function of η 57

2-17 Fraction of events with a rapidity gap from color-octet exchange 62

2-18 Fraction of events with a rapidity gap from large-angle quark scattering 63

2-19 Contributions to σ_{gap}/σ as a function of $\Delta\eta_c$ 64

2-20 Overlap of a proton and antiproton in impact parameter space 66

2-21 Behavior of $S(\Delta\eta_c)$ 68

2-22 Prediction for $f(\Delta\eta_c)$ with and without a QCD color-singlet 69
2-23 Effect of particle detection inefficiencies on $f(\Delta\eta_c)$ 70
2-24 The ratio $R(\Delta\eta_c, \mu)$ for several values of μ 73

3-1 The DØ Detector 77
3-2 The DØ Central Detector 78
3-3 Cutaway view of the DØ calorimeter 80
3-4 Cross sectional view of the calorimeter and central detector 82
3-5 Cross section of a typical calorimeter read-out cell 83
3-6 Pseudorapidity coverage of the calorimeter by section 85
3-7 Cross sectional view showing the ICD and MG detectors 89

4-1 Calorimeter jet response in the central region versus jet energy 102
4-2 Jet energy scale correction for $|\eta|$=0 and $|\eta|$=2.5 versus measured jet transverse energy 103
4-3 Jet energy resolution versus jet energy 105

5-1 E_T distributions of the two leading jets for the inclusive and high-$\Delta\eta$ triggers 110
5-2 The η distributions and η-ϕ scatter plot for the two leading jets from the inclusive trigger 111
5-3 The η distributions and η-ϕ scatter plot for the two leading jets from the high-$\Delta\eta$ trigger 112
5-4 The $\Delta\eta_c$ distributions for the inclusive and high-$\Delta\eta$ triggers 113
5-5 Fits to the jet E_T distributions of the inclusive and high-$\Delta\eta$ triggers . . 114
5-6 Approximate efficiencies for the inclusive and high-$\Delta\eta$ triggers 115
5-7 The ratio $\epsilon_{qq}/\epsilon_{gg}$ showing the bias towards qq dijet events with respect to gg dijet events as a function of parton p_T 117
5-8 The $|\eta_{boost}|$ distribution ($\Delta\eta_c > 2.6$) for inclusive and high-$\Delta\eta$ triggers . 118

5-9 Behavior of the level 0 single-interaction cut versus instantaneous luminosity 121
5-10 The z-vertex and $|\eta_{boost}|$ distributions for the inclusive and high-$\Delta\eta$ triggers 122
5-11 The $\Delta\eta_c$ distribution for the final combined data sample 123

6-1 Test beam and DØGEANT electron and pion tagging efficiencies . . . 128
6-2 Distribution of tagged particles in minimum bias events versus η_d . . . 130
6-3 Tagged particle multiplicity of noise runs with no beam 134
6-4 Tagged particle multiplicity of a noise run with beam 134
6-5 EM calorimeter tower occupancy showing "hot" towers 136
6-6 Number of events versus $\Delta\eta_c$ for the total inclusive dijet sample and the subset with an experimental rapidity gap 137
6-7 Detector event display of an event from the rapidity gap sample 139
6-8 Calorimeter η-ϕ "E_T lego" of an event from the rapidity gap sample . . 140
6-9 Detector event display of a typical jet event 141
6-10 Calorimeter η-ϕ "E_T lego" of a typical jet event 141
6-11 Number of hadronic towers and charged tracks for gap events and inclusive events with $\Delta\eta_c > 3$ 142
6-12 Number of jets and the $d\phi$ distribution for for the rapidity gap sample and inclusive sample for $\Delta\eta_c < 3$ 142

7-1 Uncorrected experimental rapidity gap fraction 145
7-2 Experimental gap fraction compared to the "color-octet" gap fraction . 146
7-3 Dependence of the experimental rapidity gap fraction on particle tagging threshold 149
7-4 The $\Delta\eta_c$ acceptance for the high-$\Delta\eta$ trigger 151
7-5 Experimental rapidity gap fraction from the combined final data sample compared to that from the inclusive trigger only 152

7-6 Rapidity gap fraction measurement versus jet E_T 153
7-7 Enchancement in multijet multiplicity for events with $E_{T_2} > 20\,\mathrm{GeV}$ . . 155
7-8 Effect on the measured rapidity gap fraction of the lower E_T requirement on the second leading jet, and the dependence on number of jets . 156
7-9 Effect of spurious jet contamination on the measured gap fraction . . . 158
7-10 Effect of multiple interaction contamination on measured gap fraction . 159
7-11 "Out-of-cone" and "away-cone" gap η-ϕ topology 161
7-12 Effect of excluding "out-of-cone" and "away-cone" tagged particles on the measured gap fraction 162
7-13 Effect of the "out-of-cone" and "away-cone" gap topologies on the measured gap fraction 163
7-14 Expected behavior of the contributions to the out-of-cone effect 164
7-15 Event topology used to determine detector out-of-cone effect 165
7-16 Out-of-cone effect as a function of cone radius for $\Delta\eta_c > 3$ 166

8-1 Upper limit on the gap fraction compared to theoretical predictions . . 170

A-1 Ratio of quarks to gluons as a function of $\Delta\eta_c$ for a single jet 176
A-2 Effect of a quark bias on measured gap fraction as a function of $\Delta\eta_c$ . . 177
A-3 Maximum effect of a quark bias on the measured gap fraction 178
A-4 Effect of η_{boost} on the measured gap fraction 179

LIST OF TABLES

3-1 Calorimeter pedestal noise widths 87

5-1 Statistics of the final data sample 123

6-1 Dispersion in η of tagged particles in the calorimeter 132

6-2 Estimated dispersion in η of tagged particles in the forward region . . . 132

6-3 Number of events in gap and inclusive samples as a function of $\Delta\eta_c$ . . 138

7-1 Estimated tagging efficiencies for various EM tower thresholds 150

7-2 Fractional difference between the nominal gap fraction measurement and the measurement binned in jet E_T 154

7-3 Systematic biases in the measurement of the rapidity gap fraction . . . 167

8-1 Systematic biases affecting the upper limit on the rapidity gap fraction 169

ABSTRACT

Experimental results are presented from a search for events with a rapidity gap between high transverse momentum jets produced by the Fermilab Tevatron $p\bar{p}$ Collider at $\sqrt{s} = 1.8$ TeV. The DØ detector is used to obtain a sample of events with no observed particles between the two highest transverse energy jets above 30 GeV using an experimental rapidity gap definition. This sample is used to measure the fraction of events with an observed rapidity gap between the jets as a function of the pseudorapidity separation between the jet cone edges ($\Delta\eta_c$). The observed rapidity gap fraction is in qualitative agreement with theoretical expectations for color-singlet exchange, but uncertainties in the color-octet contribution and the background from particle detection inefficiencies make this association difficult. The measured gap fraction is used to place an upper limit at the 95% confidence level of 1.1×10^{-2} on the fraction of events with no particles between the jets for events with $\Delta\eta_c > 3$. This limit puts a significant constraint on the cross section for rapidity gap production between jets (color-singlet exchange) and the probability of a rapidity gap surviving spectator interactions.

Chapter 1

Introduction

Jets, or collimated sprays of hadrons, have been routinely observed in high energy collisions ever since their discovery in e^+e^- experiments nearly 20 years ago. Jet production has provided a very useful tool for probing the smallest known constituents of hadronic matter—the quarks and gluons—and their interactions. Since jets are the observable remnants of these "partons" (parts of hadrons), understanding jet production can give insight into the unobservable quarks and gluons. Quantum chromodynamics (QCD), or the theory of strong interactions, is presently believed to describe the interactions of partons.

Many aspects of jet production at hadron-hadron colliders have been predicted or verified by quantum chromodynamics. Measurements of jet cross sections, angular distributions, and other related quantities have confirmed in part the validity of quantum chromodynamics as a description for hard scattering processes. Unfortunately, many of the details of final-state particle production or "hadronization" in jet events can be quantitatively predicted only by empirical models. These models, based on experimental observation, predict substantial final-state particle production in the region between final-state jets. There may exist, however, a hard scattering process with a unique "hadronization" pattern in which the region between the jets is totally devoid of particles.

Rapidity gaps, namely large regions of rapidity containing no particles, have

typically been associated with low transverse momentum processes such as elastic and diffractive scattering. Rapidity gaps have also recently been observed in deep inelastic scattering events [1]. However, they are also expected to occur in high transverse momentum processes when a color singlet is exchanged between interacting partons [2, 3]. These gaps are believed to occur between final-state high transverse momentum jets due to the absence of gluon radiation from the exchanged color singlet and the resulting destructive interference between initial and final-state radiation [4, 5]. Hadrons are produced only between an outgoing jet and its associated hadron remnant (parent hadron), resulting in an unpopulated region of phase space between the jets.

The exchange of a electroweak gauge boson (photon, $W^{\pm}$ or Z^0) is expected to give such an event topology. In addition, a hard Pomeron, which has been shown to be associated with jet production [6], is a color singlet which is expected to produce rapidity gaps. Although QCD interactions (quark or gluon exchange) typically produce particles between jets due to the exchange of color, rapidity gaps can also arise from fluctuations in the particle multiplicity.

A rapidity gap will not be observed in the final state, however, if spectator interactions produce particles between the jets. These additional interactions occur frequently due to the large overlap of the colliding hadrons. The resulting hadronization from these interactions can produce particles between the jets and obscure rapidity gaps.

While both the cross section for producing a rapidity gap from the hard scattering and the probability of a rapidity gap surviving spectator interactions are of theoretical interest, experiments are directly sensitive to the product of these factors. One quantity that is both theoretically and experimentally accessible is the *rapidity gap fraction* [7], which is the fraction of events with a rapidity gap between the jets measured as a function of jet separation.

Realistically, however, direct measurement of the rapidity gap fraction is quite difficult due to the intrinsic particle detection inefficiencies of a real detector. Since some particles will not be observed due to imperfect detection efficiency, some events will erroneously be counted as rapidity gap events. Thus an experimental measurement of the gap fraction is necessarily an upper limit on the fraction of events with no particles between jets.

In order to make a meaningful experimental measurement of the rapidity gap fraction and resulting upper limit, the experiment must satisfy three conditions. First, the detector must be able to trigger on high transverse momentum jets and measure their transverse energy. Second, the detector should have sufficient pseudorapidity coverage to allow large pseudorapidity separations between the jets. Finally, the detector must be able to tag or detect particles between the jets with a reasonable efficiency. A reasonable efficiency is one that provides an upper limit that is significant in terms of the existing theory.

The DØ detector is well suited for this measurement and is used to obtain an upper limit on the rapidity gap fraction. In this dissertation, an *experimental rapidity gap fraction* is measured by defining a rapidity gap as the absence of *tagged* (detected) particles between the two highest transverse energy jets. This measurement is then used to place an upper limit on the fraction of events with *no particles* between the jets. The resulting limit is shown to put a significant constraint on the existing theoretical predictions [3, 8].

Overview of Dissertation

The subsequent chapters of this dissertation describe in detail the theoretical motivation for the rapidity gap fraction measurement and the experimental methodology used to determine an upper limit on the rapidity gap fraction. This work expands upon the measurement previously published by the DØ Collaboration in

Ref. [7]. A short description of each chapter is given below.

Chapter 2 explains the theoretical motivation for the rapidity gap fraction measurement. First, a description of QCD is given to introduce the concepts of jet production and hadronization in hadron-hadron interactions. Color flow and particle flow in jet events is described in terms of several different models, and rapidity gap production in jet events is motivated in terms of the color flow in these events. The various contributions to rapidity gap production between jets are discussed and theoretical predictions are given. The extended detail of this chapter is designed to provide a comprehensive compilation of the current theoretical understanding of rapidity gap production between jets.

Chapter 3 describes the DØ detector and trigger system with particular emphasis on those elements essential to the gap fraction measurement. The calorimeter is discussed in detail since it is used to measure jets and search for rapidity gap events.

Chapter 4 discusses jet measurement at DØ. The jet reconstruction algorithm and transverse energy measurement in the calorimeter are explained, and the jet reconstruction performance, jet energy scale correction, and jet energy resolution are discussed.

Chapter 5 describes the selection of the data sample used for the gap fraction measurement. The specific trigger conditions, efficiencies, biases, and final selection criteria for the gap fraction measurement are also discussed.

Chapter 6 describes the method of searching for rapidity gap events by tagging particles in the calorimeter, since a rapidity gap is defined as the absence of tagged particles between the jets. The particle tagging efficiency is given and the impact of noise on this method is discussed. The final selection cuts for the rapidity gap subsample are described, and this subsample is compared to the inclusive sample.

Chapter 7 describes the rapidity gap fraction measurement and the system-

atic biases associated with the measurement. The dependence on particle tagging definition, offline cuts, and jet transverse energy is discussed. In addition, effects that contaminate rapidity gap events (such as noise and jet out-of-cone effects) are examined in detail, since these effects can artificially reduce the experimental gap fraction measurement. The gap fraction measurement is compared to a sample of events that contains a highly suppressed color-singlet contribution. The difference in the shape of the gap fraction between these samples is suggestive of observation of a color-singlet exchange process in the inclusive gap fraction measurement.

Chapter 8 discusses how the experimental gap fraction measurement is used to place an upper limit calculation on the fraction of events with no particles between the jets. The systematic errors and corrections needed for the upper limit calculation are discussed, and the upper limit is compared to the current theoretical predictions. This limit is shown to put a significant constraint on these predictions.

Chapter 9 summarizes the most important results in this dissertation and reflects on their meaning and significance.

Chapter 2

Theory

High energy elementary particle physics is the study of fundamental particles and their interactions. While the ultimate goal of obtaining a grand unified theory has not yet been achieved, high energy physics has made many contributions to the understanding of the universe and its creation.

In particular, the standard model of electroweak interactions has had great success in the calculation of various production cross sections, branching ratios and other measurable quantities. Although some parameters of the theory are "free" and must be determined from experiment, the outstanding accuracy of the calculations and predictions arises from the small value of the electroweak coupling constants. Perturbative expansions converge very quickly to accurate and verifiable predictions.

In contrast, quantum chromodynamics (QCD), or the theory of strong interactions, is beset with many unanswered questions. The nature of the strong coupling makes perturbative expansions less accurate and applicable only in "high" momentum transfer regimes. Although particle masses and strong decay rates have been calculated recently using lattice QCD, final-state hadronic particle production cannot currently be calculated. However, perturbative QCD, in combination with phenomenological models, yields good predictions for jet production cross sections and other measurable quantities.

This chapter introduces the ideas and methods of QCD in relation to jet and particle production in proton-antiproton collisions. First, the quark-parton model and the principle of factorization in hadron-hadron collisions are introduced. Next, perturbative QCD is discussed in relation to jet production. The hadronization of jets is also discussed in terms of perturbative QCD and the string model. Color flow in jet events and the resulting hadronization is further discussed in terms of several different models in order to gain additional insight into particle production in jet events.

This chapter also discusses the relationship between color flow and rapidity gaps in proton-antiproton collisions. Elastic and diffractive scattering, which are typically associated with rapidity gaps, are discussed to introduce the ideas of rapidity gap production and the Pomeron. Rapidity gap "production" in hard scattering jet events is then motivated in terms of color flow and hadronization. Finally, the various processes contributing to rapidity gap production are covered along with both qualitative and quantitative predictions for the rapidity gap fraction.

2.1 The Quark-Parton Model

The electron, unlike the proton, is believed to be a point-like particle with no substructure. Predictions from quantum electrodynamics for e^+e^-, e^-e^- and e^+e^+ interactions have been confirmed experimentally and indicate that the electron and the positron have a point-like structure.

In contrast, the proton has a complex substructure. This was first observed in deep inelastic electron-proton scattering ($ep \rightarrow e+X$) experiments and is evidenced routinely in proton-antiproton experiments ($p\bar{p} \rightarrow X$). A successful model for describing the structure of the proton (and antiproton) is the quark-parton model.

The main assumption of the quark-parton model is that a hadron can be represented by constituent point-like particles (partons) if the hadron collides with

some other particle with a large momentum transfer (Q). The partons, or parts of the hadron, are quarks and gluons. The masses of the hadron and its partons are neglected since they are small compared to the energy scale Q of the hard scattering.

Each parton necessarily has some fraction x of the total momentum of its parent hadron. Thus, for a hadron with momentum p^μ, parton i has momentum $x_i p^\mu$, where $\sum_{partons} x_j = 1$ (i.e. the sum of all parton momentum fractions is one). However, each type of parton—or flavor—does not necessarily have the same probability of having momentum fraction x of the parent hadron: the *parton distribution function* $f_{A\to i}(x, Q)$ represents the probability density of a parton i having momentum fraction x of the parent hadron A. These distributions currently cannot be calculated from theory and are empirically obtained from data (e.g. deep inelastic scattering experiments). Figure 2-1 shows parton distribution functions measured for the proton at low Q [9]. By folding the measured parton distribution functions with calculations for partonic cross sections from perturbation theory, various cross sections can be calculated. This method is called *factorization* since the calculation is factored into independently measurable or calculable parts that are subsequently combined into verifiable predictions [10].

The cross section for a specific process is calculated by summing over all relevant parton-parton scatterings, weighted by the appropriate distribution functions. The cross section for two jet (i.e. two parton) production in $p\bar{p}$ collisions can therefore be written as

$$\begin{aligned}\frac{d\sigma}{dx_1 dx_2}(p\bar{p} \to c(x_1)d(x_2) + X) &= \sum_{abcd} \int dx_a dx_b \; (f_{p\to a}(x_a) f_{\bar{p}\to b}(x_b) \\ &\quad \times \hat{\sigma}(a(x_a)b(x_b) \to c(x_1)d(x_2)) + \text{perm.})\end{aligned}$$

where $\hat{\sigma}(ab \to cd)$ is the lowest order subprocess scattering cross section for two partons.

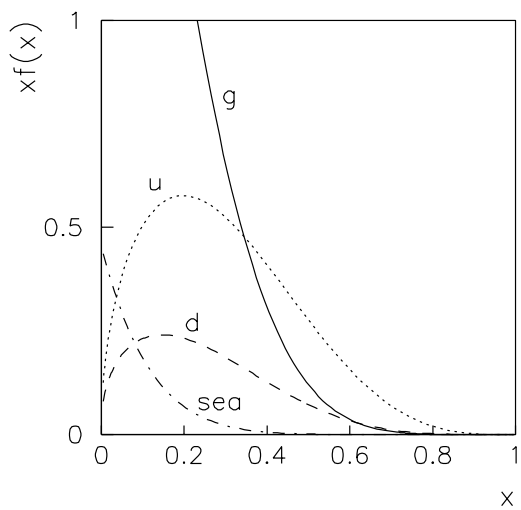

Figure 2-1: Parton distribution functions for the proton at low Q. The proton consists of gluons (g), "valence" quarks (u and d), and "sea" quark-antiquark pairs. (Figure adopted from Ref. [9].)

To calculate the inclusive cross section for producing a specific final-state hadron, namely $p\bar{p} \to H + X$, an additional distribution, called the *fragmentation function* $D_{i\to H}(z)$, must be introduced. This is the probability for a parton i with momentum q^μ/z to produce hadron H with momentum q^μ in the final state. The cross section is given by

$$\begin{aligned}\frac{d\sigma}{dq}(p\bar{p} \to H(q) + X) &= \sum_{abcd} \int dx_a dx_b dz \; (f_{p\to a}(x_a) f_{\bar{p}\to b}(x_b) D_{c\to H}(z) \\ &\quad \times \hat{\sigma}(a(x_a)b(x_b) \to c(q/z)d) + \text{perm.})\end{aligned}$$

where $\hat{\sigma}(ab \to cd)$ is the partonic subprocess scattering cross section. In contrast to parton distribution functions, which give the probability of finding a certain parton in a hadron, fragmentation functions give the probability of producing a certain hadron from a parton. Therefore, the quark-parton model can be expanded to calculate the cross section for any final state, assuming that the appropriate parton distributions and fragmentation functions are known, and all the appropriate parton-parton subprocess cross sections can be calculated.

In summary, the quark-parton model approximates high transverse momentum scattering processes in hadron-hadron collisions by "factorizing" the process distinctly into the initial state (parton distribution functions), the intermediate state (the hard parton-parton scattering cross sections) and the final state production of hadrons (fragmentation functions). Factorization allows the non-calculable effects of quark and gluon confinement to be reduced to empirical probabilities, which can be determined from experiment, while the parton-parton interactions are calculated from perturbation theory (QCD).

Factorization is also useful for determining other interactions that may accompany a hard interaction such as additional hard parton-parton scatterings or soft (low transverse momentum) spectator interactions. In general, however, calculation of these processes is model dependent and less rigorous than perturbative methods.

2.2 Perturbative QCD

Quantum chromodynamics (QCD) describes the physics of strong interactions. Each parton (i.e. quark or gluon) carries a "color charge" which determines how it interacts with other partons. Empirically, a quark can have one of three color charges: red(R), green(G) or blue(B), while an antiquark can have one of three anticolor charges: $\bar{R}$, $\bar{G}$ or $\bar{B}$. At the lowest-order approximation, the interactions between quarks are mediated by a color-charged quantum field, called the gluon, which changes the color charge of the interacting quarks. A gluon can have one of eight combinations of color-anticolor charge, such as $R\bar{B}$ or $G\bar{R}$. The color symmetric "gluon", $R\bar{R}+G\bar{G}+B\bar{B}$, is a "color singlet" (no net color charge) and does not interact. A Feynman diagram of quark scattering via the exchange of a gluon is shown in Fig. 2-2. The color charge is conserved in the same way that electric charge must be conserved.

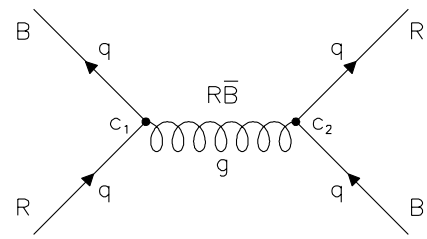

Figure 2-2: Feynman diagram of quark (q) scattering via exchange of a gluon (g). Each vertex is assigned a color factor c depending on the color flow through the vertex. At every point color charge is conserved.

In quantum electrodynamics (QED), the strength of a fermion-fermion force is proportional to the electric charge of the fermions and the fine structure constant: $(e_1 e_2)\alpha$. Similarly, in QCD the strength of the strong interaction force is determined by the color factors c (magnitude of charge) of the interacting partons and the *strong coupling constant* α_s: $(c_1 c_2)\alpha_s/2$. By exploiting the color symmetry of QCD and the properties of fermions (all quarks are fermions), the interactions between quarks and gluons can be represented by Feynman diagrams with the appropriate couplings at each vertex. Once all possible Feynman diagrams for a specific process have been determined, the calculation of an observable (such as a cross section) reduces to matrix algebra. This is the essence of perturbative QCD.

2.2.1 The Running Coupling Constant

Perturbative QCD is applicable only in "high" energy (momentum transfer) regimes (short distances and times): it cannot explain the structure of hadrons or the fragmentation of partons into hadrons, which involve much smaller energies, longer times and larger distances. This is due to properties of quarks and gluons called *confinement* and *asymptotic freedom.* Confinement is the statement that as one parton (colored object) separates from another, the force between them rises with-

out bounds within a very short distance—partons cannot be observed as free objects. Asymptotic freedom is the statement that as two partons get closer, the force between them gets smaller and approaches zero—the partons act as if they are free objects. This effect is shown in Fig. 2-3 as a function of the energy scale Q of the interaction between partons. As $Q \to \infty$ (probing small distances) the QCD coupling constant α_s approaches zero—that is, asymptotic freedom. As $Q \to 0$, however, the coupling constant becomes very large, resulting in confinement of quarks and gluons within hadrons.

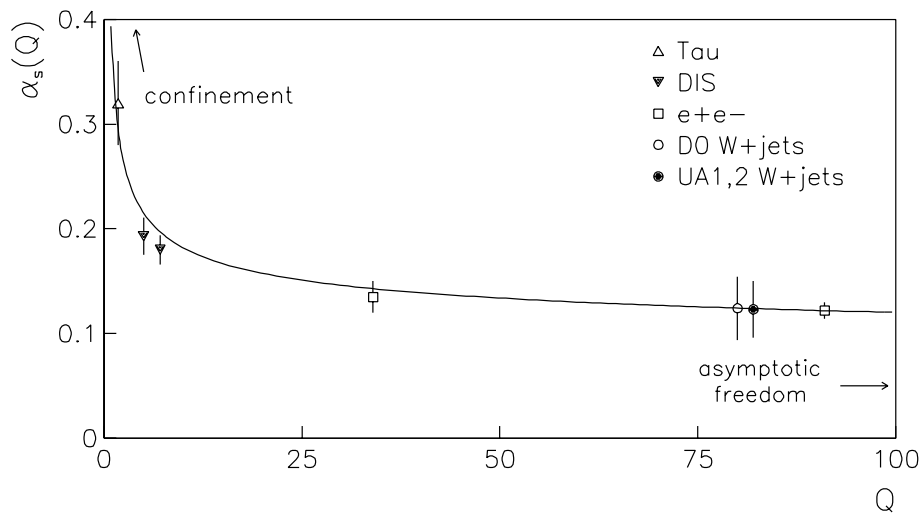

Figure 2-3: Behavior of the strong coupling constant α_s as a function of the energy scale Q. The solid line illustrates the leading-order behavior of α_s as given by Eq. 2.1. At small Q (large distances) the coupling is large (resulting in confinement), but steadily decreases for high Q (leading to asymptotic freedom). Some measurements of α_s are also shown.

The strong coupling constant can be calculated within perturbative QCD. This involves a detailed procedure, called renormalization, which takes into account the infinities and divergences that occur when calculating Feynman diagrams. The net result of this procedure is the introduction of a mass scale parameter Λ_{QCD} which makes the calculations well-behaved. The leading-order expression for the strong

coupling constant is

$$\alpha_s(Q^2) = \frac{12\pi}{(33 - 2n_f)\log(Q^2/\Lambda_{QCD}^2)} \tag{2.1}$$

where n_f is the number of quark flavors excited at a given Q, and Λ_{QCD} is a fundamental scale parameter of QCD which is determined experimentally. This parameter, measured to be approximately 200 MeV, is roughly the energy scale that determines where perturbative calculations fail (diverge) and phenomenological models must be used to determine the non-perturbative particle production (hadronization).

2.3 Jet and Particle Production

The production of jets in hadron-hadron collisions can be represented by (or "factorized") into five distinct processes: the initial-state parton configuration (non-perturbative parton distribution functions), initial-state parton radiation (parton showering, calculated perturbatively down to energies approaching Λ_{QCD}), the hard parton-parton interaction (calculated perturbatively to a fixed order), final-state parton radiation (also parton showering), and hadronization or fragmentation (non-perturbative and empirically derived). This factorization scheme allows separate calculations to be performed only in the regimes where they are applicable and accurate. These calculations can then be combined to yield the final result (e.g. a simulated event) which could not be obtained without factorization.

2.3.1 Hard Scattering

At its simplest, jet production in hadron-hadron collisions is hard scattering of partons. These lowest order subprocesses are (charge-conjugate processes implied): $qq \to qq$, $q\bar{q} \to q\bar{q}$, $q\bar{q} \to gg$, $gg \to q\bar{q}$, $qg \to qg$ and $gg \to gg$. Some leading-

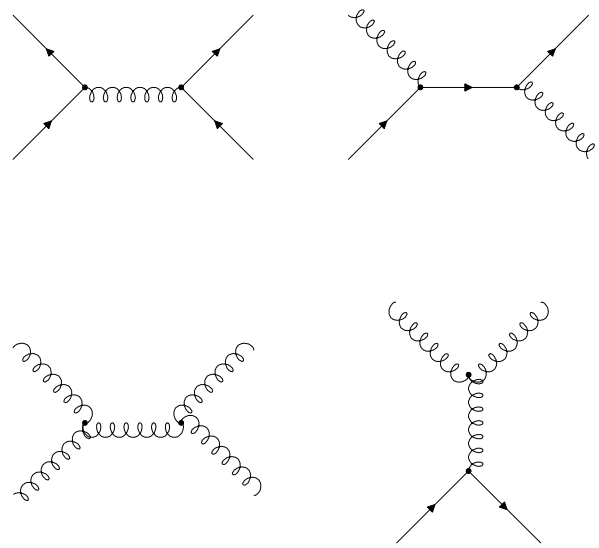

Figure 2-4: Examples of leading-order (α_s^2) Feynman diagrams for jet production.

order ($O(\alpha_s^2)$) Feynman diagrams are shown in Fig. 2-4. Leading-order calculations derived from these Feynman diagrams describe two-jet production reasonably well, within certain kinematic regimes.

To explain three jet production and higher-order effects on two-jet production, next-to-leading-order diagrams ($O(\alpha_s^3)$) must be included in the calculation (see Fig. 2-5). At this order, many more subprocesses must be included, a few of which are $qq \to qqg$, $qg \to qgg$, $q\bar{q} \to ggg$ and $gg \to gq\bar{q}$. While the accuracy of the much more involved next-to-leading-order calculations is improved compared to leading-order, there is an added complication related to the jet definition (see §2.5.2).

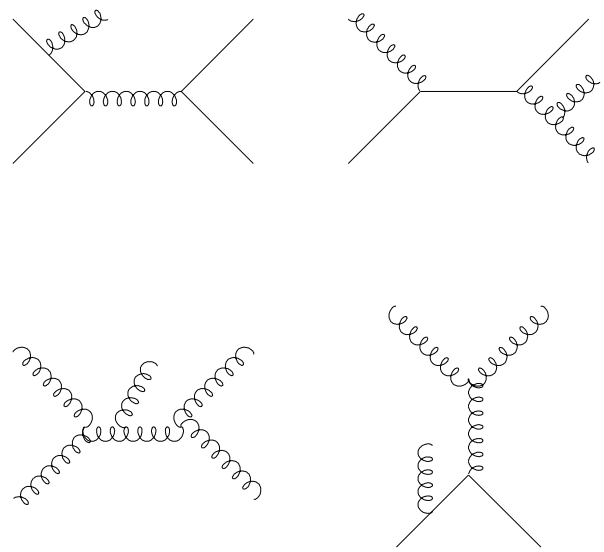

Figure 2-5: Examples of next-to-leading-order (α_s^3) Feynman diagrams for jet production.

2.3.2 Parton Showering and Evolution

In order to fully explain experimentally observed multijet production, higher-order Feynman diagrams (next-to-next-to-leading-order etc.) must be calculated. However, at present only next-to-leading order processes have been fully calculated [11] and calculating higher orders rapidly becomes technically difficult.

A very useful approximation, the so-called leading-log approximation (LLA), takes into account higher order processes and allows more accurate calculation of multijet production and hadronization. These equations represent *all-order* processes to the "one-loop" level. That is, all order Feynman diagrams are partially taken into account by utilizing the leading order expression for α_s as given in Eq. 2.1. Higher order corrections to α_s are neglected in order to calculate perturbatively to all orders.

The leading-log approximation describes the "equation of state" for a quark

or gluon at a certain energy scale Q, where Q gives the characteristic time or distance scale of the interaction. In this approximation any quark (at a given Q) could have previously "radiated" a gluon or could be the result of a gluon splitting into a quark-antiquark pair. Similarly, any gluon could have originated (been radiated) from a quark or could have radiated a gluon itself. Thus quarks and gluons are coupled in a way that determines their evolution as a function of Q.

The leading-log approximation has become extremely useful in the simulation of jet and particle production. Since the leading-log approximation determines the relative probabilities of quark and gluon "branchings" or radiation, it can be adapted for use in simulations of jet production. In these simulations both the initial and final hard partons can radiate other partons according to the leading-log approximation. Since each of the resulting partons can also radiate (or decay into) other partons, a cascade of partons or a *parton shower* is formed as illustrated in Fig. 2-6. At small times (corresponding to small distances), the partons have a large invariant (virtual) mass, producing radiation at large angles and/or large momentum. As time progresses, the invariant masses of the radiated partons decreases until the invariant mass or momentum of the partons in the shower begins to approach the QCD scale parameter Λ_{QCD} where perturbative calculations diverge. At some low cutoff energy (still much greater than Λ_{QCD}), each parton is not allowed to decay (or radiate) further and hadronization is simulated using phenomenological hadronization models (see §2.3.4).

2.3.3 Color Coherence

While the simple parton showering picture is useful for simulating jet and particle production, it ignores significant interference effects between partons. This interference, or *color coherence*, effectively results in an "angular ordering" of the

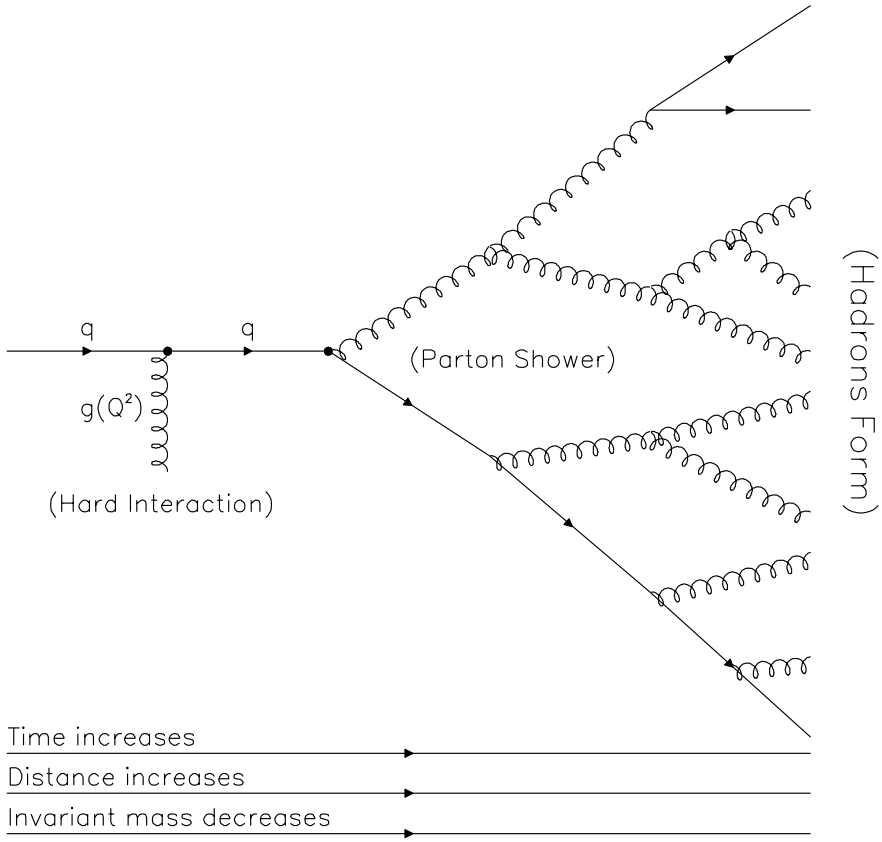

Figure 2-6: Schematic evolution of a parton shower. At small times and small distances the invariant masses of the partons are comparable to the hard interaction energy scale. As time increases, the energy scale Q of the radiated partons approaches Λ_{QCD} (QCD scale parameter) and non-perturbative "hadronization" (confinement) occurs. (Figure adopted from Ref. [12].)

sequential parton decays (or radiation) in which the angle of parton emission depends on the previous shower development.

Angular ordering of parton cascades can be explained by a simple quantum mechanical argument [13]. For simplicity we will deal with the decay of a virtual gluon into a relativistic massless quark-antiquark pair and a gluon ($g \rightarrow q\bar{q}g$). (This argument can easily be extended to other parton emissions or radiations.)

First we assume that the final gluon was actually radiated from either the quark (or antiquark) at some time $t_g > 0$ after the initial $g \rightarrow q\bar{q}$ decay. The gluon's momentum is constrained by the lifetime t_g of the parton that radiated it due to the uncertainty principle: for small t_g, the gluon momentum is large while for large t_g the momentum is small. However, there is an additional constraint on the radiated gluon: the radiated gluon must have a transverse wavelength ($\sim$1/energy) smaller than the maximum transverse separation of the quark-antiquark pair. If the transverse wavelength were larger than the separation of the quark-antiquark pair, the gluon would not be able to "resolve" the pair and separate the quark from the antiquark. Thus a radiated gluon that has a transverse wavelength that is too large to resolve the quark-antiquark pair can be thought of as effectively originating from the original gluon since it can't "see" the individual quark and antiquark. The quark-antiquark pair therefore *coherently* radiates as if it was only one parton, i.e. the original gluon.

This quantum mechanical argument results in a simple requirement on successive parton emissions: the angle between two partons resulting from the decay of another parton must be smaller than the angle of decay that produced the preceeding parton [13], as illustrated in Fig. 2-7. Thus higher order QCD interference effects can be largely taken into account by imposing an *angular ordering* on the parton shower.

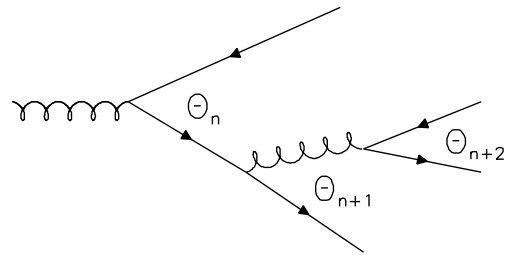

Figure 2-7: Illustration of the angular ordering of parton radiation. Each successive partonic "branching" angle θ must be less than the previous: $\theta_1 > \cdots\cdots > \theta_n > \theta_{n+1} > \theta_{n+2} \cdots$. (Figure adopted from Ref. [12].)

2.3.4 Hadronization

The hadronization of quarks and gluons into final state particles cannot currently be calculated by perturbative methods and is derived from experiments and/or phenomenological models. Although perturbative QCD and parton showering qualitatively explain large scale effects such as jet production and color coherence effects, the actual distribution of final state particles in hard scattering hadron-hadron events is not well understood. Certain models have been developed to get the overall hadronization pattern correct, but this usually involves "tuning" to data (if data exists).

Several models have been successful in "explaining" the final-state particle production in hard scattering hadron-hadron events. One is the "string model", in which colored objects (quarks and gluons) are connected by a tube or string [14]. As the string stretches (e.g. as a quark-antiquark pair separates), potential energy is built up in the string. Once the energy in the string reaches the threshold of energy required to create a new quark-antiquark pair, the string can break into two sections. The process continues until each quark-antiquark pair becomes stable and cannot produce more pairs. The remaining quark-antiquark pairs form the final state hadrons. (The string model is discussed in greater detail in §2.6.1.)

Although various other models have been developed to explain hadronization,

the string model is widely accepted due to its relatively simple intuitive interpretation and simple implementation. It can be applied in conjunction with the hard parton level (e.g. LO or NLO QCD) predictions to reproduce the qualitative hadronization pattern in hard scattering jet events, or it can be used in combination with parton showering (or other models) which account for higher order QCD effects such as color coherence.

2.3.5 Spectator Interactions

While the hard scattering collision (e.g. jet production) is usually of primary concern because it allows one to probe deeply into the structure of matter, interactions between the "spectators" (remaining partons) of the proton and antiproton can also produce particles. These *spectator interactions*, sometimes referred to as the soft underlying event, are expected to produce a roughly uniform distribution of low energy particles in η-ϕ space (see §2.5.1 for the definition of η and ϕ). The distribution is believed to be similar to the distribution of particles in a minimum bias event (see §2.7.4) although there is little, if any, experimental information confirming this.

Spectator interactions may also include secondary semi-hard parton scattering which produces "minijets" with small transverse momenta. Minijet production has the advantage that it can be perturbatively calculated and included in cross section calculations. Minijets have been observed in minimum bias events [15] indicating that semi-hard scattering is necessary for a more complete understanding of proton-antiproton collisions.

2.4 The Monte Carlo Event Generator

If one were only interested in jet production cross sections in certain limited kinematic regions, analytical QCD hard scattering predictions (§2.3.1) would be sufficient to test the present state of the theory. Once one has agreed on a jet definition (§2.5.2), comparison of theoretical and experimental cross sections would not in principle depend on the details of parton showering or hadronization, since ideally there would be a one-to-one correspondence of hard final-state partons and experimentally observable jets.

However, in order to explain higher order effects on jet production (such as multijet production and color coherence), one needs a more complete description of hard scattering hadron-hadron collisions. For this reason, various stochastic "Monte Carlo" event generators have been developed to simulate the complicated interactions involved in proton-antiproton collisions. In these event generators (computer programs), the interactions are factorized into many manageable calculations (such as discussed in the sections above) in an effort to obtain the most accurate predictions.

Since many aspects of QCD and particle production are still not well understood, most Monte Carlo generators allow users to vary certain parameters or input distributions (such as parton distribution functions). Usually the default settings incorporate a nominal set of parameters that have been tuned to agree with certain well-established experimental distributions at certain center-of-mass energies. The generators can then be used to predict distributions or cross sections at other energies with a certain accuracy depending on the particular models and parameters that are used in the simulations.

Monte Carlo event generators are also very useful in testing experimental particle detector designs. By modeling a detector design and its properties, Monte Carlo event generators can be used to assess (in a limited way) the detector's

behavior and ability to measure the desired distributions or cross sections. The results of these simulations can be used to aid in development of new detectors or to understand existing ones in terms of their efficiency, discrimination, and response with respect to analyses of interest.

2.5 Theoretical and Experimental Conventions

2.5.1 Invariant Phase Space and Transverse Momentum

In hadron-hadron collisions, there are essentially three relevant variables that are used to describe partons, particles, or jets. These are *azimuthal angle* ϕ, *rapidity* y (or *pseudorapidity* η), and *transverse momentum* p_T. These variable form a convenient *invariant phase space*,

$$\frac{d^3p}{E} = p_T\, dp_T\, dy\, d\phi,$$

which satisfies simple transformation properties under longitudinal Lorentz boosts:

$$\begin{aligned} p_T &\rightarrow p_T \\ \phi &\rightarrow \phi \\ y &\rightarrow y + \text{const.} \end{aligned}$$

Therefore distributions in these variables are invariant under longitudinal Lorentz boosts.

These variables are described in greater detail below:

- The *azimuthal angle* ϕ is the angle in the plane perpendicular (xy-plane) to the initial proton-antiproton beam directions (z-axis).

- *Rapidity* is a measure of an object's fractional momentum along the z-axis and is given by $y = \tanh^{-1}(p_z/E)$, where p_z and E are the longitudinal

momentum and total energy, respectively, of the object. Rapidity has the advantage that the shape of a distribution as a function of rapidity is invariant under Lorentz boosts—e.g. a cross section, $d\sigma/dy$. Thus, the longitudinal boost of the center-of-mass system does not affect the shape of distributions in rapidity.

- *Pseudorapidity* (η) is an approximation to rapidity when the mass of the particle is much smaller than its energy (i.e. relativistic) and its angle from the z-axis is not too small. Pseudorapidity has the same invariance property as rapidity, provided that the particle masses can be neglected. Unlike rapidity however, pseudorapidity can be calculated even if the mass is unknown—which frequently occurs experimentally. In addition, it is directly related to the zenith angle θ from the z-axis by $\eta = -\ln\tan(\theta/2)$. Thus the pseudorapidity can be considered both a spatial coordinate and a kinematic variable.

- *Transverse momentum* denotes the momentum perpendicular to the collision axis (z-axis): $p_T = \sqrt{p_x^2 + p_y^2}$. Its value is also invariant under longitudinal Lorentz boosts and is the same if measured in the center-of-mass system or in the lab frame. A frequently used experimental variant of transverse momentum is *transverse energy* (E_T) in which the object (particle or jet) is assumed to be massless.

2.5.2 Jet Definition

Experimentally, jets are observed as a collimated spray of hadrons originating from the interaction point. That is, jets are the products (remnants) of the partons that undergo the hard interaction. Since theorists generally define jets as the unobservable final-state hard partons themselves (or sprays of partons), some convention must be made for an experimental jet definition in order to compare to hard parton

level predictions.

The jet definition typically used at hadron-hadron colliders is based on a "cone" or circle in η-ϕ space [16]. Any particle that falls within the cone is considered part of the jet, and any particles falling outside the cone are ignored. The actual radius of the cone is somewhat arbitrary but a typically used cone size is $R = \sqrt{(\Delta\eta)^2 + (\Delta\phi)^2} = 0.7$, which is large enough to contain most of the jet energy.

The cone definition would be relatively simple to apply if real jet production were at most a leading-order process—i.e. only two jets produced in any interaction. In this case one would use the same jet definition in the theory and experiment and compare cross sections unambiguously, since each jet would correspond to one and only one parton. However, if higher orders are included in the theory, multijet (more than two jets) production is allowed, and the jets are not necessarily widely separated in η-ϕ space. Thus two jet cones can overlap significantly, and the jet definition becomes more complicated both theoretically and experimentally.

The major difficulty lies in finding a method that minimizes differences between experimental "jet finding" and the theoretical parton level predictions, especially when jets are close to each other in η-ϕ space. Since experiments see only the products of partons, there is no unique way of defining a jet that perfectly corresponds to the parton level. However, several methods have been used with reasonable success to account for jets that overlap.

One common method uses a definition based on energy in the overlap region. If the shared energy in the overlap region is greater than some fraction, the two original jets are "merged" into one, otherwise the energy is split between the original jets in some reasonable way. Other methods employ a simple geometric condition to determine how to define overlapping jet cones.

One method which completely avoids the problems associated with cones is based on the "clustering" of particles. In this method a resolution parameter is

used to determine if particles are to be included in a jet. As a result, particles belong to a specific jet with no overlapping of jets. This method has mostly been used in e^+e^- experiments, but due to its simplicity compared to cone definitions, it is beginning to be used in $p\bar{p}$ experiments [17].

2.6 Color and Particle Flow in Jet Events

As discussed in previous sections, QCD describes the dynamics of interactions between color-charged partons. The exchange of color between partons, or the *color flow*, determines the dynamics of hard interactions. However, although color itself is confined (quarks and gluons are confined), the color flow in hadron-hadron interactions is observable via the resulting *particle flow* or hadronization into final-state particles.

A simple quantum mechanical argument can be used to understand why color flow is observable as a particle flow. The color flow (exchange of color) in hard parton scattering is determined in a very short time scale on the order of $1/Q$, where Q is on the order of the invariant mass of the interacting partons. However, the time scale for hadronization into colorless observable particles is on the order of $1/\Lambda_{QCD} \gg 1/Q$. Therefore, the system (the separating color-connected system of partons) has a long enough time (from kinematics and the uncertainty principle) to radiate a significant number of partons that subsequently hadronize into observable particles. If the time scale for hadronization were on the order of the hard scattering time scale, only the remnants of the hard partons would be observable as a few highly energetic particles in each parton direction (a very narrow jet), and the color flow would not be observable by its hadronization into many particles. Thus both the dynamics of jet production and the resulting hadronization into final-state particles are closely tied to the color flow in the interaction.

As mentioned in §2.2, quarks and gluons form specific *color multiplets* depend-

ing on the the color symmetry properties of each: quarks form a *color triplet* (since each can have one of three colors) and gluons form a *color octet* (since gluons can have one of eight color-anticolor charges). Color triplets (quarks) and octets (gluons) interact in such a way that the overall color state and internal color flow is conserved. A neutral *color singlet* is formed when the system (or part of the system) is in a color symmetric state in which each color charge exists in equal quantities. All observable final state particles are color singlets due to the confinement of color.

The relationship between color flow and particle flow (hadronization) in hard scattering interactions can be illustrated with several different models, each of which qualitatively gives the same results. The string model, initially successful for predicting the so-called "string effect" in $e^+e^- \rightarrow 3\,\text{jets}$, is very useful because of its simple intuitive interpretation. The color dipole model, which has its basis in classical electrodynamics, also provides a relatively simple but extremely useful picture which takes into account color coherence effects. Finally, the parton shower model (discussed earlier), with its direct basis in perturbative QCD, gives the same results as the simpler models. These models qualitatively give the same prediction: color flow between partons leads to particle flow between the partons—the so-called *rapidity plateau.* Conversely, the lack of color flow between partons leads to an absence of particle production between the parton, or a *rapidity gap.*

2.6.1 The String Model

In the string model [14], color-charged partons are connected by a (color-neutral) string which links the partons into a color-singlet configuration. Quarks and antiquarks (and color-triplet combinations of two quarks or two antiquarks called di-quarks) form the ends of the string while gluons form "kinks" in the string, due to their color-anticolor octet charge.

The simplest example of color flow in jet events is the process $e^+e^- \rightarrow q\bar{q}$. Since the overall color of the system is neutral, the final-state $q\bar{q}$ pair forms a color singlet. However, the quark and antiquark are both color charged and a string representing the color field (lines) can be drawn between the final-state quarks. As the quark and antiquark separate relativistically, the string builds up potential energy which is released inelastically by breaks in the string—manifested as new $q\bar{q}$ pairs. The resulting strings continue to break until all of the potential energy has been converted to $q\bar{q}$ pairs. The remaining $q\bar{q}$ pairs still connected by strings form the color-singlet final-state hadrons, which tend to fill η-ϕ space uniformly. Thus the color flow—the color-connected quark and antiquark—is observable as a flow of particles filling the available space.

In the slightly more complicated process, $e^+e^- \rightarrow q\bar{q}g$ (3 jet production), the overall color of the $q\bar{q}g$ system is still neutral but the gluon, due to its color-octet charge, becomes a "kink" in the string between the $q\bar{q}$ pair as shown in Fig. 2-8. The string is not collinear with the q, $\bar{q}$ or g momenta, and the string segments are boosted sideways. Thus particle production occurs asymmetrically, and the angular region between the $q\bar{q}$ pair is depleted. In contrast, for kinematically similar $e^+e^- \rightarrow q\bar{q}\gamma$ interactions, the region between the $q\bar{q}$ pair is enhanced since the photon has no color charge which "drags" the string away from that region. This is the predicted "string effect" which was subsequently observed in e^+e^- experiments [18].

In proton-antiproton collisions, the string topology becomes more complicated due to the partonic structure of the proton and antiproton. Since any parton of the proton can interact with any parton of the antiproton, there are many possible "subprocess" hard interactions that can take place (see §2.3.1 for some examples). For each of these possible subprocesses there are many combinations of color exchange and color flow allowed by QCD. Some examples of string topologies

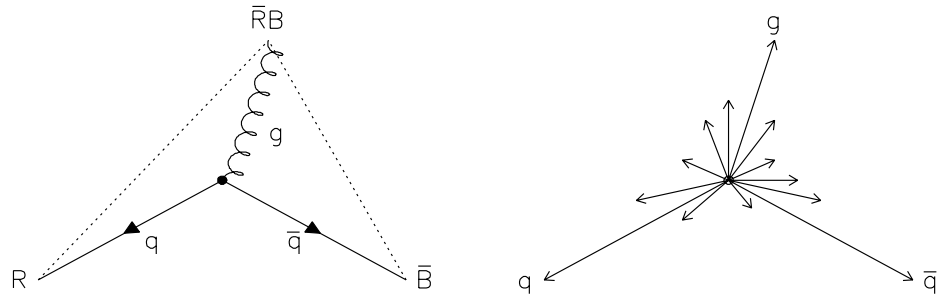

Figure 2-8: The "string effect" in $e^+e^- \to q\bar{q}g$. The outgoing quarks form the ends of the string (dotted line) while the gluon forms a "kink". The resulting hadronization (right) produces particles between the quarks and gluon while the region between the quark and antiquark is depleted.

are given in Fig. 2-9.

Although the string model provides a useful way of accounting for the color flow and the general qualitative hadronization pattern in jet events, it must be tuned to agree with data (usually in combination with the highest order QCD calculations available and/or parton showering). Nevertheless, the string model's success in predicting the color coherence string effect observed in $e^+e^- \to q\bar{q}g$ indicates that it has some underlying dynamical features. However, the string model is not sufficient to explain multijet production, higher order coherence effects, or the exact details of particle flow in hadron-hadron collisions.

2.6.2 The Color Dipole Model

Another relatively simple picture useful for understanding color flow and the resulting hadronization is the color dipole model. This model has its origin in classical electrodynamics: a relativistically separating e^+e^- pair has a radiation pattern characteristic of a dipole or antenna. In its center-of-mass (cms) system the dipole radiation (photon emission) is given by

$$\frac{d\sigma}{dy\, d\phi\, dp_T^2} \approx \frac{\alpha}{4\pi^2}\frac{1}{p_T^2}. \tag{2.2}$$

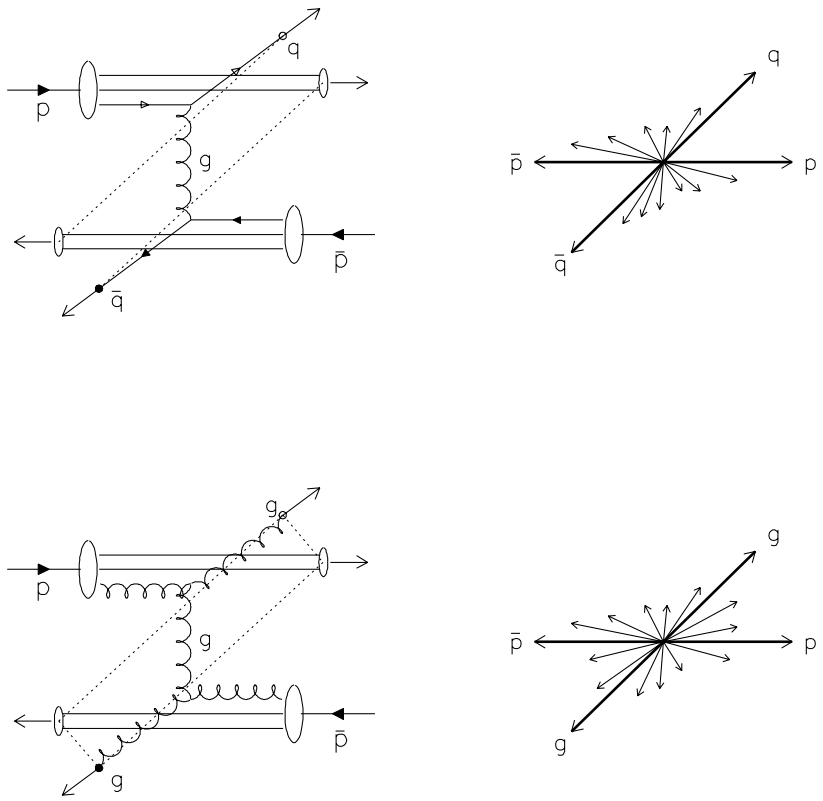

Figure 2-9: Examples of color flow in hard $p\bar{p}$ collisions. Two subprocesses, $q\bar{q} \to q\bar{q}$ and $gg \to gg$ are represented schematically (left). The initial proton and antiproton interact via the exchange of a hard gluon. The outgoing partons (full circles) are connected to the outgoing spectator quarks or beam hadron remnants (small ovals) by strings (dotted lines). The resulting hadronization in the hard scattering center-of-mass is shown schematically (right) for each subprocess.

For a fixed p_T this corresponds to a flat distribution in rapidity (y) and azimuthal angle (ϕ) between the kinematical limits $|y| \approx ln(W/p_T)$, where W is the invariant mass of the e^+e^- pair. This distribution is called a *rapidity plateau.*

This picture can easily be extended to QCD [19] if the e^+e^- pair is replaced by a $q\bar{q}$ pair and α is replaced by $\alpha_s N_c$, where N_c is the number of colors (three). In this case, however, when a color-charged gluon is radiated, it alters the dipole by splitting the original dipole into two: one connecting the quark and the gluon and one connecting the gluon and the antiquark. Successive gluon radiations create additional smaller dipoles, each of which radiates independently. Since each dipole has an implicit kinematic limit depending on its invariant mass, color coherence effects are automatically taken into account. The color dipole model has been implemented in a Monte Carlo program ARIADNE [20] and has been shown to give results similar to those from parton shower models [19].

The string model and color dipole model give qualitatively the same results since each assumes that a color connected quark-antiquark pair forms a field (a string or dipole respectively) which radiates (particles or gluons respectively). Thus color flow between color-connected partons is manifested by hadronization into observable particles. Although the color dipole model provides a more dynamical picture than the string model since it explicitly takes into account color coherence (like parton showers with angular ordering), the string model is still useful for understanding the large scale qualitative effects of hadronization.

2.6.3 Strings and the Rapidity Plateau

As mentioned above, due to color coherence effects and the long time for hadronization, the color flow in an event leads to specific observable hadronization patterns. The string model provides the simplest picture for understanding color flow and hadronization: wherever a string can be drawn between partons (in an overall color

singlet), particle production is expected to occur.

In the process $e^+e^- \rightarrow q\bar{q}$, a string representing the color flow can be drawn between the quark and antiquark. The hadronization of this string (in its center-of-mass system) is approximately uniform in rapidity and azimuthal angle, leading to the experimentally observed rapidity plateau. This plateau is a natural feature of dipole and parton showering models. The rapidity plateau spans from the quark to the antiquark and populates the region between them uniformly in y-ϕ space (for a fixed p_T) as given by Eq. 2.2. Higher order corrections from gluon radiation modify the distribution, but the qualitative behavior is unchanged: hadronization occurs roughly uniformly in y-ϕ space in the center-of-mass system of a string or two-jet system.

The string effect (color coherence) in $e^+e^- \rightarrow q\bar{q}g$ events can be understood simply in terms of boosted strings or boosted plateaus. Since the string connecting the q, $\bar{q}$ and g is not in its center-of-mass system, each segment of the string (which independently gives a rapidity plateau) is boosted transversely (see Fig. 2-8). This boost causes a suppression of radiation in the azimuthal direction opposite the boost due to the Lorentz contraction of the radiation pattern. The result (in the lab frame) is the depletion of hadrons in the region between the quark and antiquark and enhancement between both the quark and gluon and the antiquark and gluon. In contrast, for $e^+e^- \rightarrow q\bar{q}\gamma$ interactions, the string between the quark and antiquark is boosted away from the photon, enhancing particle production in that region.

This kinematical string picture is very useful for explaining particle production patterns in both low and high transverse momentum proton-antiproton collisions. For example, the rapidity plateau in minimum bias events arises from the color flow between soft partons in the proton and antiproton, while rapidity gaps in elastic and diffractive scattering can be explained by *lack* of color flow in these events.

Similarly, rapidity gap "production" in jet events can arise from the lack of color flow between the interacting partons. These issues will be discussed further below.

2.7 Elastic and Diffractive Scattering: Rapidity Gaps

In proton-antiproton collisions, most interactions have a small transverse momentum transfer, for which perturbative QCD is not applicable. These interactions include elastic scattering ($p+\bar{p} \rightarrow p+\bar{p}$), single diffractive scattering ($p+\bar{p} \rightarrow p+X$), double diffractive scattering ($p+\bar{p} \rightarrow X+Y$), and nondiffractive inelastic scattering ($p+\bar{p} \rightarrow X$). In elastic scattering both initial protons remain intact and are scattered at small angles due to the small momentum transfer. In diffractive scattering, however, one or both of the protons is excited to a higher invariant mass and then decays into hadrons as shown in Fig. 2-10. In nondiffractive inelastic scattering the proton and antiproton exchange color resulting in "soft" (non-perturbative) hadronization which produces a rapidity plateau.

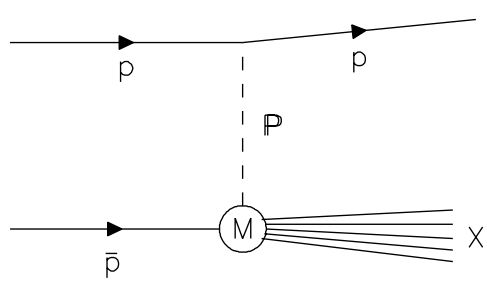

Figure 2-10: Single diffraction via Pomeron exchange. The Pomeron (dotted line) emitted from a proton excites the antiproton into a system with mass M which subsequently decays into hadrons X.

2.7.1 The Pomeron and Rapidity Gaps

The phenomenology of elastic and diffractive scattering is well described by Regge theory [21]. This theory proposes a phenomenological "trajectory", called the *Pomeron* which mediates elastic and diffractive scattering. By definition, the Pomeron has the quantum numbers of the vacuum since it does not change the quantum numbers of the proton or antiproton. The Pomeron is therefore a color singlet.

Since the Pomeron is a color singlet, there is no color flow (exchange) between the proton and antiproton and each remains in a color-singlet state. However, the Pomeron can excite the proton (and/or antiproton) to a higher invariant mass which can decay into additional hadrons, depending on the excited mass. Since these particles are boosted with the original proton (or antiproton) momentum, they are produced primarily at high rapidity along the initial proton (or antiproton) direction. As a result, the region of rapidity ($|y| \ll y_{proton}$) at large angles away from the proton and antiproton directions is rarely populated with particles. For typical events a significant region of y-ϕ (η-ϕ) space is unoccupied by final-state particles: this region is called a *rapidity gap*.

In elastic scattering—which by definition has a rapidity gap—the rapidity gap edges are defined by the rapidities of the proton and antiproton. In diffractive scattering, the rapidity gap is given by the largest region of phase space not occupied by final-state hadrons, i.e. the region not occupied by the fragmentation (decay products) of the excited proton (and/or antiproton). Thus the exchange of a Pomeron, a color singlet, produces rapidity gaps in elastic and soft diffractive scattering.

2.7.2 The Hard Pomeron and Jet Production

Typically the Pomeron has been used to explain low transverse momentum cross sections for elastic and diffractive scattering. However, if the Pomeron has partonic substructure, jets should be produced in some diffractive events [22]. Jet production has recently been observed experimentally in diffractive events [6], indicating that the Pomeron does have partonic substructure. The Pomeron was shown to have a relatively hard component consistent with $q\bar{q}$ or gg partonic constituents, which leads to diffractive jet production.

2.7.3 Nondiffractive Inelastic Scattering

A significant portion of low transverse momentum proton-antiproton collisions do not undergo elastic or diffractive scattering. In these low-p_T nondiffractive inelastic collisions color is exchanged but transverse jets are not typically produced. Thus, these interactions (and similarly hard interactions producing jets) do not typically produce rapidity gaps because there is exchange of color.

The color flow and particle production in these interactions can be explained qualitatively by strings. As the proton and antiproton pass through each other, color is exchanged (e.g. between a quark in the proton and antiquark in the antiproton) via a low-Q^2 gluon as shown in Fig. 2-11. The quark and antiquark thus are color connected by strings to the remnants of the antiproton and proton respectively. Subsequently, each string hadronizes producing a roughly flat distribution of particles in rapidity, or a rapidity plateau, with "beam jets" along the initial proton and antiproton directions. This has been observed experimentally at various center of mass collider energies including Tevatron energies [23, 24]. Thus low-p_T inelastic nondiffractive interactions look very similar to two-jet production in e^+e^-: in the center-of-mass system, each has two back-to-back jets with a rapidity plateau between them.

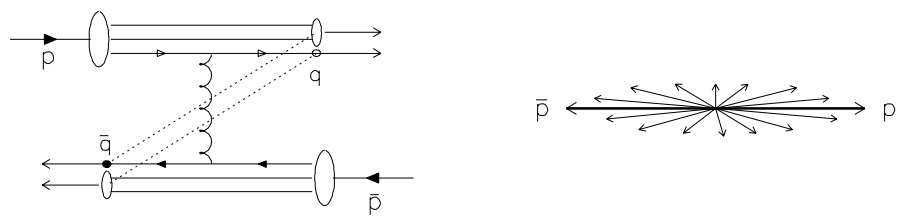

Figure 2-11: The color flow in a nondiffractive inelastic interaction. The exchange of a soft gluon (shown on left) creates two strings (dotted lines) connecting the outgoing proton and antiproton. The resulting hadronization (right) produces a rapidity plateau with beam jets in the initial proton and antiproton directions.

2.7.4 Minimum Bias Events

Experimentally, nondiffractive inelastic scattering is relatively easy to distinguish from elastic or single diffractive scattering due to their drastically different event topologies (in η-ϕ). In contrast, double diffractive and nondiffractive inelastic scattering typically cannot be distinguished on an event-by-event basis. These interactions are collectively called minimum bias events since these events are experimentally obtained using an essentially unselective "inelastic" trigger which rejects only elastic or single diffractive events. Strictly speaking, the experimentally observed rapidity plateau [23, 24] applies to minimum bias events, which include both double diffractive and nondiffractive inelastic events, although the nondiffractive inelastic cross section is dominant.

2.8 Rapidity Gaps in Hard Scattering

In typical hard scattering jet events the color flow tends to fill η-ϕ space with particles. Since typical QCD interactions involve either color-triplet or color-octet exchange, strings stretch across most of phase space as shown in Fig. 2-9. In contrast, if a color singlet is exchanged between the interacting hard partons as shown

in Fig. 2-12, no color flows between the proton and antiproton and the strings are connected only between the hard parton and its associated proton or antiproton remnant. Therefore, for interactions with large pseudorapidity separations between the jets, color-singlet exchange is expected to produce a rapidity gap between the jets.

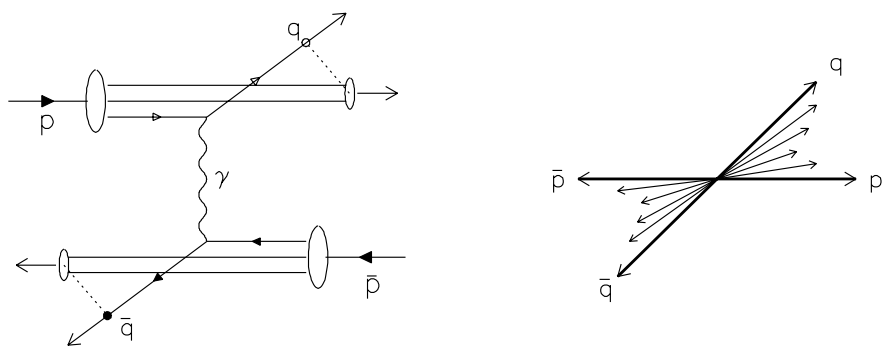

Figure 2-12: The color flow in hard scattering color-singlet exchange. The exchange of a color singlet (in this example, a photon) produces strings (dotted lines) which are connected only between the hard partons and their associated proton or antiproton remnant. The resulting hadronization (right) produces a rapidity gap between the jets since particles are produced only between the outgoing jets and beam remnants.

Figure 2-13 shows the distribution of particles in a two-jet event with a rapidity gap of size $\Delta\eta_c$, where $\Delta\eta_c$ is the pseudorapidity separation between the edges of the jet cones. The exchange of an electroweak gauge boson (γ, $W^{\pm}$, or Z^0), is expected to produce such an event topology. In addition, the exchange of a hard Pomeron, also a color singlet, is expected to produce rapidity gaps between jets. Rapidity gaps can also occur in color-octet or color-triplet exchange events due to fluctuations in the particle multiplicity.

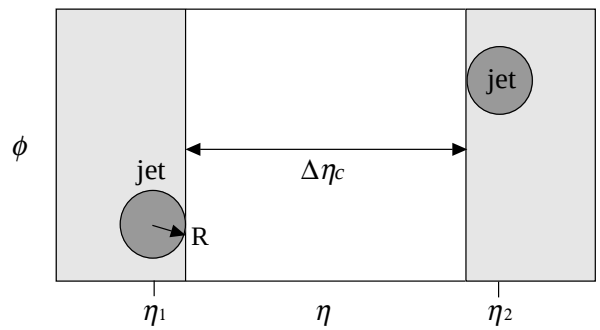

Figure 2-13: Representation in η-ϕ space of the distribution of particles in a typical two-jet event containing a rapidity gap. The pseudorapidity region between the edges of the jet cones (of radius R), $\Delta\eta_c = |\eta_1 - \eta_2| - 2R$, contains no particles.

2.8.1 The Electroweak Color-Singlet Radiation Pattern

While the string model, dipole model, and the angular ordering approximation each predict rapidity gaps from color-singlet exchange between hard partons, Fletcher and Stelzer [4] have shown that the rapidity gap event topology can also be derived directly from perturbation theory. The suppression of radiation in the region between jets can be seen by comparing the parton level cross section for $qq' \to qq'g$ from photon exchange to that for single gluon exchange. For simplicity, the quark jets are fixed at $\eta = \pm 5$ with $p_T = 40\,\text{GeV}$ and the radiated gluon is allowed to vary in pseudorapidity in the plane of the jets. Figure 2-14 shows the radiation pattern of a 1 GeV gluon from photon exchange with respect to single gluon exchange. The relative probability of gluon radiation for photon exchange is plotted as a function of the pseudorapidity of the gluon.

The radiation pattern shows several distinct features. First, at large pseudorapidity the radiation pattern due to the initial- and final-state radiation is similar for photon and gluon exchange. Near the quarks ($|\eta| \gtrsim 5$), however, the radiation from the gluon exchange process is slightly suppressed due to destructive interference of initial and final-state radiation (color coherence effects). In contrast, at small pseudorapidity—i.e. between the jets—the gluon radiation from photon

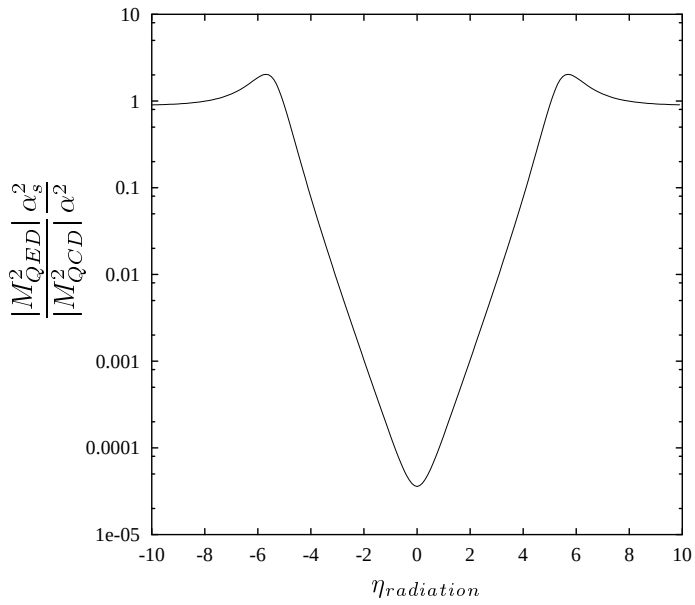

Figure 2-14: Radiation pattern in two-jet events for an additional 1 GeV gluon from photon exchange with respect to single gluon exchange [4]. The quark jets are fixed at $\eta = \pm 5$. The relative probability for gluon radiation is plotted as a function of η. The gluon radiation from photon exchange is exponentially suppressed between the jets with respect to events with single gluon exchange. (Figure courtesy of B. Fletcher.)

exchange has a large suppression due the cancellation of initial and final-state radiation. The resulting radiation pattern for photon exchange is exponentially suppressed between the jets.

2.8.2 The QCD Color-Singlet Radiation Pattern

In leading order QCD, only the exchange of a color triplet (quark) or color octet (gluon) is allowed. However, at higher orders, the exchange of two gluons in a color-singlet state is possible [25]. This QCD color singlet has been suggested as a model for the Pomeron [26].

Chehime and Zeppenfeld [5] have calculated the radiation pattern for "two-gluon" Pomeron exchange from perturbative QCD for t-channel quark-quark scat-

tering, $qq' \to qq'g$. They assume that the Pomeron is explicitly exchanged between the quarks and not between one of the quarks and the radiated gluon, since the radiated gluon from this process tends to go into the region between the jets. By removing this diagram from the calculation, the remaining processes lead to a mechanism for rapidity gap production.

To illustrate the radiation pattern, the gluon is fixed with $p_T = 2\,\mathrm{GeV}$ and the quarks are fixed at $\eta = \pm 3$ with $E_T = 30\,\mathrm{GeV}$. Figure 2-15 shows the soft gluon radiation pattern obtained for two-gluon Pomeron exchange. The radiation patterns for single gluon exchange and photon exchange are also plotted for comparison.

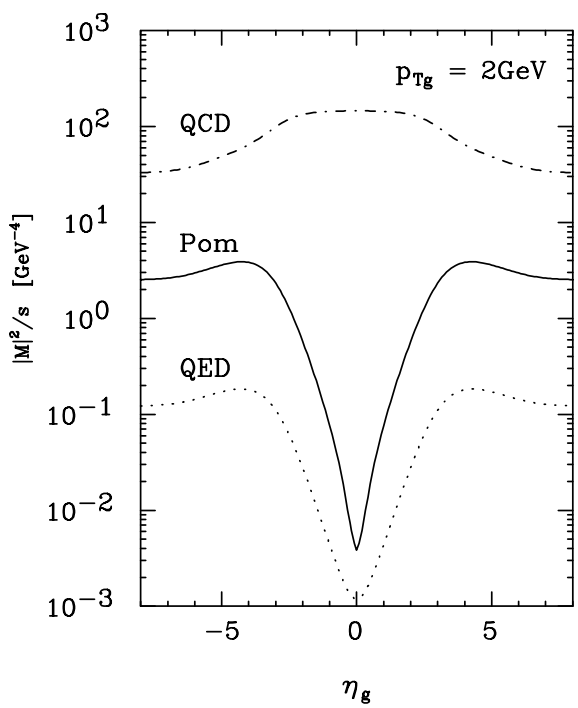

Figure 2-15: Radiation pattern in two-jet events for an additional 2 GeV gluon from two-gluon Pomeron exchange (solid line) compared to single gluon exchange (dashed line) and photon exchange (dotted line) [5]. The quark jets are fixed at $\eta = \pm 3$. The relative probability for gluon radiation is plotted as a function of η of the gluon. (Figure courtesy of D. Zeppenfeld.)

The radiation pattern for the two-gluon Pomeron clearly resembles that for photon exchange: gluon emission between the jets is strongly suppressed. It is

expected that at higher orders, this pattern should survive additional gluon radiation due to color coherence effects [5]. Therefore, two-gluon Pomeron exchange is expected to produce a rapidity gap topology similar to that in photon exchange.

Interestingly, if the gluon radiation is not required to be soft, the radiation pattern for the two-gluon Pomeron resembles that for single gluon exchange and no rapidity gap is expected [5]. Thus the hard radiated gluon can resolve the individual gluons in the Pomeron and the Pomeron no longer behaves in an effective color-singlet state. The resulting radiation pattern approaches the single gluon exchange radiation pattern.

2.8.3 Out-of-cone Radiation in Color-Singlet Exchange

Clearly, the rapidity gap event topology shown in Fig. 2-13 is idealized. Although radiation between the jets is highly suppressed as shown in Fig. 2-14 and Fig. 2-15, the hadronization of the jets can produce particles which "leak" outside of a fixed jet cone. This *out-of-cone radiation* is a concern since jet fragmentation in color-singlet exchange events can produce particles in the $\Delta\eta_c$ region. These particles, if detected, would "spoil" the rapidity gap.

The amount of out-of-cone radiation for color-single exchange can be qualitatively estimated from color coherence considerations. In the angular ordering approximation, radiation is limited to a cone around a radiated parton (approximated by the observed jet) defined by the initial radiation angle of the parton (§2.3.3). Therefore for a jet scattered at an angle θ_j, the radiation is limited to a cone of half-angle θ_j and no radiation is allowed for angles $\geq 2\theta_j$. As the jet scattering angle θ_j decreases (η_j increases) the radiation is restricted to physically smaller cones. Although the maximum angle for radiation decreases as θ_j decreases, the angular ordering requirement results in an approximate cone in η-ϕ space for $|\eta| > |\eta_j|$ whose radius approaches a constant value as shown in Fig. 2-

16. For jets with $|\eta_j| \gtrsim 2$ all radiation is limited to an effective cone with radius $R \leq \ln 2 \approx 0.69$. However, since angular ordering is only an approximation for color coherence this constraint should not be taken literally. Clearly, some out-of-cone radiation is expected although it should be suppressed for jets with $|\eta_j| \gtrsim 2$.

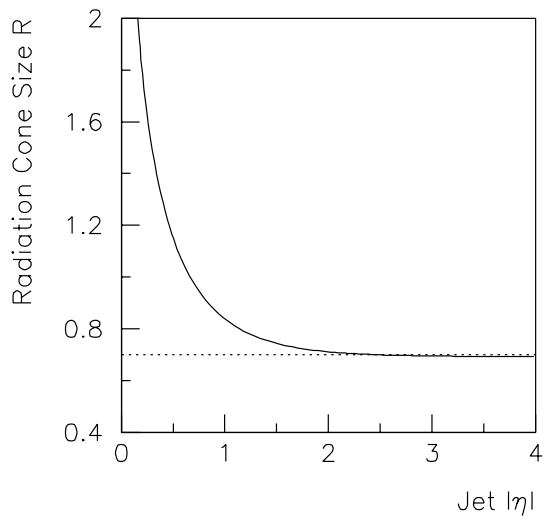

Figure 2-16: The cone size for allowed radiation (with $\eta > \eta_j$) from the angular ordering approximation as a function η_j (solid curve). The cone size approaches $\ln 2 \approx 0.69$ for large $|\eta_j|$. For jets with $|\eta_j| \gtrsim 2$ all radiation is limited to a cone of radius $R \approx 0.7$ (dotted line).

Another estimate of out-of-cone radiation can be obtained by a kinematical argument. According to Bjorken [27], the average number of final-state particles emitted outside a cone of radius R is roughly given by

$$N_{gap} \approx \frac{1}{2}\left(\frac{dN}{d\eta}\right) \mathrm{e}^{-2R}$$

where $dN/d\eta$ is the average particle multiplicity per unit η (i.e. the height of the rapidity plateau between jets). Assuming $dN/d\eta \approx 4$ [24] (at the Fermilab Tevatron) and a cone size of $R = 0.7$, then N_{gap} is on the order of one particle. Therefore, a large portion of events may in fact have at least one particle leaking into the gap near the jets.

The arguments given above are only qualitative and indicate that the magnitude of out-of-cone radiation is not well understood. For this reason it is not expected to be accurately simulated in Monte Carlo programs, most of which utilize the angular ordering approximation. While the angular ordering approximation can account for the overall interference effects in parton showers, the strict angular requirement allows absolutely no radiation outside a certain radius from the jet. More likely, the radiation is exponentially suppressed away from the jet, as suggested by Fig. 2-14 and Fig. 2-15, although the actual rate of suppression is difficult to calculate theoretically.

2.9 Rapidity Gap "Production" Rates

Jet production cross sections for color-singlet exchange processes, can be calculated from perturbation theory. However, these cross sections are more conveniently expressed in terms of a ratio with respect to inclusive jet production cross section—i.e. as the fraction of color-singlet exchange to total jet production. The cross section for color-octet and color-triplet (gluon or quark) exchange is a good estimate for inclusive jet production since it is in general much larger than the cross sections for color-singlet exchange.

Although rapidity gaps are expected to occur primarily in color-singlet exchange processes, color-triplet and color-octet exchange processes can also produce rapidity gaps due to fluctuations in the particle multiplicity between the jets. For events with small pseudorapidity separation between the jets ($\Delta\eta_c \gtrsim 0$), a large fraction is expected to have a rapidity gap due to the substantial probability for fluctuations to zero particles between the jets. However, the fraction is expected to decrease sharply as $\Delta\eta_c$ increases due to the larger phase space for hadronization, which increases the average particle multiplicity between jets and makes a fluctuation to zero particles much less likely. Therefore, it is expected that color-octet

and triplet exchange will dominate the rapidity gap production at small $\Delta\eta_c$, while for large $\Delta\eta_c$ the color-singlet contribution dominates.

2.9.1 Electroweak Color-Singlet

Jet production cross sections from electroweak exchange can be calculated from quantum electrodynamics. For small angle quark scattering (large $\Delta\eta_c$), the cross section for jet production via photon exchange can be written [28]

$$\frac{d\sigma_{EW}(p\bar{p} \to q(x_1)q(x_2) + X)}{d\eta_1\, d\eta_2\, dp_T^2} = \frac{4\pi\alpha^2}{x_1 x_2 p_T^4} Q_p(x_1) Q_{\bar{p}}(x_2)$$

where $Q(x) = f(x)$ denotes the quark distribution function (§2.1). The pseudorapidity separation of the jets is given by $\Delta\eta = |\eta_1 - \eta_2| = \ln(x_1 x_2 s/p_T^2)$, where $\sqrt{s} = 1.8$ TeV.

However, since QED jet production is suppressed compared to QCD jet production due to the relative coupling strengths, a more useful quantity is the ratio of electroweak to QCD jet production. For t-channel quark scattering, Bjorken [3] calculates the ratio to be

$$\frac{\sigma_{EW}}{\sigma_{QCD}} \approx \frac{9}{32}\left(\frac{\alpha(Q^2)}{\alpha_s(Q^2)}\right)^2 \sim 10^{-3},$$

which is only weakly dependent on jet transverse momentum through the coupling constants. Thus the rate of jet production via photon exchange is small compared to QCD inclusive jet production, and observation of rapidity gaps from electroweak exchange would require a large sample of jet events with large jet pseudorapidity separations.

2.9.2 QCD Color-Singlet

In contrast to the electroweak jet cross section, the QCD color-singlet, as modeled by the two-gluon Pomeron, is believed to have a significant cross section. Naively,

the ratio of two-gluon exchange jet production to single gluon exchange is proportional to $1/\alpha_s^2$ from the extra two vertices associated with the additional gluon exchange. However, Bjorken [3] finds a significant two-gluon exchange contribution to the total jet cross section. The ratio of the two-gluon exchange cross section to the single gluon exchange cross section has been roughly estimated to be [3]

$$\frac{\sigma_{QCD}^{singlet}}{\sigma_{QCD}} = \frac{1}{2}\left(\frac{4\pi}{33-2n_f}\right)^2 \approx 0.11.$$

Thus approximately 10% of jet events are expected to produce rapidity gaps from QCD color-singlet exchange, independent of jet transverse momentum.

2.9.3 Color Octet/Triplet Production

Typically the color flow in color-octet or color-triplet exchange (collectively referred to as color-octet exchange due to the dominance of gluon exchange) fills η-ϕ space with particles as shown in Fig. 2-9. It is possible, however, for rapidity gaps to arise from fluctuations in the particle multiplicity between the jets. In addition, a small fraction of events can undergo large-angle t-channel or u-channel color-octet exchange in which the color flow looks like that in Fig. 2-12, due to large-angle scattering of the hard partons.

Color Octet Fluctuations

The particle production (hadronization) between jets in color-octet exchange is expected to be qualitatively similar to that in e^+e^- jet production and nondiffractive inelastic scattering. Therefore, the distribution of particles between jets is expected to have a rapidity plateau and as the pseudorapidity separation between the jets increases, the average particle multiplicity (number of particles) is expected to increase roughly linearly with $\Delta\eta_c$. In addition, the particle multiplicity distribution (for a given $\Delta\eta_c$) is qualitatively expected to follow a negative binomial

(NB) distribution:

$$P(n) = \binom{n+k-1}{k-1}\left(\frac{\bar{n}}{k+\bar{n}}\right)^n \frac{1}{(1+\bar{n}/k)^k}$$

where n is the particle multiplicity, $\bar{n}$ is the average particle multiplicity, and k is a measure of the distribution width. The negative binomial distribution has been phenomenologically successful in describing multiplicity distributions in e^+e^-, $p\bar{p}$ minimum bias data and other hadron-hadron collider experiments although at high center-of-mass energies some deviations from this distribution have been observed [23, 29]. The negative binomial distribution has also been predicted from QCD assuming a local parton-hadron duality in which soft gluon radiation multiplicity corresponds to final-state particle multiplicity [30], although higher order effects produce slight deviations [31].

The combination of a flat rapidity plateau between jets and a negative binomial distribution leads to the following qualitative prediction: for small $\Delta\eta_c$ the fraction of jet events with a rapidity gap is large but decreases rapidly as $\Delta\eta_c$ increases. Fig. 2-17 shows the fraction of jet events from color-octet exchange with a rapidity gap as a function of $\Delta\eta_c$ for various negative binomial distributions. The shape of the fraction is sensitive to both the mean number of particles $\bar{n}$ per unit pseudorapidity in the plateau (a) and the width of the negative binomial distribution (b). The actual shape of the fraction and the suppression for large $\Delta\eta_c$ is not well-known, but a PYTHIA [32] Monte Carlo study indicates that the fraction of gap events for $\Delta\eta_c > 2$ is less than 10^{-5} [28], although this includes spectator interactions which lowers the number by about an order of magnitude (see section §2.9.5).

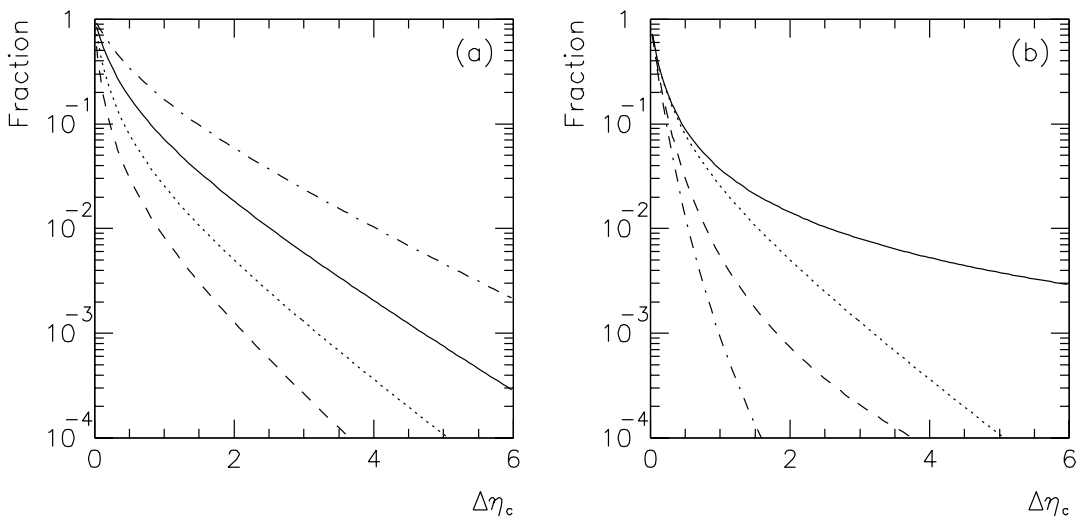

Figure 2-17: The fraction of jet events with a rapidity gap as a function of $\Delta\eta_c$ from color-octet exchange assuming various negative binomial particle multiplicity distributions. The solid line in (a) assumes a minimum bias NB multiplicity distribution estimated from Ref. [23] ($\bar{n}_{mb} = 6, k_{mb} = 0.3\Delta\eta_c + 1.5$) while the dotted, dashed and dot-dashed curves show the effect of changing the average multiplicity to 2, 3, and 1/2 times $\bar{n}_{mb}$. Figure (b) shows the effect of varying the k parameter for $\bar{n} = 2\bar{n}_{mb}$. The dotted line is identical to the dotted line in (a) and has a minimum bias-like k parameter (linear in $\Delta\eta_c$) while the solid, dashed and dot-dashed curves correspond to constant values of $k = 1.5$, $k = 3.5$ and $k = 7$ respectively.

Large-Angle Quark Scattering

Although the majority of rapidity gap events in color-octet exchange arise from fluctuations, color singlet-like topologies as shown in Fig. 2-12 can occur if hard quarks are scattered at large angles ($\theta \gg 90°$) in the t-channel or at small angles in the u-channel. In this case, the color flow is identical to that in color-singlet exchange since the strings do not stretch across the event as shown in Fig. 2-9 (top).

Processes which can produce a rapidity gap include the quark-quark processes $qq \to qq$, $qq' \to qq'$, $q\bar{q} \to q\bar{q}$, and $q\bar{q}' \to q\bar{q}'$, where q and q' denote distinct quark flavors. These quark-quark scattering processes contain t-channel interactions which can lead to rapidity gaps at large angles. The u-channel process, which is highly suppressed at small angles, arises only in qq scattering due to the nature

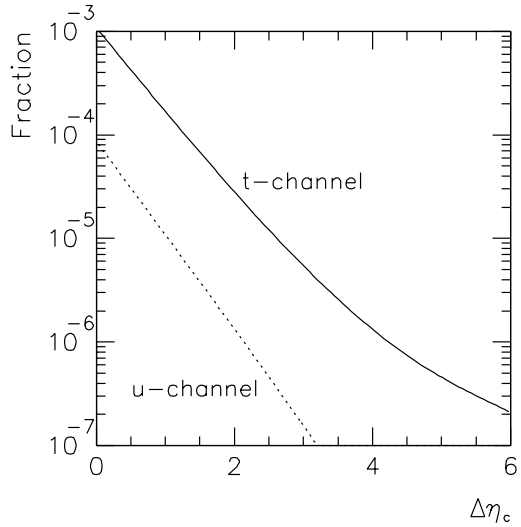

Figure 2-18: The fraction of jet events with a rapidity gap as a function of $\Delta\eta_c$ from large-angle quark scattering for jets with $p_T = 30\,\mathrm{GeV}$. The dashed and dotted lines represent the contribution from t-channel and u-channel processes respectively.

of the identical quarks. Other t-channel processes such as $gg \to gg$ and $qg \to qg$ are not expected to produce rapidity gaps in large-angle scattering due to the color flow (strings) across the event. Annihilation processes (s-channel) such as $gg \to qq$ and $q\bar{q} \to q'\bar{q}'$ also are not expected to produce rapidity gaps since the color flow is similar to that in $e^+e^- \to q\bar{q}$ (see §2.6.1).

The fraction of events with a rapidity gap from t-channel and u-channel exchange has been estimated by convoluting the appropriate leading order (α_s) subprocess cross sections with parton distribution functions of Ref. [9] (with no Q^2 evolution). The resulting probability for producing a rapidity gap from t-channel and u-channel quark processes as a function of $\Delta\eta_c$ is shown in Fig. 2-18 for jets with $p_T = 30\,\mathrm{GeV}$. Both the t-channel and u-channel contributions fall rapidly with $\Delta\eta_c$, and for large jet separations these processes are highly suppressed.

2.9.4 Inclusive Gap Production

The expectations given above for rapidity gap production from color-singlet and color-octet exchange can be combined to give a qualitative prediction for σ_{gap}/σ as shown in Fig. 2-19. The figure shows the components of σ_{gap}/σ from electroweak exchange, QCD color-singlet exchange, fluctuations in color-octet exchange, and the fraction from large-angle quark scattering. The solid line shows the sum of all the contributions and assumes that the QCD color-singlet Pomeron exists at the predicted level.

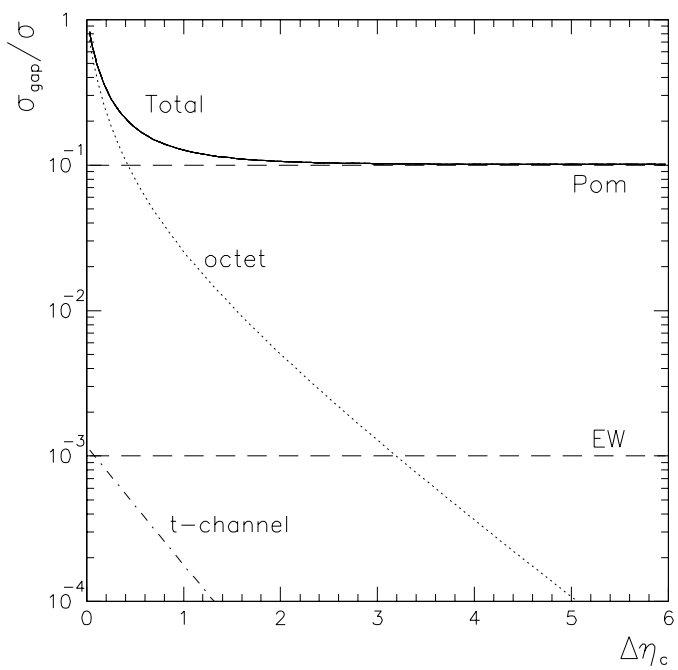

Figure 2-19: Contributions to σ_{gap}/σ as a function of $\Delta\eta_c$. Shown are the contributions to the fraction from electroweak exchange) [28] (EW), QCD color-singlet exchange [3] (Pom), fluctuations in color-octet exchange assuming $\bar{n} = 2\bar{n}_{mb}$ and $k = k_{mb}$ (octet), and the fraction from large-angle quark scattering processes (t-channel). The solid line is the weighted sum of all contributions.

2.9.5 Spectator Interactions and Survival of the Gap

Additional parton-parton spectator interactions are expected to occur in most hard scattering events (§2.3.5), and a rapidity gap will not be observed in the final state if spectator interactions produce particles between the jets. Spectator interactions arise from the abundance of soft gluons in the proton and antiproton caused by the evolution of the parton distribution functions, and the large physical overlap of the proton and antiproton when a hard interaction occurs.

The probability of an additional spectator interaction can be naively calculated [3, 4, 8] in the so-called "impact parameter space" picture [33]. This model assumes that the proton (antiproton) has a certain parton density distribution $\rho(r)$ in the plane transverse to its directions of motion, where r is the distance from the center of the hadron in the impact plane. The hard interaction probability, given a certain *impact parameter* b between the proton and antiproton, is simply the integrated overlap of the parton densities of the proton and antiproton as shown in Fig. 2-20. Therefore, the cross section for the hard interaction is a convolution of parton densities integrated over all possible impact parameters b of the proton and antiproton [3]:

$$\sigma_{hard} \approx \sigma_0 \int d^2b\, d^2r\ \rho(r)\rho(b-r) \equiv \sigma_0 \int d^2b\ \omega(b),$$

where σ_0 is the total inelastic $p\bar{p}$ cross section and the convolution $\omega(b)$ is typically assumed to be Gaussian.

The probability for a soft interaction can be determined in a similar way except that soft parton impact parameter densities must be used. The average number of soft interactions per $p\bar{p}$ collision is proportional to the soft overlap density (effective soft parton luminosity) and is Poisson distributed. Thus the probability that the

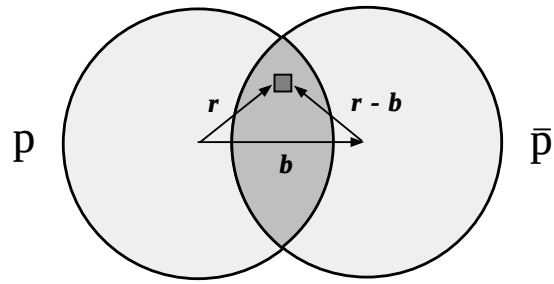

Figure 2-20: Representation of the overlap of a proton and antiproton with impact parameter b. The density element (shaded square) is the product of parton densities for the proton and antiproton. The total overlap (dark shaded region) is the convolution of the parton densities integrated over all r in the overlap region. The overlap is proportional to the probability for an interaction.

proton and antiproton do not interact with an additional soft interaction is

$$P_0^{soft}(b) \quad = \quad \mathrm{e}^{-\nu\chi(b)}$$

where $\chi(b)$ is a convolution of soft parton impact parameter densities (typically assumed to be Gaussian) and ν is a constant. The probability for no additional spectator interactions can therefore be written as [3]

$$\langle |S|^2 \rangle \quad = \quad \frac{\int d^2b\ \omega(b) P_0^{soft}(b)}{\int d^2b\ \omega(b)}.$$

Thus $\langle |S|^2 \rangle$ represents the integrated probability for no additional soft interactions given that a hard interaction has occurred with impact parameter distribution $\omega(b)$.

Several models [3, 4, 8] have been used to calculate $\langle |S|^2 \rangle$, although they typically only vary in their assumptions of the effective radius of the hard and soft parton densities and the parameter ν. These parameters are constrained by the measured total and inelastic cross sections. The results from the various models are consistent within a factor of three and predict a survival probability for rapidity gap production ranging from 9.6% to 32.6% at Tevatron energies with weak dependence on $\Delta\eta_c$ and jet transverse energy [3, 4, 8]. In addition, a PYTHIA [32] Monte Carlo study indicates that $\langle |S|^2 \rangle \approx 15\%$ for jets with $p_T > 30\,\mathrm{GeV}$ [34].

Although the survival probability of Eq. 2.3 gives the probability for no spectator interactions accompanying the hard interaction, rapidity gap events which do have a spectator interaction can in fact "survive" due to fluctuations in the particle multiplicity of the spectator interactions. The rapidity gap events that do not survive are called "zombies" (due to Fletcher) since they are spoiled by spectator interactions. Therefore, a more appropriate estimate of the probability for the survival of a rapidity gap is

$$S(\Delta\eta_c) \quad = \quad \langle |S|^2 \rangle + (1 - \langle |S|^2 \rangle) P_{n=0}^{spect}(\Delta\eta_c)$$

where $P_n^{spect}(\Delta\eta_c)$ is the multiplicity distribution between the jets from spectator interactions. The expected qualitative behavior of S is shown in Fig. 2-21 assuming that the spectator particle multiplicity is similar to minimum bias as in Ref. [23] and that $\langle |S|^2 \rangle = 15\%$. For small $\Delta\eta_c$, S is large but falls rapidly with $\Delta\eta_c$. At large $\Delta\eta_c$, however, $S \approx \langle |S|^2 \rangle$ since fluctuations to zero multiplicity become much less likely.

2.10 The Rapidity Gap Fraction

The fraction of observable rapidity gap events, called the *rapidity gap fraction*, depends on both the cross section for producing a rapidity gap from the hard scattering (σ_{gap}) and the probability of the gap surviving spectator interactions (S). The gap fraction is defined as

$$f(\Delta\eta_c) \quad = \quad \frac{\sigma_{gap}(\Delta\eta_c) \cdot S(\Delta\eta_c)}{\sigma(\Delta\eta_c)} \tag{2.3}$$

where $\sigma(\Delta\eta_c)$ is the inclusive cross section for producing jets with a separation of $\Delta\eta_c$ between the edges of the jet cones.

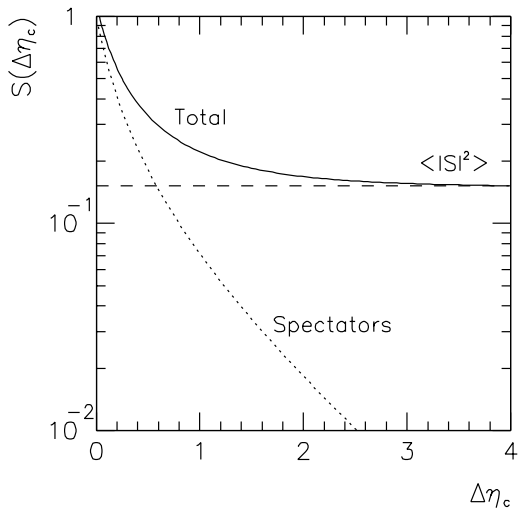

Figure 2-21: The expected behavior for $S(\Delta\eta_c)$, the probability for a rapidity gap surviving spectator interactions. The dotted curve shows the fluctuations to zero multiplicity in $\Delta\eta_c$ assuming that spectator interactions look like minimum bias events while the dashed curve corresponds to a representative value of $S = \langle |S|^2 \rangle = 15\%$. The solid curve is the sum of the dotted and dashed curves and shows the predicted behavior of $S(\Delta\eta_c)$.

2.10.1 Qualitative Expectation

The expectations for rapidity gap production from color-singlet and color-octet exchange (Fig. 2-19) and the probability of gap survival (Fig. 2-21) can be combined to give a qualitative prediction for the shape of the rapidity gap fraction $f = (\sigma_{gap}/\sigma)S$ as a function of $\Delta\eta_c$. The resulting prediction for the rapidity gap fraction is shown in Fig. 2-22, assuming a QCD color-singlet or only an electroweak color-singlet. If the QCD color-singlet exchange process exists, the rapidity gap fraction has a distinctive behavior: for small $\Delta\eta_c$, the fraction is large (~ 1) but falls quickly as $\Delta\eta_c$ increases, while for large $\Delta\eta_c$, the fraction becomes roughly constant at $f_{Pom} = (\sigma_{Pom}/\sigma)\langle |S|^2 \rangle \sim 0.015$. If the QCD color-singlet exchange process does not exist, the fraction is expected to decrease to much smaller values before eventually flattening at very large $\Delta\eta_c$. In addition, the gap fraction is expected to have very weak dependence on jet transverse momentum.

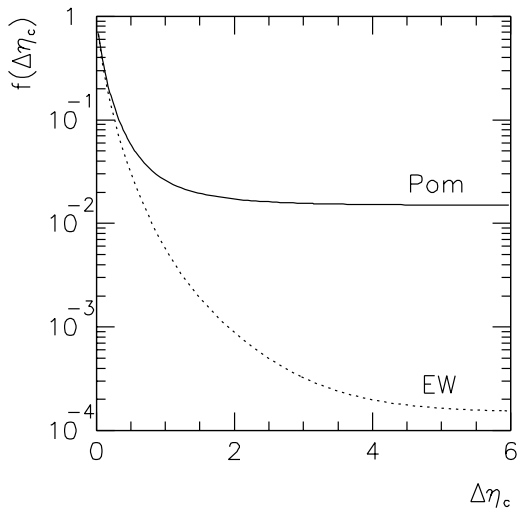

Figure 2-22: The qualitative prediction for the rapidity gap fraction $f(\Delta\eta_c)$ with (solid line) and without (dotted line) the QCD color-singlet. The prediction is obtained by multiplying $\sigma_{gap}(\Delta\eta_c)/\sigma(\Delta\eta_c)$ in Fig. 2-19 and $S(\Delta\eta_c)$ in Fig. 2-21.

The qualitative predictions given above can change if some fraction of the particles in each event are not observed experimentally. While inefficiencies typically do not affect the level of observed rapidity gaps from color-singlet exchange, they can strongly affect the contributions to the gap fraction from fluctuations—namely the color-octet contribution and spectator interactions. Figure 2-23 qualitatively shows the effect of particle detection inefficiencies on the measured gap fraction, assuming negative binomial distributions for the octet and spectators as in Fig. 2-22 with new mean multiplicity given by $\bar{n}_\epsilon = \epsilon\bar{n}$. For small inefficiencies, the measured gap fraction is similar in shape to the original gap fraction and $f(\Delta\eta_c)^{exp} \gtrsim f(\Delta\eta_c)$. For large inefficiencies, however, $f(\Delta\eta_c)^{exp} \gg f(\Delta\eta_c)$ and the gap fraction is dominated by fluctuations in particle multiplicity.

The qualitative predictions for the gap fraction given above are subject to large uncertainties. The color-octet contribution depends strongly on the shape of the actual multiplicity distribution between jets, which may not be negative binomial. The QCD color-singlet contribution—if in fact it exists—is also not

well-known and predictions for it vary by at least a factor of three (see §2.10.2 for another estimate). Although the electroweak color-singlet contribution is well known, its small magnitude requires a prohibitively large statistical sample to observe it unambiguously. Finally, the predictions for the survival of the gap are subject to large model-dependent uncertainties of at least a factor of three. Nonetheless, the predictions given above are useful for understanding the various components of the gap fraction and the resulting experimental measurement of the gap fraction.

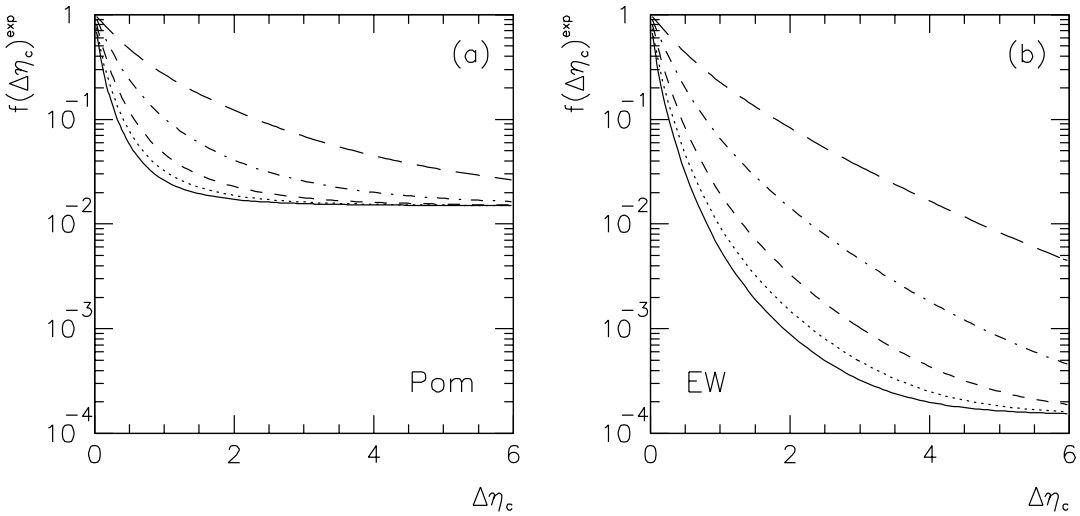

Figure 2-23: The effect of particle detection inefficiencies on the measured rapidity gap fraction $f(\Delta\eta_c)^{exp}$. The plots shown are with (a) and without (b) QCD color-singlet exchange respectively. The curves (bottom to top respectively) correspond to particle detection efficiencies of $\epsilon = 100$, 75, 50, 25 and 10%.

2.10.2 QCD Prediction

Del Duca and Tang [35] have calculated the rapidity gap fraction within perturbative QCD using BFKL theory [26, 36], which corrects the leading order calculation to take into account higher order effects in the large rapidity approximation. This

theory is used to calculate

$$R(\Delta y) \;=\; \frac{\sigma_{sing}(\Delta y)}{\sigma_{tot}(\Delta y)} \equiv \frac{\sigma_{gap}(\Delta y)}{\sigma_{tot}(\Delta y)},$$

which is the probability of having an *elastic* collision (no color exchange) at the parton level with jets separated by $\Delta y = |y_1 - y_2|$. This can be extended to calculate the *quasi-elastic* probability by defining a rapidity gap as having no parton radiation with transverse momentum larger than μ in the region between the jets:

$$R(\mu) \;=\; \frac{\sigma_{gap}(\mu)}{\sigma_{tot}} \equiv \frac{\sigma^{sing} + \sigma^{oct}_{gap}(\mu)}{\sigma_{tot}} \tag{2.4}$$

where σ^{sing} is the cross section for two-gluon color-singlet BFKL Pomeron [26] exchange, $\sigma^{oct}_{gap}(\mu)$ is the cross section for color-octet exchange with no parton radiation with $p_T > \mu$ between the jets, and σ_{tot} is the inclusive jet cross section. For $\mu \lesssim \Lambda_{QCD}$ the quasi-elastic probability reduces to the elastic case since the octet contribution is strongly suppressed.

Equation 2.4 has three cross section components: the total jet cross section and the color-singlet and color-octet exchange cross sections. The inclusive jet cross section for producing two jets each with $p_T > Q$ can be written

$$\frac{d\sigma_{tot}}{d(\Delta y)d\bar{y}}(p\bar{p} \to jj + X) = \int dp^2_{T1} dp^2_{T2} \prod_{i=p,\bar{p}} \left[G(x_i, Q^2) + \tfrac{4}{9} \sum_f Q_f(x_i, Q^2) \right] \frac{d\hat{\sigma}_{tot}}{dp^2_{T1} dp^2_{T2}}$$

where $x_p \approx \mathrm{e}^{y_1} p_{T1}/\sqrt{s}$ and $x_{\bar{p}} \approx \mathrm{e}^{-y_2} p_{T2}/\sqrt{s}$, $\Delta y = |y_1 - y_2|$ is the rapidity separation between the jets, $\bar{y} = (y_1 + y_2)/2$ is the rapidity boost of the system, and G and Q_f represent the gluon and quark parton distribution functions respectively. The cross section for color-singlet exchange in the t-channel is

$$\frac{d\sigma^{sing}}{d(\Delta y)d\bar{y}}(p\bar{p} \to j(x_p)j(x_{\bar{p}})) \;=\; \int d\hat{t} \prod_{i=p,\bar{p}} \left[G(x_i, Q^2) + (\tfrac{4}{9})^2 \sum_f Q_f(x_i, Q^2) \right] \frac{d\hat{\sigma}^{sing}}{d\hat{t}}$$

where $\hat{t} \approx -p^2_T$ and the additional factor of 4/9 in front of the quark parton distri-

bution is obtained from color charge considerations. The color-octet cross section is similar to the total cross section except that only additional gluon radiation with $p_{T_g} < \mu$ is allowed:

$$\frac{d\sigma^{octet}_{gap}}{d\Delta y d\bar{y}}(p\bar{p} \to jj + g(p_{T_g} < \mu)) = \int d\hat{t} \prod_{i=p,\bar{p}} \left[G(x_i, Q^2) + \tfrac{4}{9} \sum_f Q_f(x_i, Q^2) \right] \frac{d\hat{\sigma}^{oct}(\mu)}{d\hat{t}}.$$

Using these expressions, R can be rewritten in terms of the hard parton-parton elastic scattering cross sections:

$$R(\mu; x_p, x_{\bar{p}}) \;=\; w(x_p) w(x_{\bar{p}}) \frac{\hat{\sigma}^{sing}}{\hat{\sigma}_{tot}} + \frac{\hat{\sigma}^{oct}_{gap}(\mu)}{\hat{\sigma}_{tot}} \tag{2.5}$$

where w is the relative weight of parton distribution functions,

$$w(x) \;=\; \frac{G(x, Q^2) + (\frac{4}{9})^2 \sum_f Q_f(x, Q^2)}{G(x, Q^2) + \frac{4}{9} \sum_f Q_f(x, Q^2)}. \tag{2.6}$$

Thus w^2 represents the suppression of the color-singlet exchange compared to color-octet exchange due to the additional vertices from the two-gluon Pomeron. For gg scattering $w^2 = 1$ while for qq scattering the suppression approaches $(4/9)^2 \approx 0.2$.

The resulting ratio $R(\Delta\eta_c, \mu)$ calculated from BFKL theory is shown in Fig. 2-24 for 30 GeV jets and several values of μ. The elastic scattering probability ($\mu = 0$) has only weak $\Delta\eta_c \approx \Delta y - 2R$ dependence except for very large $\Delta\eta_c$, where Pomeron exchange becomes enhanced over gluon exchange. For experimentally accessible values of $\Delta\eta_c$, $R(\mu = 0) \approx 0.03$, which is within a factor of three of the prediction $\sigma_{Pom}/\sigma \sim 0.1$ discussed in §2.9.2. The elastic scattering ratio also has a slight jet p_T dependence: for 10 GeV jets $R \approx 0.05$ while for 40 GeV jets the ratio falls to about 0.025.

In contrast to the parton elastic scattering ratio, the probability for quasi-elastic scattering is large for small $\Delta\eta_c$, falls rapidly as $\Delta\eta_c$ increases and then rises again at large $\Delta\eta_c$. For small values of μ the quasi-elastic scattering ratio approaches the elastic ratio only at large $\Delta\eta_c$, while for larger μ, $R_{quasi} \gg R_{elastic}$. Since $\mu > 0$

corresponds to allowing "undetected" partons with $p_T < \mu$ into the gap region, this is qualitatively identical to having particle detection inefficiencies. Thus small values of μ ($\lesssim \Lambda_{QCD}$) correspond to high detection efficiencies and large values correspond to small efficiencies (compare to Fig. 2-24).

Using the above prediction for elastic parton scattering ($\mu = 0$), the rapidity gap fraction is predicted to be $f \approx \langle |S|^2 \rangle R(\mu = 0) \sim 5 \times 10^{-3}$ for $2 \lesssim \Delta\eta_c \lesssim 5$. However, since the BFKL calculation has an absolute normalization uncertainty, this prediction should be taken as order of magnitude only. Nevertheless, the dependence on $\Delta\eta_c$ for large $\Delta\eta_c$ is free from this uncertainty. Thus the gap fraction, or more specifically $R = \sigma_{Pom}/\sigma$, is expected to be relatively independent of jet p_T and $\Delta\eta_c$ for experimentally attainable values of $\Delta\eta_c$.

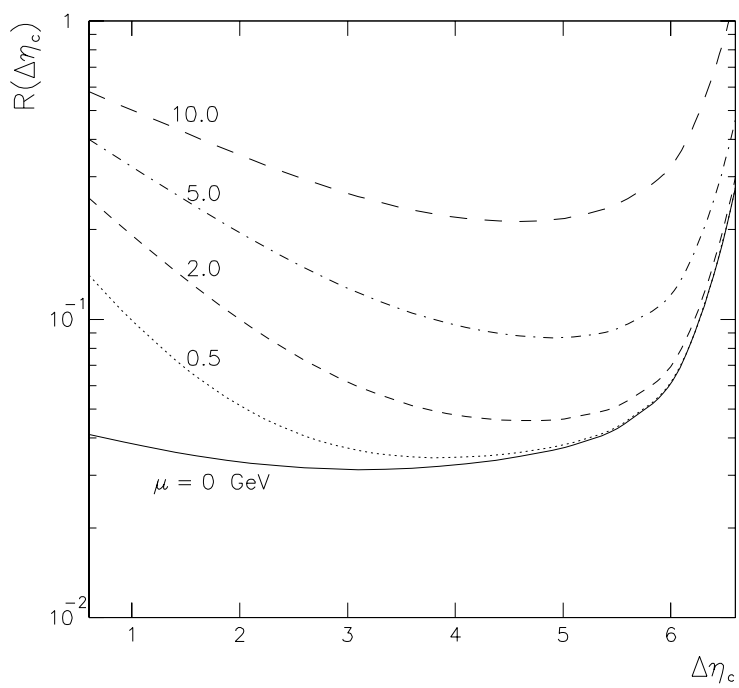

Figure 2-24: The ratio $R(\Delta\eta_c, \mu)$ for several values of μ. The elastic scattering probability corresponding to $\mu = 0$ has no octet contribution. For larger values of μ the quasi-elastic contribution dominates. (Data used for this plot courtesy of V. Del Duca.)

Chapter 3

The DØ Experiment

The DØ experiment [37] was proposed to study proton-antiproton collisions in the Fermilab Tevatron Collider at $\sqrt{s} = 1.8$ TeV. The physics under investigation is primarily large mass and high-p_T phenomena including: the search for the top quark, precision measurements of W and Z bosons and related tests of the Standard Electroweak Model, production and study of b-quark hadrons, tests of perturbative QCD, as well as searches for new phenomena.

3.1 The Fermilab Tevatron $p\bar{p}$ Collider

The Fermilab Tevatron $p\bar{p}$ Collider accelerates protons and antiprotons to energies of 900 GeV providing a center-of-mass colliding energy of $\sqrt{s} = 1.8$ TeV. The Tevatron is currently the highest energy particle accelerator in existence and provides a wealth of $p\bar{p}$ interactions for studying high energy physics.

The operation of the collider begins with protons originating as hydrogen ions. The ions are first accelerated to 750 KeV by an electrostatic field and subsequently accelerated to 200 MeV by a linear accelerator. The hydrogen ions are then passed through a carbon foil which strips off the electrons. The resulting protons are sent to a booster synchrotron (8 GeV) before entering the 3.7 mile circumference main ring which accelerates the protons to 120 GeV. In the main ring, the protons are

focused into six "bunches" of high density and steered into a fixed target in order to create antiprotons (in roughly the ratio one antiproton per 10^5 protons) which are subsequently focused and sent to a storage ring. Antiproton accumulation or "stacking" continues until a sufficient number ($\sim 10^{11}$) of antiprotons have been accumulated. The antiprotons are then injected in bunches into the main ring and accelerated in the direction opposite the proton bunches. As the final step, the protons and antiprotons are injected into the Tevatron and accelerated to 900 GeV.

Once the proton and antiproton beams have been injected into the Tevatron, they must be "scraped" in order to reduce the beam halo, a cloud of uncollimated particles surrounding each bunch, which arises from manipulating and steering the beams. Beam halo can cause undesirable effects in the detector, such as spurious charged tracks and anomalous calorimeter energy.

A typical collider physics run lasts approximately 20 hours, during which time protons in the main ring can be used to generate antiprotons for the next collider run. The instantaneous luminosity of the collider (i.e. the proton-antiproton flux, proportional to the average rate of $p\bar{p}$ collisions), depends on the bunch crossing time (3.5 μsec) and the density of protons and antiprotons per bunch. During colliding, the instantaneous luminosity decays exponentially from a peak initial value.

The Tevatron has two high luminosity interaction regions at which the CDF [38] and DØ detectors are situated. For the 1992-1993 collider run, instantaneous luminosities in these regions ranged from $0.5\times10^{30}\,\mathrm{cm}^{-2}\mathrm{sec}^{-1}$ to $8.7\times10^{30}\,\mathrm{cm}^{-2}\mathrm{sec}^{-1}$. In addition, at the DØ interaction region, the proton-antiproton collisions had a Gaussian longitudinal vertex distribution along the proton-antiproton beam direction (z-axis). The mean vertex position measured with respect to the center of the DØ detector was $z \approx -10\,\mathrm{cm}$ with a width of approximately 30 cm.

3.2 The DØ Detector

The DØ detector, shown in Fig. 3-1, consists of three major systems: the central detector, the calorimeter, and the muon system. The central detector consists of tracking and transition radiation detectors. It is used mainly to help identify charged particles (electrons, muons) and to determine the interaction vertex position. The calorimeter is used primarily to identify high-p_T electrons, photons and jets, as well as neutrinos which are measured as missing transverse energy ($\vec{\not{E}}_T$) in the calorimeter. The muon system is used to identify muons and measure their transverse momentum.

In the following description of the detector and its components, a right-handed coordinate system is adopted in which the z-axis is along the proton beam direction and the y-axis points up. In addition, the pseudorapidity η_d refers to *detector* η in which interactions are assumed to occur at the center of the detector ($z = 0$). Other coordinates used in the descriptions are the azimuthal angle ϕ and the polar angle θ, measured from the proton beam direction. The polar angle and pseudorapidity are related by $\eta = -\ln \tan(\theta/2)$.

3.2.1 The Central Detector

The central detector [39] consists of four subdetectors: a vertex detector, a transition radiation detector, and central and forward drift chambers as shown in Fig 3-2. The vertex detector and the central and forward drift chambers determine the trajectory of charged particles, while the transition radiation detector can be used to discriminate between electron and charged pions.

The transition radiation detector (TRD) utilizes the property that charged particles radiate photons when crossing a boundary between two materials with different dielectric constants. The energy of the radiated photons depends on the

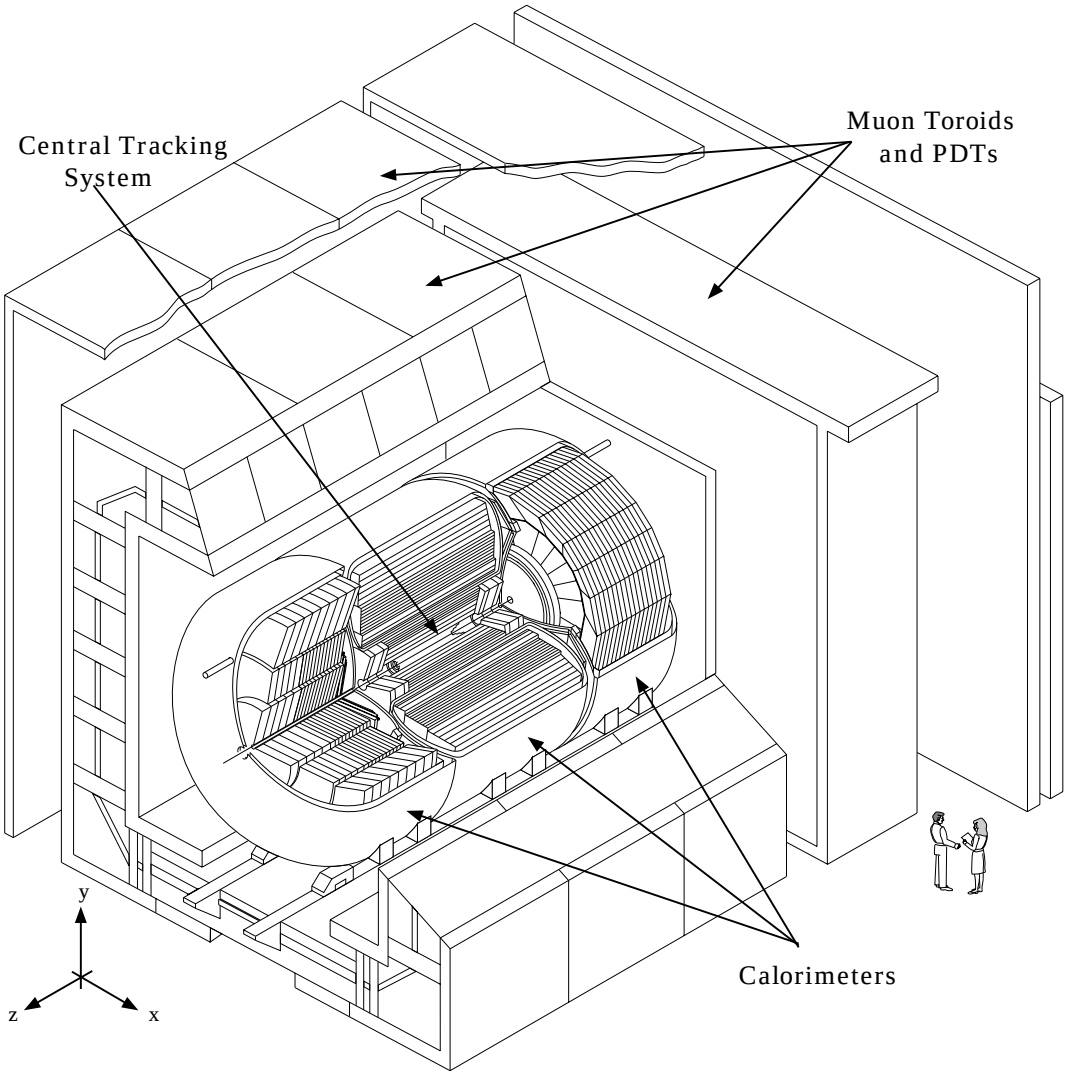

Figure 3-1: The DØ Detector.

Figure 3-2: The DØ Central Detector (cross sectional view).

Lorentz factor, which is inversely proportional to the square root of the mass of the charged particle. For electrons and charged pions of the same energy, the difference in energy of the radiated photons can be used to distinguish them.

The vertex detector, central drift chamber, and forward drift chamber each measure charged particle trajectories by utilizing a high electric field in an ionizable gas medium. A high energy charged particle passing through a tracking chamber ionizes the gas and the arrival time of the gas at the anode is measured. By combining timing signals from all "hit" anodes, the track trajectory can be reconstructed along with its goodness-of-fit parameters and errors. Reconstructed tracks are straight and give no information about particle momentum or charge since the DØ detector contains no central magnetic field.

The three primary tracking detectors are briefly described below:

- The vertex detector (VTX) is located closest to the interaction region just outside the Tevatron beam pipe, in order to minimize multiple scattering and extrapolation errors. The VTX consists of three concentric super-layers designed to accurately measure the longitudinal vertex position of an event.

- The central drift chamber (CDC), located outside the VTX and TRD, measures charged particle tracks with $|\eta_d| \lesssim 1$. It consists of four concentric layers of drift chambers. It can also be used to measure the vertex position of an inelastic collision.

- The forward drift chambers (FDC) are located on both sides of of the interaction region and measure charged particle tracks with $1 \lesssim |\eta_d| \lesssim 3$. The FDC can be used to determine the the interaction vertex when the CDC has an insufficient number of tracks for a vertex measurement.

3.2.2 The Calorimeter

The DØ calorimeter [37] was designed primarily to identify high-p_T objects originating from inelastic collisions (e.g. electrons or jets) and measure their transverse energy. The calorimeter has full pseudorapidity coverage out to $|\eta_d| \leq 4.1$ and partial (reduced depth) coverage for $4.1 < |\eta_d| \leq 4.5$. The calorimeter is divided into three distinct "cryostats", each designed to be a self-contained unit. The arrangement of the central (CC) and two end cap (EC) calorimeters is shown in Fig. 3-3.

Each calorimeter cryostat contains three separate calorimeter types designed to measure different types of energy deposition. The electromagnetic (EM) section, which lies just outside the tracking systems and closest to the interaction region, measures electromagnetic energy deposition (primarily from electrons and photons). The hadronic section, lying just outside the EM section, has two subsections that are used to measure hadronic shower energy deposition (primarily from jets). The hadronic section contains a fine hadronic (FH) section with good hadronic shower energy resolution, and a coarse hadronic (CH) section used primarily for energy containment. The operation of each will be discussed in greater detail later in this section.

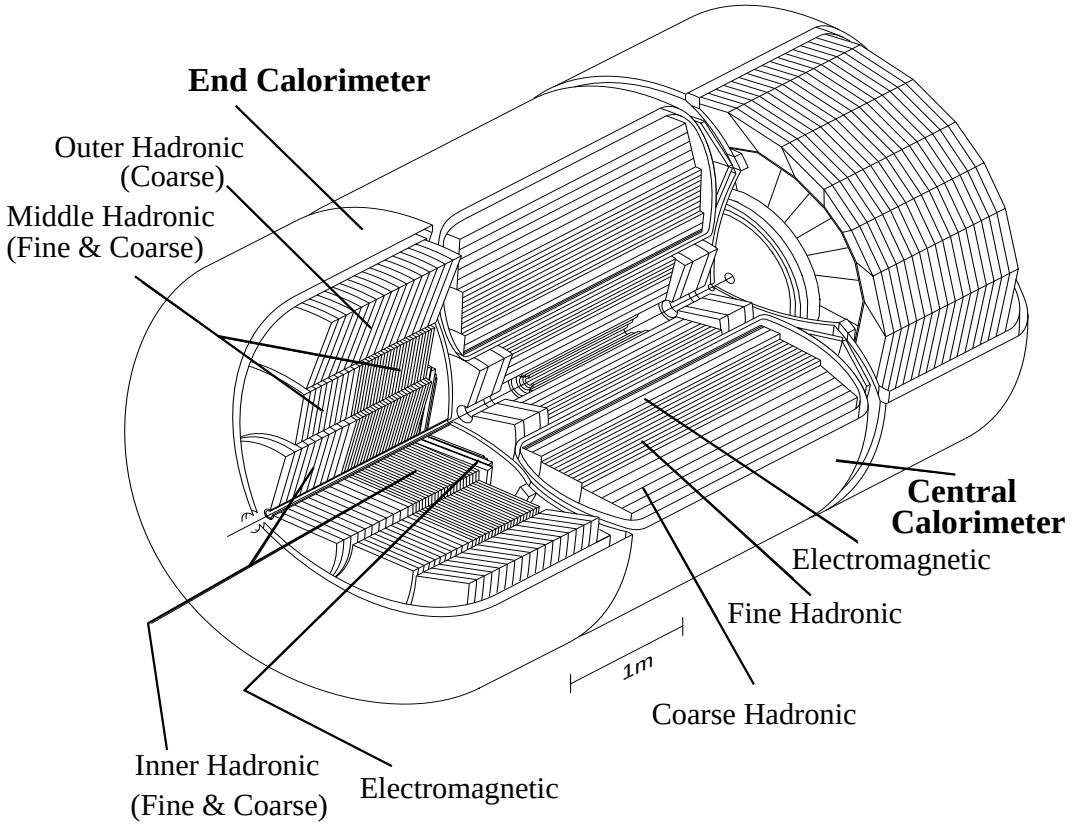

Figure 3-3: Cutaway view of the DØ calorimeter. The calorimeter consists of three cryostats (one central and two endcap) covering a large range in pseudorapidity. In addition, each cryostat contains an electromagnetic section and a hadronic section.

The calorimeter is finely segmented in both pseudorapidity and azimuthal angle (η-ϕ) in units of 0.1×0.1 as shown in Fig. 3-4. The segmentation is achieved with a "pseudo-projective" tower design in which each η-ϕ tower is approximated by a finite number of layers. Each layer has a geometry that does not project back to the center of the detector ($z = 0$). The pseudo-projective geometry does not significantly affect the energy measurement or position resolution and was implemented for construction simplicity.

The Fermilab main ring accelerator runs directly through the CH section of the calorimeter at $\phi \approx 1.8$ where the calorimeter is not fully instrumented. This is not a concern since typically only a small fraction of the calorimeter energy is measured in the CH section. However, as protons circulate in the main ring, they can deposit false energy in the CH section due to scattering out of the beam pipe. This problem is largely reduced by vetoing (ignoring) events which coincide with main ring activity (see §3.2.5).

Calorimeter Operation

The DØ calorimeter is based on a "sampling" design: particles deposit a fraction of their energy which is subsequently converted (via calibrated electronics and software) into a total energy measurement. The sampling design consists primarily of depleted uranium as an absorber and liquid argon as the active ionizing material. As particles pass through the dense absorber, they produce additional particles via various electromagnetic and nuclear processes. As the resulting "shower" of particles passes through the active sampling layer of argon, it ionizes the argon producing a charge that is read out and digitized by electronics. This signal is then converted to a total energy measurement. Many layers of absorber, ionizing material, and read-out boards (ganged together) are interlaced to achieve improved energy resolution.

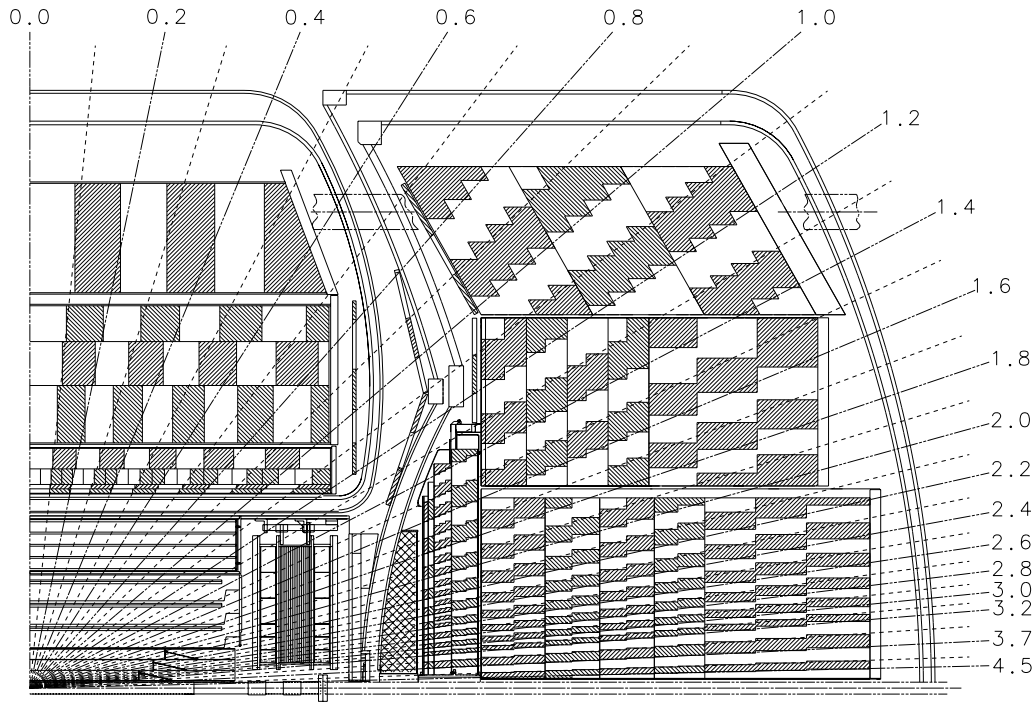

Figure 3-4: Cross sectional view of the calorimeter and central detector showing η coverage, which extends out to $\eta_d = 4.5$. The "pseudo-projective" calorimeter towers correspond to 0.1 unit in η and ϕ.

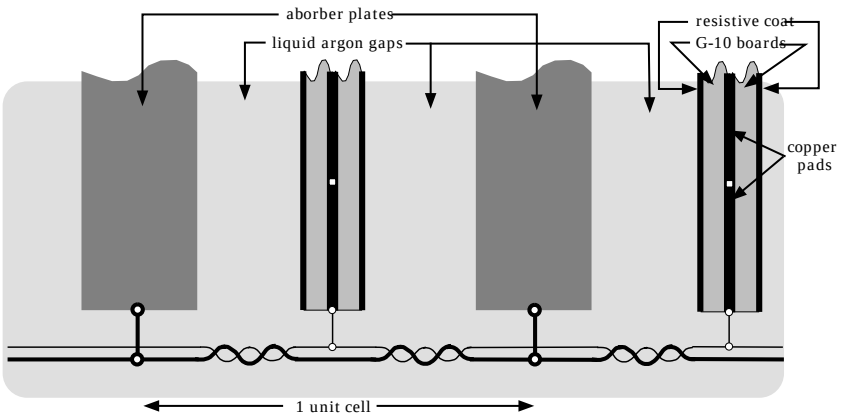

Figure 3-5: A typical calorimeter read-out cell (in cross section, not to scale).

A representative calorimeter read-out cell is shown in Fig. 3-5. The uranium absorber serves as the passive material which is held at ground. The read-out board lies in the liquid argon gap between absorber plates. It consists of a G-10 board, one side of which is copper coated. Both sides of the signal board are additionally coated with a resistive layer (on top of the copper) which is held at approximately 2.0 KV and serves as an anode and capacitor. Several of these individual cells are ganged to form one read-out cell or channel.

The signal from each cell is measured as follows: as charge moves towards the anode (resistive coating), an image charge is induced on the copper pad. The resulting signal is subsequently sent to (1) a charge sensitive preamp, which boosts the signal; (2) a shaping and sampling circuit which measures the accumulated charge; and (3) an analog to digital converter which puts the signal in a computer readable form. The signal is then pedestal subtracted to account for the average noise level. If the magnitude of the final signal is consistent with a small fluctuation in noise, the channel is not recorded (zero-suppressed) since it is consistent with zero signal.

Each of the three calorimeter types (the electromagnetic, fine hadronic and course hadronic), has a characteristic read-out cell design as follows:

- **Electromagnetic (EM) Section**: The EM section was designed to measure the energy of electromagnetic particles and absorbs almost all of the energy from electromagnetic showers. It has four longitudinal layers (in depth from interaction point) of read-out cells with thicknesses of 2, 2, 7, and 10 radiation lengths (X_0) [40]. The transverse segmentation is $\Delta\eta \times \Delta\phi = 0.1 \times 0.1$ except for the third longitudinal layer which is segmented with $\Delta\eta \times \Delta\phi = 0.05 \times 0.05$. This provides increased η-ϕ position resolution since typical electromagnetic showers deposit most of their energy in this layer. Figure 3-6 shows the segmentation of the EM section as a function of detector η and depth.

- **Fine Hadronic (FH) Section**: The FH section was designed to measure the energy of hadronic particles. It has a transverse segmentation of $\Delta\eta \times \Delta\phi = 0.1 \times 0.1$ and three to four longitudinal read-out layers (see Fig. 3-6). These layers give a total of about five interaction lengths [41].

- **Course Hadronic (CH) Section**: This section consists of at least one layer of either very thick copper or stainless steel absorber plates which amount to about four interaction lengths (see Fig. 3-6). The CH is designed not for optimal energy resolution but for energy containment of calorimeter showers.

Calibration

The calorimeter was studied and calibrated at the DØ test beam [42]. Different sections of the calorimeter were tested using monoenergetic beams of electrons and charged pions ranging from 2–150 GeV. The test beam studies determined that the calorimeter response is linear to within less than 1% for electrons above 10 GeV and charged pions above 20 GeV. For low energy particles, however, the response of the calorimeter is nonlinear, which significantly affects low energy particle detection

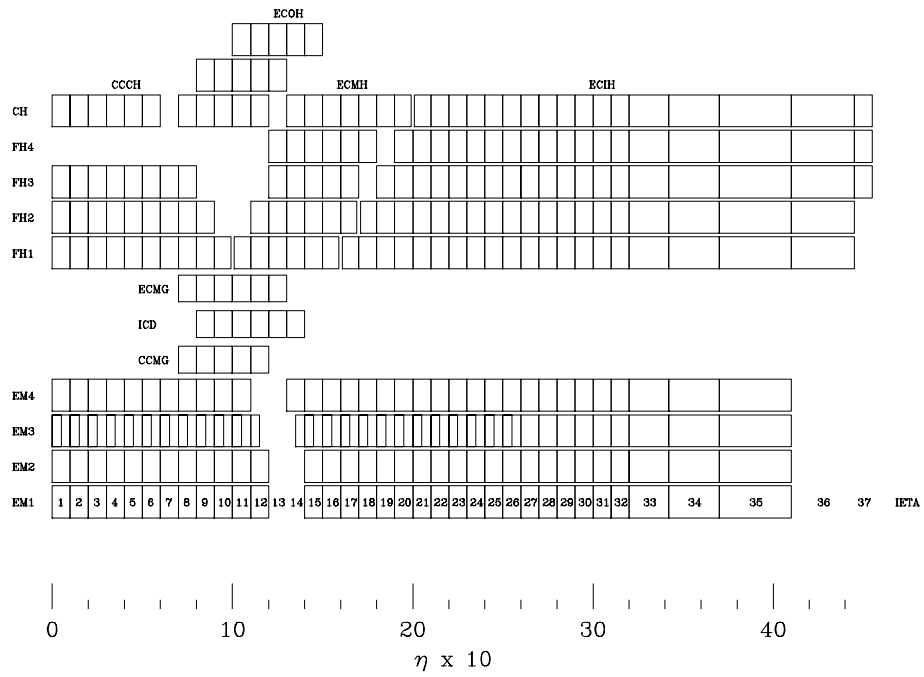

Figure 3-6: Segmentation of the calorimeter in towers of η_d for each layer and section of the calorimeter (shown schematically).

efficiencies and jet energy response.

The energy resolution for electrons and charged pions was also measured from the test beam data. The calorimeter resolution was determined to be approximately $15\%/\sqrt{E}$ for electrons and $50\%/\sqrt{E}$ for charged pions. The jet energy resolution (determined offline, see §4.5) is approximately $85\%/\sqrt{E}$.

Additional fine-tuning calibration of the calorimeter was done online, between periods of Tevatron collider operation. Roughly once every other day, the electronics of each calorimeter read-out channel was calibrated by sending various pulsed signals through each preamp. The resulting calibration data was then analyzed to determine gain corrections for each preamp. These corrections were subsequently stored in a database and used to correct each calorimeter read-out channel during offline data reconstruction.

Noise

The calorimeter is subject to both uranium and electronic noise. Uranium noise (due to beta decay from the uranium absorber plates) produces a non-Gaussian distribution with a long high energy tail, while electronic noise produces a symmetric Gaussian distribution. Channels with signals that are consistent with small fluctuations in noise are "zero-suppressed" (ignored) in order to significantly reduce the number of channels recorded per event. These channels are not useful for measuring the transverse energy of particles or jets since they nominally only contain energy due to noise.

The noise distribution of each channel is measured roughly once per day during collider operation by taking approximately 1000 events with no physics trigger or Tevatron beam to determine the mean noise "pedestal" and the standard deviation of each channel using a Gaussian fit. The mean and width are subsequently used during online data taking to determine if a channel is within $\pm 2\sigma$ of the pedestal value. Cells within this window are not recorded and assumed to be noise. Zero-suppression reduces the number of recorded channels by more than a factor of 10, which allows a smaller recording time per event.

Zero suppression has little effect on high-p_T electrons and photons measured in the calorimeter but does introduce a small but significant (and correctable) effect on the energy of jets measured in the calorimeter. This effect is due to the high energy tail of the non-Gaussian uranium noise. Fluctuations in the uranium noise after zero-suppression produce a small positive mean energy for each channel (about 1 MeV per calorimeter tower. Although this energy is small, it can add a few GeV of energy to reconstructed jets due to the large number of channels (~ 2000) required to reconstruct jets. Noise and zero suppression clearly also affect low energy particle detection due to fluctuations obscuring real energy deposition.

The noise distributions produced in each section of the calorimeter (EM, FH

Section	CC ($\eta_d < 1.2$)	EC ($\eta_d > 1.2$)
EM	10 MeV	10 MeV
FH	60 MeV	30 MeV
CH	75 MeV	55 MeV
MG	30 MeV	30 MeV
ICD	8 MeV	15 MeV

Table 3-1: Typical calorimeter noise (pedestal) widths by calorimeter section and cryostat.

and CH) differ due to differences in the geometry of the read-out cells. Cells with a smaller area have less noise compared to those with larger area since calorimeter noise (both electronic and that due to the uranium) is proportional to the area (capacitance) of the read-out cell. Typical noise widths for the different sections of the calorimeter are given in Table 3-1. The EM section has the lowest level of noise due to its location closest to the interaction point, since the pseudo-projective towers are physically smaller. Conversely, the CH section has the highest noise level due to the relatively large size of the readout cells. Although the noise distributions are substantially different for each section of the detector, these differences are taken into account on a cell-by-cell basis and therefore do not significantly affect energy measurements of high-p_T objects.

Unfortunately, the noise distributions can have a large effect on low energy particle detection ($E < 1\,\mathrm{GeV}$). The observation of low energy particles in the calorimeter can be obscured by fluctuations in noise, which depend on calorimeter section. The typical noise "width" in the EM section is about 10 MeV, while it is about four times larger in the FH section. The CH section is even noisier due to its large cell geometry. The EM section is best suited (most efficient) for low energy particle detection due to its comparatively low level of noise. In addition, the lower noise level reduces the probability of misidentifying fluctuations in noise as low energy particles. The hadronic (FH and CH) sections only marginally increase low energy particle detection efficiency due to their significantly higher noise level.

Occasionally certain calorimeter channels may become ill-behaved due to electronics failures or other problems. These so-called "hot channels" can give false energy measurements either regularly or intermittently. In general these channels are not suppressed unless they are "on" very frequently with a large energy for a long time (on the order of days). Other marginally behaved channels are logged, but not suppressed, since suppression would result in an unrecoverable loss of acceptance for high-p_T objects measured in the calorimeter.

Calorimeter noise and "hot" channels are not a serious concern for the energy measurement of electrons and photons. However, they do affect the measurement of jets and missing energy (i.e. neutrinos), as well as low energy particle detection. The effect of noise on the jet energy response will be addressed in the next chapter. The effect of noise on low energy particle detection efficiency and misidentification will be discussed in Chapter 6.

3.2.3 Massless Gaps and Inner Cryostat Detectors

The DØ calorimeters do not have uniform geometric acceptance or response in the region between the central and end-cap cryostats due to a gap in calorimeter coverage between them. In this region, which roughly spans $0.8 \lesssim |\eta_d| \lesssim 1.4$, the EM and FH sections are only partially instrumented, as shown in Fig. 3-4. The resulting energy response and acceptance in this region is not uniform due to this partial coverage.

In order to supplement this partial coverage, two types of detectors were instrumented in this region as shown in Fig. 3-7. The inner cryostat detector (ICD) consists of scintillator on the outer endcap calorimeter wall between the cryostats. The massless gap (MG) detectors consist of read-out cells in which the uranium is replaced by a G-10 board with resistive coating. The massless gaps are situated just inside both the CC and EC cryostat walls and measure charge in the same

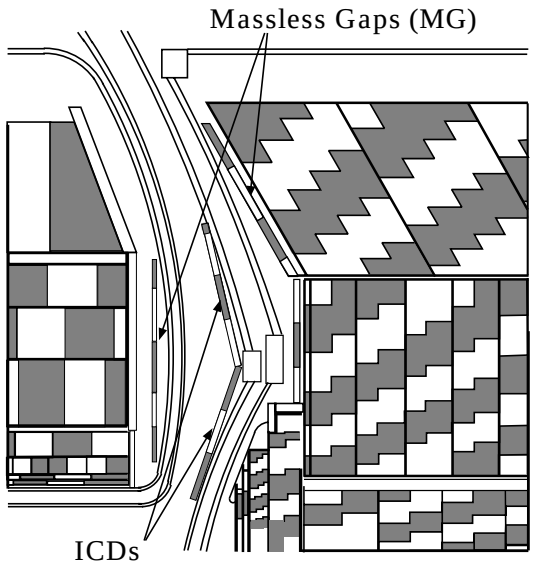

Figure 3-7: Cross sectional view of the DØ calorimeter showing the ICD and MG detectors.

way as the calorimeter.

Like the calorimeter, the ICD and MG have been calibrated in the DØ test beam. Online, the signals from both detectors are treated in the same way as the calorimeter in terms of calibration and zero-suppression. The pedestal noise widths for the ICD and MG detectors are shown in Table 3-1. The detectors can contribute a large fraction of reconstructed energy, particularly for jets entering this region, although the response and resolution is different from the calorimeter.

3.2.4 DØGEANT Detector Simulator

A detector simulator program, called DØGEANT [43] was developed, first, to aid in the initial design of DØ and, second, to assess the detector's performance with respect to physics analyses. DØGEANT simulates the detector behavior by incorporating the relevant electromagnetic and nuclear interaction processes. Specifically, multiple coulomb scattering, showering of electromagnetic and hadronic particles,

decays, and bremsstrahlung by electrons and muons are simulated. The *plate* version of the simulator incorporates the geometry of each passive absorber plate in order to obtain the most accurate calorimeter simulation. In the *mixture* version, however, certain geometric approximations (i.e. homogeneous mixture of absorber and ionizing material) are made to allow faster execution times resulting in larger simulated data samples. The response of the plate and mixture simulations have been shown to be similar and reasonably consistent with test beam data [37, 44].

3.2.5 The Trigger System

The DØ trigger system consists of three distinct levels. Each successive level uses a more restrictive requirement to reject events that do not meet the desired conditions. In this way the large rate of inelastic collisions ($\approx$ 500 kHz at a typical luminosity of $2 \times 10^{30}\text{cm}^{-2}\text{sec}^{-1}$) can be quickly reduced to a manageable data recording rate of a few events per second.

The three trigger levels relevant to this analysis are:

- **Level 0:** The level 0 trigger [45] is used to ensure the presence of an inelastic collision. Scintillator hodoscopes, located on opposite sides of the interaction point, are used to determine the presence of an inelastic collision by requiring a coincidence of hodoscope "hits" (on both sides) with the proton-antiproton bunch crossing. In addition, the timing difference between the two hodoscopes can be used to determine the position of the interaction along the beam direction (z-axis) as well as to determine if there is more than one inelastic collision per beam crossing.

  The level 0 can also be used to veto events (i.e. override other triggers and not read out the event) in which the main ring accelerator is active, since protons in the main ring can "scrape" or collide with the main ring beam

pipe passing through the calorimeter and deposit large amounts of energy in the coarse hadronic section.

- **Level 1:** The level 1 hardware jet trigger [46] sums all calorimeter layers in towers of 0.2×0.2 in η-ϕ and determines if the trigger tower transverse energy (E_T) is above a specified threshold. The minimum number of trigger towers above an E_T threshold and minimum $|\eta|$ of the towers can be specified at this level. For the 1992-1993 collider run, the level 1 trigger was implemented out to $|\eta| = 3.2$.

- **Level 2:** The level 2 software jet filter invokes a jet cone algorithm with $R = \sqrt{\Delta\eta^2 + \Delta\phi^2} = 0.7$ to find jets. The algorithm uses a list of level 1 trigger towers with $E_T > 3$ GeV as the center of the jets and sums all E_T in a 0.7 cone centered on these towers. Like the level 1 trigger, the minimum number of jets above an E_T threshold and minimum $|\eta|$ of the jets can be specified. In addition, the pseudorapidity separation ($\Delta\eta = |\eta_1 - \eta_2|$) between the jet axes can be specified in the filter to select specific jet pseudorapidity configurations.

Chapter 4

Jet Reconstruction

Jet measurement at DØ is done entirely with the calorimeter. The spray of particles contained in a jet deposits a concentrated "cluster" of energy in the calorimeter. The energy and location (η, ϕ) of the the cluster is determined by an iterative jet cone algorithm [47], given the primary vertex position. After the offline reconstruction, the transverse energy of all jets is corrected for the nonlinear response of the calorimeter. In addition, a series of cuts is imposed to significantly reduce spurious or "fake" jets arising from detector effects (such as hot cells).

4.1 Vertex Position Measurement

In order to reconstruct jets accurately, the vertex position must first be determined, since the measured value of E_T and η directly depend on the vertex position. The central detector tracking system (CDC or FDC) was used to determine the event vertex of the primary (high-p_T) interaction.

The vertex finding algorithm [48] determines the primary vertex position by extrapolating each track of the CDC back to the beam axis. In order to remove tracks that originate from other sources (such as scattering), a cut on impact parameter (distance from the z-axis in the xy-plane) of less than 2.5 cm is used. The point of closest approach to the nominal beam axis (z-axis) is used to de-

termine the z-position of each track along the axis. The z-positions of all tracks with $|z| < 100\,\mathrm{cm}$ are then histogrammed in 2 cm bins to determine "clusters" of track positions along the z-axis. The primary vertex position is then determined as follows:

- The bin containing the largest number of tracks (≥ 2) and its neighboring contiguous bins with at least one track are grouped together to form the primary cluster. The mean z-position of this cluster is determined as primary vertex position. The error in the vertex position is also determined.

- If no bin has more than two tracks, then the largest contiguous set of bins is used to determine the primary vertex.

- If there is only one track in the event, the vertex position is given by the z-position of that track and the error is the error determined from the reconstructed track.

If none of these conditions is satisfied, then no vertex is found. In addition, secondary and tertiary vertex positions and errors are reconstructed from the next largest clusters on each side of the primary vertex position. The primary vertex position resolution of the CDC vertex finding algorithm is less than 1 cm [49] for typical high-p_T events.

If no primary vertex is found using the CDC, the FDC is used to determine the vertex position. The FDC vertex finding algorithm, which is simpler than the CDC algorithm due to difficulties with the geometry, uses an iterative method to find the mean of all tracks with an impact parameter less than 3 cm. The algorithm determines the primary vertex iteratively from tracks with $|z| < 100\,\mathrm{cm}$ as follows:

- Determine the mean z-position and width from the tracks.

- Accept only tracks within 1.5 times the width of the mean and redetermine

the mean and width and iterate until the width does not change by more than 0.1 cm.

- Next, accept only tracks within 1.3 times the width of the previous mean and redetermine the mean and width. Iterate until the width does not change by more than 0.1 cm.

- The primary vertex position is the mean z-position from the final iteration. The error is also determined from the width obtained from the final iteration.

- If the error in the vertex position is greater than 10 cm, no vertex is found.

The FDC algorithm reconstructs only the primary vertex position and does not attempt to find multiple vertices due to the decreased vertex resolution of the FDC, which averages approximately 2 cm [49].

If no vertex is found using reconstructed tracks, the vertex position can be obtained from the timing difference between the two level 0 hodoscopes. The vertex resolution is approximately 4 cm for events with one interaction per beam crossing [45]. For events with multiple interactions the accuracy of the level 0 vertex becomes questionable.

4.2 The Cone Algorithm

The cone jet reconstruction algorithm [47] uses several steps to determine the location (η, ϕ) and E_T of jet candidates.

- **Seed Towers:** The first step in jet reconstruction involves finding calorimeter towers with $E_T > 1\,\mathrm{GeV}$. The towers are constructed by summing the energy vectorially (using the geometric center of each cell and the reconstructed vertex position) in all layers at each calorimeter (η, ϕ) position. Using the reconstructed vertex position each tower's E_T and η is determined.

- **Preclusters:** The seed towers are used to find jet "preclusters" of neighboring towers. If any seed tower is next to another in (η, ϕ), the E_T, η and ϕ of each neighboring tower is used to determine the E_T-weighted (η, ϕ) center of the precluster. Isolated towers that do not neighbor others are also considered as preclusters.

- **Jet cone algorithm:** Each precluster is used as a starting point for the jet cone algorithm. The (η, ϕ) position of each precluster serves as the initial cone center (η_0, ϕ_0) of the jets. For each cone, E_{total}, E_x, E_y, and E_z are summed for towers within a "cone" radius of $R = \sqrt{(\eta - \eta_0)^2 + (\phi - \phi_0)^2} = 0.7$. The (η, ϕ) centroid of the jet is then determined from

$$\begin{aligned} E_T &= \sqrt{E_x^2 + E_y^2}. \\ \theta &= \tan^{-1} \frac{E_T}{E_z} \\ \eta &= -\ln \tan(\theta/2) \\ \phi &= \tan^{-1} \frac{E_x}{E_y} \end{aligned}$$

  If the resulting centroid is very close to the center of the cone (η_0, ϕ_0), the jet position is stable and the algorithm is completed. If, however, the recalculated centroid changes, the algorithm uses this new centroid as the cone center and continues until the center of the cone corresponds to the centroid of the jet energy cluster. As a final step, only stable jets with $E_T > 8\,\mathrm{GeV}$ are retained.

- **Jet Splitting and Merging:** In some cases, several jet cones will overlap so that a portion of the energy in each cone is contained in another cone. Jets are merged or split depending on the E_T contained in the overlap region. If the shared E_T is more than 50% of the jet with the smaller E_T, the jets are merged into one by summing all towers in both jet cones and recalculating

the new (η, ϕ) centroid and E_T. Conversely, if the shared E_T fraction is less than 50%, the jets are split by awarding towers in the overlap region to the nearest cone center in (η, ϕ) and recalculating the each new centroid and E_T. Reconstructed jets that are within 0.01 in (η, ϕ) and within 10 MeV in E_T are considered to be the same jet and only one is retained.

4.3 Cone Algorithm Performance

The performance of the jet cone reconstruction algorithm has been evaluated using a Monte Carlo simulation [50]. The efficiency of the jet reconstruction as a function of jet E_T has been determined using the Monte Carlo event generator ISAJET [51] by generating two-jet events. The Monte Carlo simulation, which included leading-log parton showering and independent fragmentation, was adequate to determine the efficiency of the reconstruction algorithm.

Each generated jet event from ISAJET contained a list of particle types and momenta which were subsequently input into the DØ detector simulator DØGEANT (§3.2.4). By comparing the reconstructed events from the DØGEANT detector simulation to the jets at the particle level, the efficiency of the reconstruction was determined as a function of actual particle-level jet E_T. The resulting efficiency for jets with $E_T > 16\,\mathrm{GeV}$ was found to be 95% and the efficiency for jets with $E_T > 20\,\mathrm{GeV}$ was greater than 99%.

The position resolution of the reconstruction was also determined using the Monte Carlo simulation. For jets with $E_T = 30\,\mathrm{GeV}$, the η and ϕ resolutions were approximately 0.07 and 0.04 respectively. These resolutions are smaller than the transverse segmentation of the calorimeter of $\Delta\eta \times \Delta\phi = 0.1 \times 0.1$. The larger η resolution may arise from the measured (reconstructed) z-vertex resolution which was also simulated.

The jet reconstruction algorithm can also introduce systematic shifts in the

measured (η, ϕ) position with respect to the actual position. These shifts have been determined to be less than ± 0.02 in ϕ and less than ± 0.06 in η. At very large $|\eta|$ (> 2.6), the shift in η approaches 0.1 due to the geometry of the detector and calorimeter showering effects.

Another Monte Carlo study has been done [52] using HERWIG [53], which is believed to have more realistic jet shapes. The resulting η resolution and η shift obtained from HERWIG are approximately half as large as those from ISAJET. For all η, the systematic shift and resolution were determined to be less than 0.02 and 0.03 respectively, for jets with $E_T = 30\,\mathrm{GeV}$ [52]. For jets with larger E_T, the η bias is smaller.

4.4 Removal of Spurious Jets

The jet triggers and subsequent jet reconstruction algorithm can misidentify spurious energy not associated with the hard inelastic collision as real jets. These spurious or "fake" jets can arise from noisy calorimeter channels depositing false energy, main ring energy deposits not vetoed by the level 0 trigger, cosmic ray depositions, or other effects.

Several cuts can be made on reconstructed jets to greatly reduce the number of spurious jets. Since spurious jets generally have a very different longitudinal energy deposition compared to real jets, most of the cuts are made on the longitudinal distribution of energy in the jets. The cuts are outlined below:

- **The Electromagnetic Fraction Cut:** The electromagnetic fraction (EMF) is defined as the fraction of the reconstructed jet E_T that is contained in the electromagnetic section of the calorimeter. The EMF is required to be greater than 0.05 and less than 0.95 for "good" jets. This cut rejects approximately 95% [54] of fake jets from noisy cells in the electromagnetic or hadronic

sections. In addition, the efficiency of this cut for jets with $E_T = 30\,\mathrm{GeV}$ is 99.9% [55] except in the region between the central and forward calorimeters, where the electromagnetic section is not fully instrumented.

- **The Coarse Hadronic Fraction Cut:** Since the main ring accelerator runs directly through the coarse hadronic (CH) section of the calorimeter, energy from protons colliding with the beam pipe can be observed in the calorimeter. For the most part this problem is reduced by vetoing events that coincide with a main ring proton injection (§3.2.5), but occasionally there can be energy depositions in the CH section that are not associated with real jets. These main ring "jets" are removed by a cut of 0.4 on the fraction of jet E_T in the CH section. This cut removes about 95% of these jets and about 99% of jets from noisy cells in the CH section [50]. This cut is about 99% efficient for 30 GeV transverse energy jets but dips to about 94% at $\eta \approx 1.3$ due to the higher probability of more energy deposited in the CH section from missing electromagnetic and fine hadronic layers in this region [50].

- **Hot Cell Fraction Cut:** The hot cell fraction (HCF) is the ratio of the second highest energy cell to the leading energy cell in the jet. A cut of HCF> 0.1 is very effective at removing jets that are caused by a "hot" cell (highly energetic noisy cell) or jets that are contaminated by such a cell. The HCF cut rejects 80% of fake jets from "hot" cells and retains 98% of real jets [54, 55].

- **Missing E_T Significance Cut:** The missing E_T ($\not\!\!E_T$) significance is the ratio of the missing transverse energy in the event to the highest E_T jet in the event. Since jet events are not expected to have a large total transverse momentum (i.e. $p_T = \sqrt{(p_x^{J_1} - p_x^{J_2})^2 + (p_y^{J_1} - p_y^{J_2})^2} \approx 0$) on the average, a

good indication of the presence of a fake jet is an event that has a large $\not\!\!E_T$. A cut of 0.7 is made on the $\not\!\!E_T$ significance to reject events with fake jets. This cut has an efficiency of about 99.5% [55] for events with a 30 GeV transverse energy jet. This cut is typically not applied, but does provide an additional method to remove spurious jets.

For events with 30 GeV transverse energy jets, the standard cuts (excluding the missing E_T significance cut) have a combined efficiency of about 97% [55]. This efficiency is not crucial to the rapidity gap fraction measurement. However, the rejection of "fake" jets is relevant for this analysis and these cuts remove about 95% of fake jets [54].

4.5 Jet Energy Scale Correction

Jets typically contain many particles (π's, photons, etc.), a large fraction of which are usually at low energies. Therefore, since the calorimeter has a non-linear response at particle energies below 10 GeV (see §3.2.2), the measured jet energy is not proportional to the actual jet energy. In addition, the response varies with pseudorapidity, especially in the poorly instrumented regions between cryostats. Consequently, the calorimeter jet response, or jet energy scale, must be corrected to reflect the true jet energy.

A jet is experimentally defined as all particles which fall inside a cone of $R = \sqrt{\Delta\eta_2 + \Delta\phi^2} = 0.7$ of the jet axis. The true jet energy E_{true} is therefore defined as the sum of the energy of all particles within the cone. The measured jet energy E_{cal} is defined as the total energy within the cone as measured in the calorimeter. The jet response R_{jet} is simply the ratio of the measured energy to the true energy. Thus, given R_{jet} as a function of measured jet energy, the jet energy measured in the calorimeter can be corrected on the average to the true jet energy.

The jet energy scale in the calorimeter was determined using a two step process [50, 56, 57]. First, the jet response in the central region ($|\eta| < 0.7$) was determined from a sample of direct photon candidates using the missing transverse energy projection fraction method (MPF) originally introduced by CDF [58]. Second, the central jet response was used to map out the energy scale in the forward region ($|\eta| > 0.7$) by using events with one central jet balancing one forward "probe" jet.

The central jet energy scale calibration utilized a sample of events with a direct photon candidate and a jet, both with $|\eta| < 0.7$. Each jet was required to satisfy the good jet requirements in order to remove spurious or fake jets. The photon candidates were defined as a narrow isolated cluster ($R = \sqrt{\Delta\eta_2 + \Delta\phi^2} \lesssim 0.2$) of energy contained in the electromagnetic section of the calorimeter, with less than 5% of the total energy in the hadronic section. Due to this "loose" requirement, the photon sample contained both direct photons and neutral pions ($\pi^0 \rightarrow \gamma\gamma$) which were well contained in the electromagnetic section. The energy of the direct photon candidates could be measured with much better precision than the jets due to the linear response and good energy resolution of the electromagnetic section (see §3.2.2). The energy of the jets was then determined using the MPF method as given below.

The MPF is defined as the ratio of missing transverse energy $\not{E}_T$ in the direction opposite the photon candidate divided by the photon transverse energy E_T^γ:

$$\mathrm{MPF} \quad = \quad -\frac{\vec{\not{E}}_T \cdot \hat{n}_T^\gamma}{E_T^\gamma}.$$

This quantity thus reflects the amount of transverse energy which is "missing" from the measurement of the jet E_T in the calorimeter. The jet response is therefore

$$R(E_j') \quad = \quad 1 - \mathrm{MPF}$$

where $E'_j = E^\gamma \cosh \eta_j$ is the characteristic E_T jet scale of the event (i.e. estimate of the original parton E_T).

The MPF method assumes that all of the missing transverse energy in the direction opposite the photon is due to a mismeasurement of the jet transverse energy. However, if another jet or another cluster (a low E_T unreconstructed jet) is present in the event, the method will be biased. To minimize the bias, no additional jets above a threshold (depending on the photon E_T) are allowed. In addition, only events with a back-to-back topology in ϕ are used to minimize effects of another unreconstructed cluster.

The MPF method is insensitive to certain effects dependent on jet cone size that can increase or decrease the jet energy that is measured in the calorimeter. These effects are due to the underlying event, calorimeter noise, and out-of-cone energy deposition. The underlying event (spectator interactions) adds approximately 1 GeV to a jet's transverse energy on the average, while calorimeter noise and zero suppression (described in §3.2.2) tend to increase the measured energy in a 0.7 cone by about 2 GeV. In addition, about 4% of the energy of particles in the jet is deposited out of the 0.7 cone due to calorimeter shower spreading. Each of these effects is accounted for before the jet energy is corrected according to the MPF method.

The jet response determined from the MPF method for $|\eta| < 0.7$ is shown in Fig. 4-1 as a function of jet energy. The response is approximately 83% for jets with $E_T = 20$ GeV and approaches 90% for 100 GeV jets. Only statistical error is shown.

Once the jet response in the central region was determined, the response in the forward region ($|\eta| > 0.7$) was mapped out using two-jet events with one central jet and one forward "probe" jet. A simple E_T balance method was used (as opposed to MPF) since it automatically corrects for the underlying event, calorimeter noise,

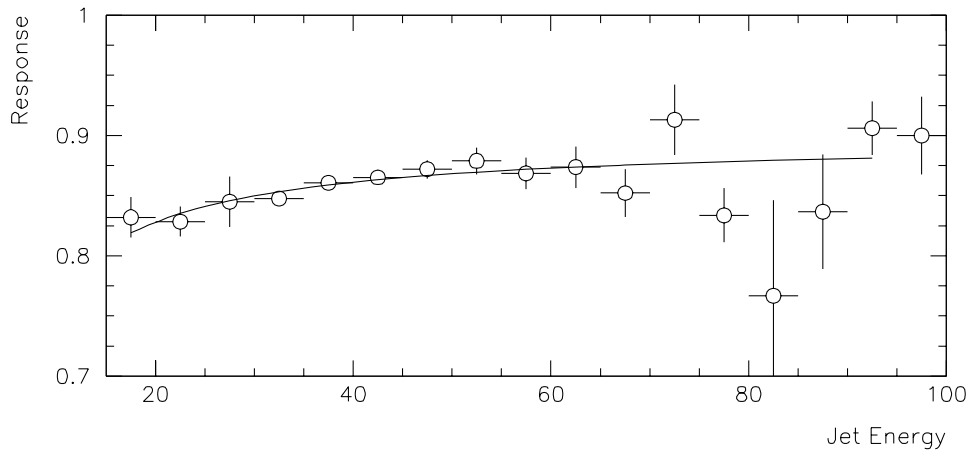

Figure 4-1: The calorimeter jet response R_{jet} in the central region versus jet energy. A fit to the response is shown as the solid curve. The error bars denote statistical errors only.

and out-of-cone showering in the the forward region. While the underlying event and calorimeter noise are on the same order as in the central region, out-of-cone showering can reduce the jet energy in a cone by as much as 15% due to the transverse shower broadening in the calorimeter. In the forward region a 0.7 cone in η-ϕ is physically much smaller than a 0.7 cone in the central region. Particles which are inside the cone can deposit a significant portion of their energy outside of the cone since the typical calorimeter shower of a single particle shower becomes comparable to the physical size of the jet cone.

The final jet energy scale correction ($1/R_{jet}$) versus jet transverse energy is shown in Fig. 4-2 for two values of pseudorapidity ($|\eta|$=0 and 2.5). For low energy jets the correction varies significantly but approaches 17% for high transverse energy jets.

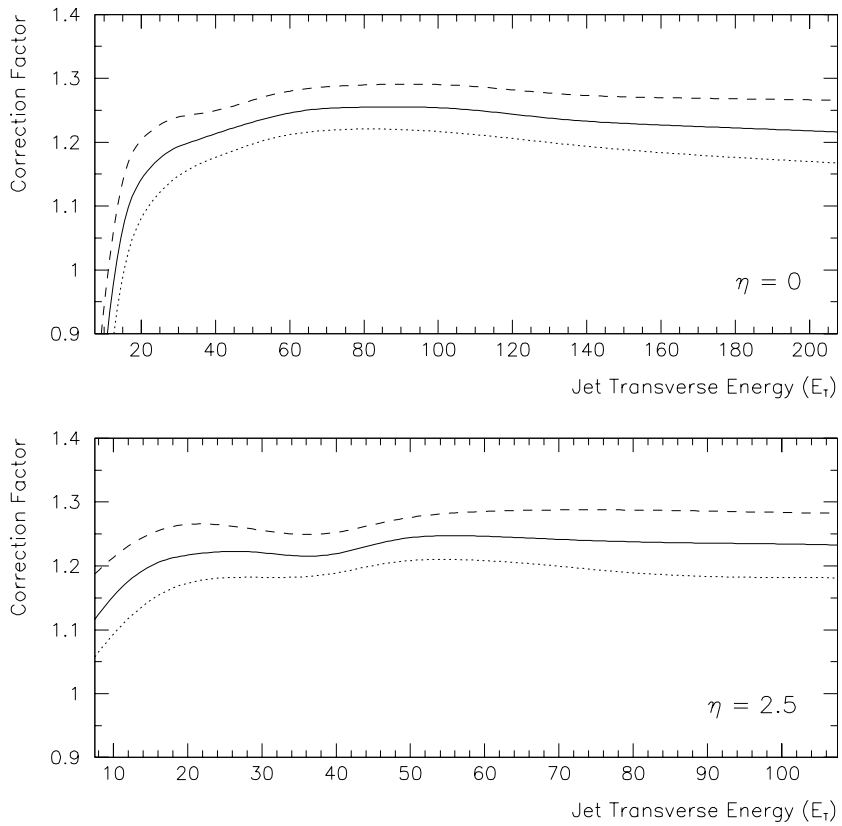

Figure 4-2: The jet energy scale correction for $|\eta|$=0 and $|\eta|$=2.5 versus measured jet transverse energy. The nominal correction is denoted by the solid line and the upper and lower errors (systematic and statistical) are denoted by the dashed and dotted lines respectively.

4.6 Jet Energy Resolution

The jet response in the calorimeter determined in the previous section is a measure of the average response of jets. According to Fig. 4-1 a jet with 30 GeV at the particle level deposits 85% of its energy in the calorimeter on the average. However, due to the intrinsic energy resolution of different particles in the calorimeter (see §3.2.2), jets have a significant smearing of measured energy. The jet resolution varies significantly with (detector) pseudorapidity due to the shower size and detector instrumentation in different regions.

Although the jet energy scale correction is essentially free from resolution biases [59], correcting the energy of jets which follow a falling distribution (i.e. a typical jet cross section) can introduce a resolution bias in the corrected sample. Each jet can be corrected properly on the average, but the energy (or transverse energy) distribution of jets will not have the correct shape due to resolution effects. Therefore, to correct for the energy scale of jets properly, an additional correction must be applied to account for the resolution bias, especially if a cross section (shape) is being measured.

The jet energy resolution versus jet energy is shown in Fig. 4-3 for the three calorimeter regions [50]. The central region has the best resolution while the poorly instrumented inner cryostat region (crack) has the lowest resolution. The forward region is worse than the central region primarily because of large out-of-cone effects.

Each region is fit to the functional form

$$\left(\frac{\sigma_E}{E}\right)^2 = \left(\frac{S}{\sqrt{E}}\right)^2 + \left(\frac{N}{E}\right)^2 + (C)^2 \tag{4.1}$$

where S denotes the calorimeter "sampling" fractional resolution, N represents the fractional resolution from noise, and C represents a constant contribution. The sampling term usually is the largest component of the resolution in sampling calorimeters like DØ. The values of the fractional sampling constant for the central

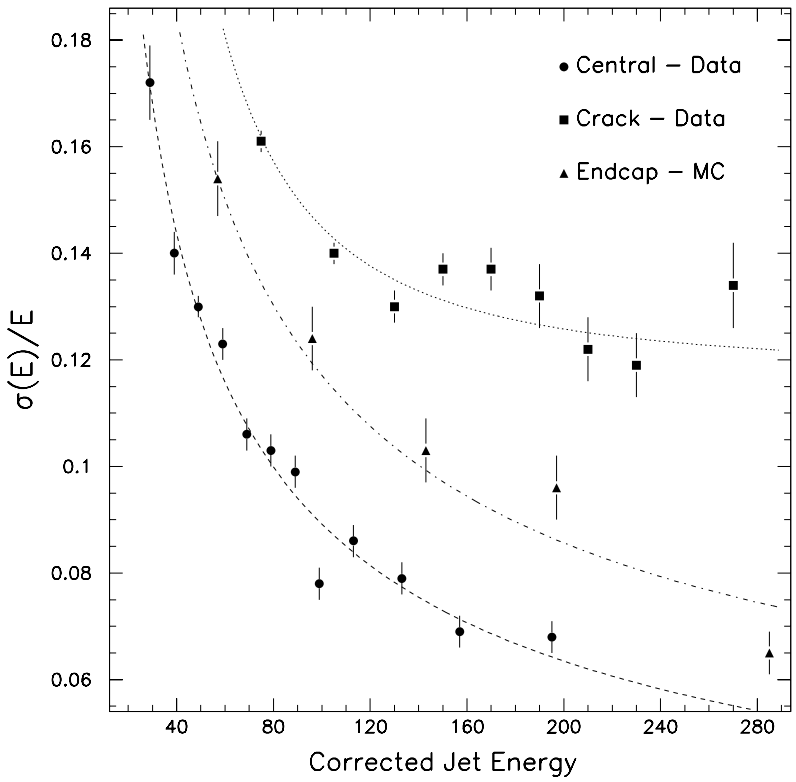

Figure 4-3: The jet energy resolution versus energy for the central (circles), inner cryostat (squares), and forward (triangles) calorimeter regions. Fits to Eq. 4.1 for the three regions are also shown.

and endcap regions are 86% and 110% respectively. The inner cryostat region, due to its poor calorimeter instrumentation and mixed detector types, has a large noise term which dominates and results in relatively poor resolution compared to the other regions.

Chapter 5

Triggers and Data Selection

The data used in this analysis was taken during the 1992-1993 run at the Fermilab Tevatron Collider. The collider produced a total integrated luminosity of $31\,\mathrm{pb}^{-1}$, $17\,\mathrm{pb}^{-1}$ of which was recorded to tape. The collider operated at instantaneous luminosities ranging from $0.5 \times 10^{30}\mathrm{cm}^{-2}\mathrm{sec}^{-1}$ to $8.7 \times 10^{30}\mathrm{cm}^{-2}\mathrm{sec}^{-1}$ with an average luminosity of about $3.0 \times 10^{30}\mathrm{cm}^{-2}\mathrm{sec}^{-1}$.

5.1 Jet Triggers

As mentioned in Chapter 3, the DØ trigger system consists of three separate trigger levels. Jet triggering at DØ is accomplished by adjusting the requirements at each level to study the jet physics of interest. A standard set of single jet triggers, which covered a large range of E_T and η, was implemented for the 1992-1993 run. These triggers were primarily intended for measuring the inclusive jet cross section. In addition, a dijet trigger was also implemented to increase statistics for jets with large pseudorapidity separations (large $\Delta\eta = |\eta_1 - \eta_2|$).

5.2 Description of Triggers

Two triggers were used to sufficiently cover the large range of jet pseudorapidity separations needed for this analysis: an inclusive jet trigger primarily for small values of $\Delta\eta$, and a high-$\Delta\eta$ trigger implemented in order to increase the statistics for large values of $\Delta\eta$. The triggers had similar jet E_T requirements and differed primarily in their pseudorapidity requirements on the jets.

The requirements for the inclusive and high-$\Delta\eta$ triggers at each of the three trigger levels are as follows:

- **Level 0:** Both jet triggers required the presence of an inelastic collision. In addition, both triggers vetoed events in which the main ring accelerator was active in order to reduce anomalous energy deposition in the calorimeter. The inclusive trigger additionally required a level 0 vertex of $|z| < 10.5\,\mathrm{cm}$. This requirement reduced the trigger rate by about a factor of four, allowing a lower prescale (see below) and better jet E_T measurement. The high-$\Delta\eta$ trigger did not have a level 0 vertex requirement due to its relatively small cross section.

- **Level 1:** The inclusive trigger required one trigger tower above 7 GeV at any η while the high-$\Delta\eta$ trigger required two towers above 5 GeV each with $|\eta| > 2$. Note that the requirement on the high-$\Delta\eta$ trigger did not necessarily restrict the towers to be at opposite η or in separate jets since the trigger could also be satisfied by one jet with $|\eta| \gtrsim 2$ or two jets on the same side with $|\eta| \gtrsim 2$.

- **Level 2:** The inclusive trigger required one jet with $E_T > 30\,\mathrm{GeV}$ at any η, while the high-$\Delta\eta$ trigger required two jets each with $E_T > 25\,\mathrm{GeV}$ and $|\eta| > 2$. In addition, the high-$\Delta\eta_c$ trigger required a jet separation of $\Delta\eta = |\eta_1 - \eta_2| > 4$ for any two jets satisfying the E_T and η requirements. The

more restrictive pseudorapidity requirements on the high-$\Delta\eta$ trigger, allowed a larger portion of events with large values of $\Delta\eta$ to be recorded compared to the inclusive trigger.

Each trigger required different trigger "prescales" depending on the instantaneous luminosity in order to keep the triggering rate within the allotted data recording rate bandwidth. This was due to the large difference in triggering rate between the two triggers as a result of their different pseudorapidity requirements. The less restrictive inclusive trigger required a significant prescale factor at all instantaneous luminosities: at low luminosities ($1.0 \times 10^{30}\,\mathrm{cm}^{-2}\mathrm{sec}^{-1}$) the prescale was set to reduce the trigger rate by a factor of 20, and at high luminosities ($8.0 \times 10^{30}\,\mathrm{cm}^{-2}\mathrm{sec}^{-1}$) the prescale was set to 5000. In contrast, the high-$\Delta\eta$ trigger, due to its more restrictive requirements and relatively small trigger rate, was not prescaled until the instantaneous luminosity reached $3.0 \times 10^{30}\,\mathrm{cm}^{-2}\mathrm{sec}^{-1}$; at a luminosity of $8.0 \times 10^{30}\,\mathrm{cm}^{-2}\mathrm{sec}^{-1}$ the prescale was set to 20. At higher luminosities the prescales were set to turn-off all jet triggers, since lower luminosities were sufficient to obtain adequate statistics within the fixed bandwidth. This allowed triggers for rarer processes, such as $p\bar{p} \to t\bar{t}$, to remain unprescaled at all luminosities in order to obtain large integrated luminosity samples.

5.3 Trigger Sample

The trigger sample contains 500,000 events ($120\,\mathrm{nb}^{-1}$) from the inclusive trigger and 77,000 events ($5.4\,\mathrm{pb}^{-1}$) from the high-$\Delta\eta$ trigger. In order to understand the differences and similarities of the two triggers, it is useful to compare certain distributions. The distributions discussed in the sections below show the trigger sample *after* reconstruction, with the requirement that each event has at least two jets with $E_T > 8\,\mathrm{GeV}$. Although the distributions differ from those at the trigger

level due to the differences between the trigger and the offline reconstruction, they serve to illustrate the effect of the trigger requirements on the offline analysis. The differences between the inclusive and high-$\Delta\eta$ triggers and their effect on the rapidity gap fraction measurement will be further discussed in Chapter 7.

Jet E_T Distribution

Although the jet E_T trigger thresholds for the inclusive and high-$\Delta\eta$ triggers are similar (30 GeV versus 25 GeV, respectively), the two-jet requirement of the high-$\Delta\eta$ trigger produces drastically different jet E_T distributions than the inclusive trigger.

For the inclusive trigger, the jet with the highest E_T (or the leading jet) in each event determines if the event is accepted by the trigger. Ideally, only events containing leading jets with E_T >25 GeV should be accepted. However, due to level 1 inefficiencies, level 2 jet energy resolution (compared to the offline reconstruction), and the offline energy scale correction, the threshold becomes less well defined, and a significant portion of jets can appear below the effective energy scale corrected trigger threshold. This is apparent in Fig. 5-1(a) as a smeared "turn-on" as opposed to a sharp cut-off at the threshold. In contrast, the second highest E_T jet is not significantly affected by the trigger requirements (although the jets are correlated), and the jet E_T distribution is not restricted to be greater than a certain threshold. This effect can be seen in as a rather long tail extending down to low jet E_T.

The high-$\Delta\eta$ trigger has a drastically different behavior due to its more restrictive two-jet requirement, as shown in Fig. 5-1(b). The E_T distribution of the second leading jet has no significant low E_T tail as in the inclusive trigger because the second leading jet in each event determines if the event is accepted by the trigger. As a result, the high-$\Delta\eta$ trigger contains a smaller fraction of multijet

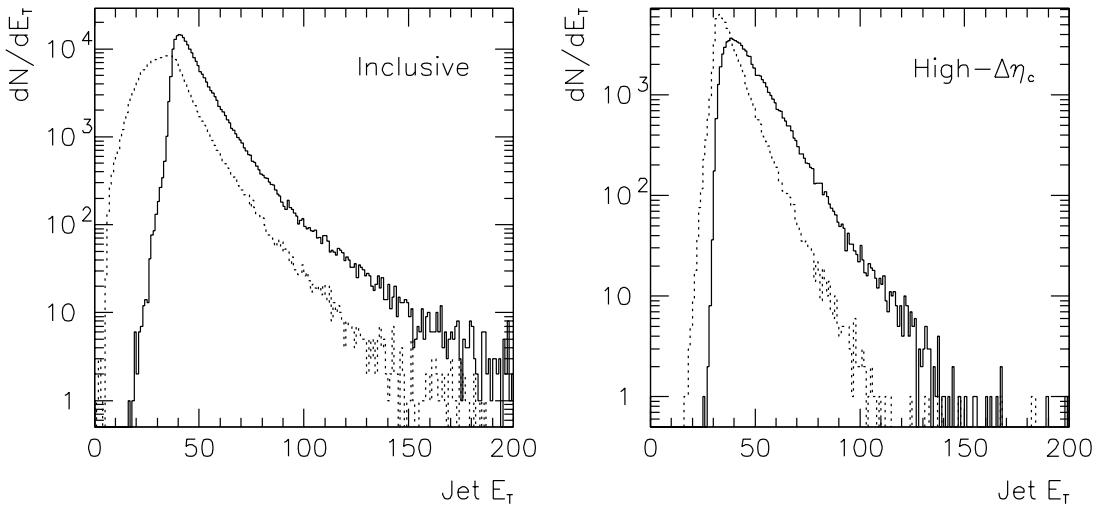

Figure 5-1: The E_T distributions of the two leading (highest E_T) jets for the inclusive trigger (a) high-$\Delta\eta$ trigger (b). The leading jet distribution is shown as a solid line and the second leading jet distribution is denoted by the dotted line.

events (more than two jets) compared to the inclusive trigger.

Jet η Distribution

The jet pseudorapidity distributions also have different behavior for the two triggers due to their different trigger requirements on the jets. Further, the level 1 trigger, which was instrumented only out to $|\eta| = 3.2$, affects the jet acceptance of each trigger differently.

The inclusive trigger had no explicit pseudorapidity requirement at the trigger level. However, since it required one level 1 trigger tower, there is an implicit cut-off of $|\eta| \lesssim 3.2$ for the leading jet (see Fig. 5-2(a)). This cut-off is not sharp since a jet with $|\eta| > 3.2$ still could have been accepted by the level 1 trigger as long as it had at least one tower with $|\eta| \leq 3.2$ and E_T above the threshold. In contrast, the second leading jet in each event was typically not limited by the trigger coverage and its pseudorapidity extends well beyond $|\eta| = 3.2$.

Several anomalous "bumps" are apparent on the η distributions. The bumps

at $|\eta| \approx 1.3$ are due to the innercryostat and massless gap detectors which reside between the central and forward calorimeters. These detectors have a relatively poor energy resolution (§4.6) which artificially enhances these regions with jets that fluctuate above the trigger E_T threshold; at higher jet E_T this effect is reduced. The additional "bumps" are due to noisy calorimeter cells that have been erroneously reconstructed as jets (§4.4). The η-ϕ scatter plot in Fig. 5-2(b) clearly shows the "hot spots" caused by specific calorimeter cells (i.e. at specific η-ϕ positions). These are subsequently removed in the offline analysis (§5.4.2).

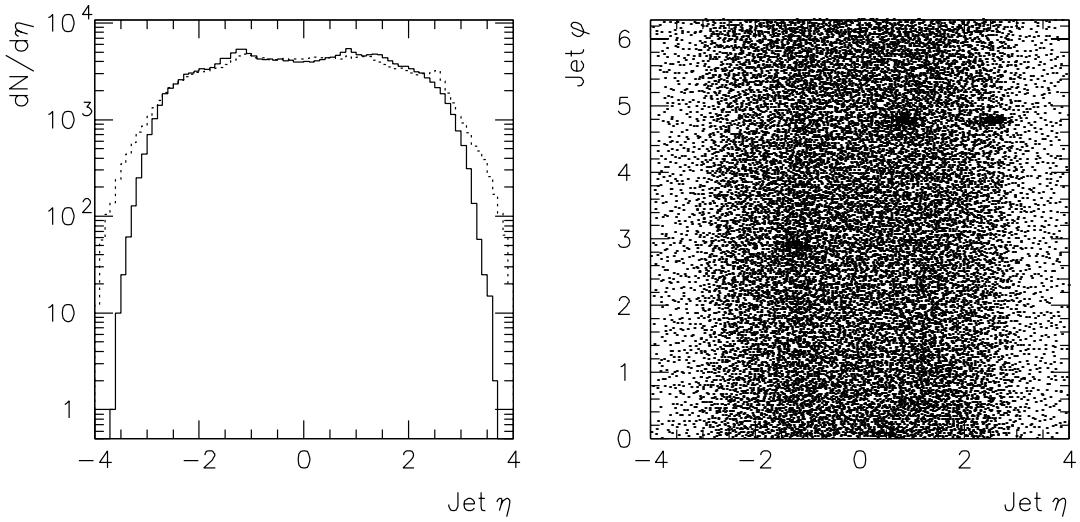

Figure 5-2: The η distributions (a) and η-ϕ scatter plot (b) for the two leading (highest E_T) jets for the inclusive trigger. The leading jet distribution is shown as a solid line and the second leading jet distribution is denoted by the dotted line.

In contrast to the inclusive trigger, the high-$\Delta\eta$ trigger has very similar η distributions for both the leading and second leading jets since they are both subject to the same trigger conditions, as shown in Fig. 5-3(a). Also evident is the jet trigger requirement of $|\eta| > 2$, which significantly enhances the statistics for large $\Delta\eta$ compared to the inclusive trigger. Jets with $|\eta| < 2$ are a result of the trigger accepting events with an additional central jet that has been reconstructed as one of the two leading jets. Events in which either of the two leading jets have

$|\eta| < 2$ are subsequently removed in the offline analysis (§5.4.4).

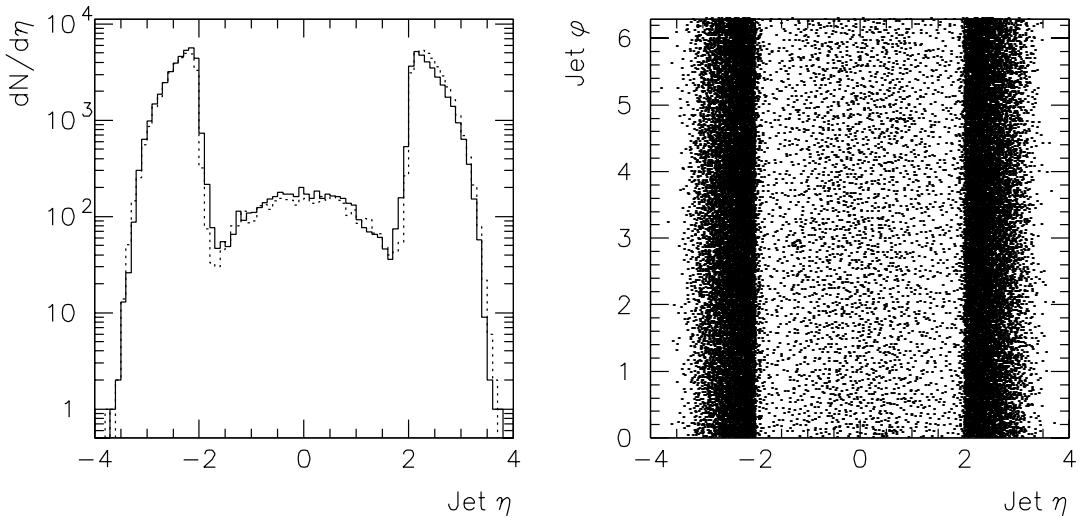

Figure 5-3: The η distributions (a) and η-ϕ scatter plot (b) for the two leading (highest E_T) jets for the high-$\Delta\eta$ trigger. The leading jet distribution is shown as a solid line and the second leading jet distribution is denoted by the dotted line.

$\Delta\eta_c$ Distribution

The high-$\Delta\eta$ trigger was implemented to increase the statistics for large jet pseudorapidity separations compared to the inclusive trigger. The pseudorapidity separation between the edges of the jet cones is given by $\Delta\eta_c = \Delta\eta - 2R = |\eta_1 - \eta_2| - 2R$, where $R = 0.7$ is the jet cone radius used in the jet finding cone algorithm (§4.2). The $\Delta\eta_c$ distribution for the two triggers is shown in Fig. 5-4, for events with $\Delta\eta_c > 0$. The figure shows the enhancement of statistics for large $\Delta\eta_c$ from the high-$\Delta\eta$ trigger. This enhancement arises primarily from the lower prescale on the high-$\Delta\eta$ trigger, which allowed a larger fraction of events with large $\Delta\eta_c$ data to be recorded.

The $|\eta| > 2$ requirement of the high-$\Delta\eta_c$ trigger results in an implicit requirement of $\Delta\eta_c > 2.6$, and this threshold is clearly apparent in Fig. 5-4. However,

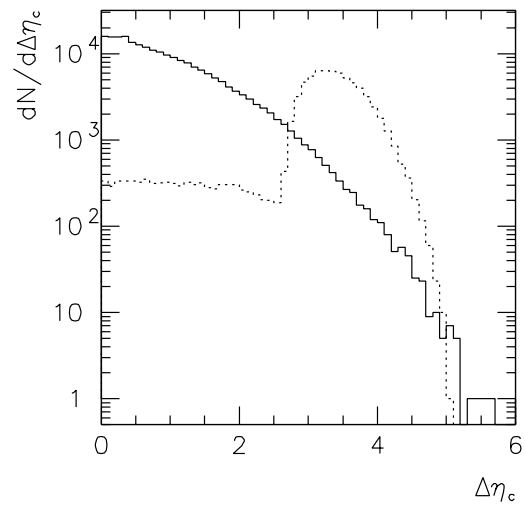

Figure 5-4: The $\Delta\eta_c$ distributions for the inclusive and high-$\Delta\eta_c$ triggers. The solid line represents the inclusive trigger, and the dotted line denotes the high-$\Delta\eta$ trigger.

the threshold is not very sharp since the $|\eta| > 2$ requirement excludes events certain η_{boost} values (see §5.3.2 for more on this bias). In addition, smearing between the trigger and the offline reconstruction (in η) results in a less sharp threshold, although this effect is small compared to the η_{boost} effect. Events with $\Delta\eta_c < 2.6$ result from central nontriggering jets being reconstructed as one of the two leading jets. The high-$\Delta\eta$ trigger is biased at very large $\Delta\eta_c$ due to the limited level 1 trigger tower η coverage (see above section), which accepts events with $\Delta\eta_c \lesssim 5$. The differences in the $\Delta\eta_c$ distribution between the two triggers and their effect on the rapidity gap fraction measurement will be discussed in Chapter 7.

5.3.1 Dijet Trigger Efficiencies

This analysis requires events with at least two jets in order to define $\Delta\eta_c$ for the gap fraction measurement. The E_T of the second leading jet determines if the event is included in the sample since both leading jets are required to be above the same E_T threshold. The dijet trigger efficiency—the efficiency for accepting

an event—has been determined from the E_T distribution of the second leading jet.

The dijet trigger efficiency was estimated by fitting the jet E_T distribution to a suitable function in a region where the triggers are expected to be fully efficient. By taking the ratio of the fit to the actual distribution, the efficiency can be extrapolated to small E_T. Although the accuracy of the extrapolation diminishes away from the fitted E_T region, it is sufficient for illustrating the efficiency for each trigger as a function of jet E_T.

The jet E_T distributions from both triggers are fit to the functional form

$$\frac{a}{x^b} + ce^{-dx} \tag{5.1}$$

which fits both distributions well ($\chi^2/\text{dof} < 1$) for jet $E_T > 45\,\text{GeV}$ where the triggers are essentially fully efficient. The fits and extrapolations for each trigger are shown in Fig. 5-5.

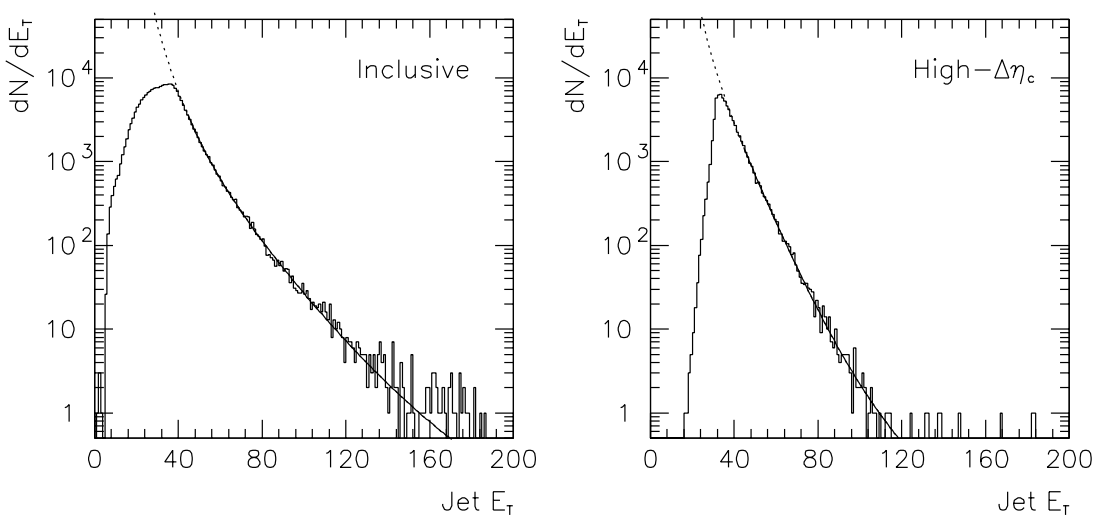

Figure 5-5: Fits to the jet E_T distributions of the inclusive trigger (a) and high-$\Delta\eta$ trigger (b). Equation 5.1 is fit to both distributions for $E_T > 45\,\text{GeV}$, where both triggers are assumed to be fully efficient. The extrapolated fits are used to determine the approximate efficiency of each trigger.

The resulting approximate trigger "efficiencies" are shown in Fig. 5-6. Although

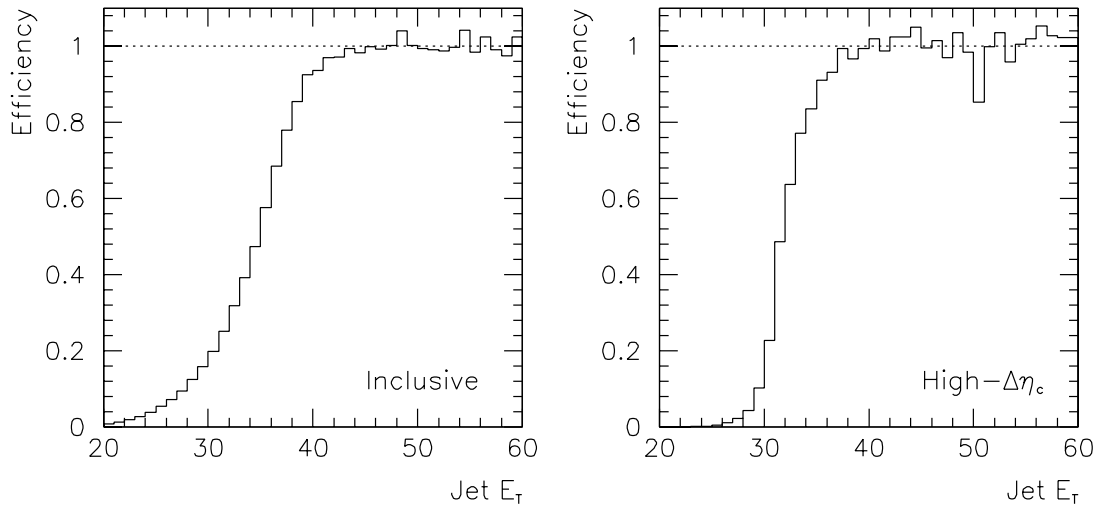

Figure 5-6: Approximate efficiencies for the inclusive trigger (a) and high-$\Delta\eta$ trigger (b) obtained from extrapolated fits to Eq. 5.1.

both triggers are "efficient" ($\geq 95\%$) for 40 GeV jets, the high-$\Delta\eta$ trigger "turns-on" faster and is efficient down to 35 GeV. For jets with $E_T > 30$ GeV the inclusive trigger is only 70% efficient while the high-$\Delta\eta$ trigger is 85% efficient.

5.3.2 Trigger Biases

The requirements of the triggers, although essential for obtaining the sample of events for this analysis, can systematically bias the physics being studied. The origins of the known trigger biases are discussed in the sections below. Their effect on the rapidity gap fraction measurement will be addressed later in Chapter 7 and Appendix A.

Level 1 Trigger Bias

The triggers used in this analysis can be subject to biases from the level 1 trigger requirements imposed on the jets. The level 1 trigger system utilizes small trigger towers (0.2×0.2 in η-ϕ) above an E_T threshold as part of the jet triggers. However,

due to the small size of the trigger towers compared to the transverse jet size, the level 1 trigger is sensitive to the fragmentation of jets. Narrow, collimated jets are more likely to satisfy the level 1 requirements than wide jets with the same total transverse energy. Thus, the level 1 trigger can have a systematic bias due to jet fragmentation, and quark jets, which are more likely to fragment "harder" [60] (fewer particles and higher p_T), are more likely to satisfy the level 1 trigger than gluon jets with the same E_T [61].

To investigate this possible bias, the Monte Carlo event generator JETSET [62] was used to generate central ($\eta \approx 0$) qq and gg dijet events. This Monte Carlo simulator incorporates parton showering and angular ordering along with string fragmentation to produce the final state particles and jets. The events were then input into the DØGEANT detector simulator and the relative efficiencies for qq and gg dijet events for various level 1 tower thresholds were determined as a function of parton p_T.

Figure 5-7 shows the bias ($\epsilon_{qq}/\epsilon_{gg}$) obtained from the inclusive jet level 1 requirement (one tower above 7 GeV) for qq dijet events with respect to gg dijet events as a function of parton p_T. Also shown are the values of p_T where qq and gg dijet events become 95% efficient. The bias necessarily becomes small when the trigger is efficient for both types of dijet events, and for fully efficient triggers the bias is negligible. A full description of the level 1 trigger bias study is given in Ref. [61].

Although the study demonstrates a bias due to the level 1 trigger requirements, its actual effect is difficult to determine due to inherent uncertainties in the Monte Carlo event generator and subsequent detector simulation. Further, the study was done only for central jets. Therefore, the actual magnitude of the bias for the triggers used in this analysis is unknown. The possible effect of a quark bias on the rapidity gap fraction measurement is discussed in Appendix A.

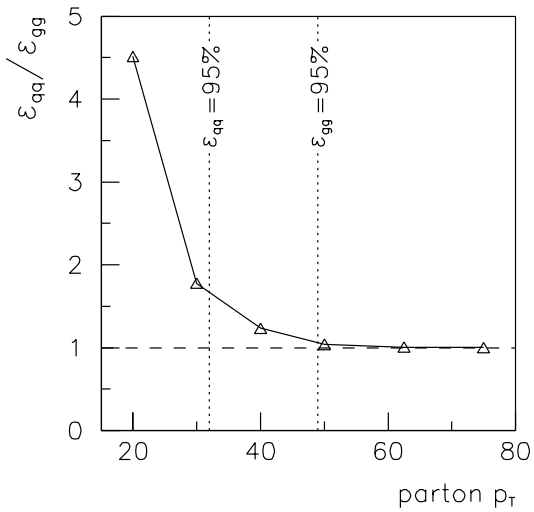

Figure 5-7: The ratio $\epsilon_{qq}/\epsilon_{gg}$ showing the bias towards qq dijet events with respect to gg dijet events as a function of parton p_T. The dotted lines show the p_T at which qq and gg dijet events are 95% efficient.

Bias in the High-$\Delta\eta$ Trigger

The high-$\Delta\eta$ trigger has an additional bias, apparent in Fig. 5-4, due to the requirements on the jet pseudorapidities: near the $\Delta\eta_c = 2.6$ threshold the trigger has an acceptance loss and therefore does not "turn-on" fully until higher $\Delta\eta_c$. The requirement of $|\eta| > 2$ on the jets results in acceptance only for events with $\eta_{boost} = \frac{1}{2}(\eta_1 - \eta_2)$ near zero for $\Delta\eta_c \sim 2.6$. The η_{boost} distribution for $\Delta\eta_c > 2.6$ is shown in Fig. 5-8 for both the inclusive trigger and the high-$\Delta\eta$ trigger . The η_{boost} distribution from high-$\Delta\eta$ trigger is clearly biased toward small values due to the pseudorapidity requirements imposed on the jets and only allows events with a maximum η_{boost} of

$$|\eta_{boost}^{max}| \quad = \quad \tfrac{1}{2}(\max(|\eta_1|, |\eta_2|) - 2) = \tfrac{1}{2}(\Delta\eta_c - 2.6).$$

Thus for $\Delta\eta_c \approx 2.6$, only small boosts are allowed, while for larger $\Delta\eta_c$ the boost distribution becomes less biased.

The high-$\Delta\eta$ trigger also has a bias caused by the E_T requirement on the

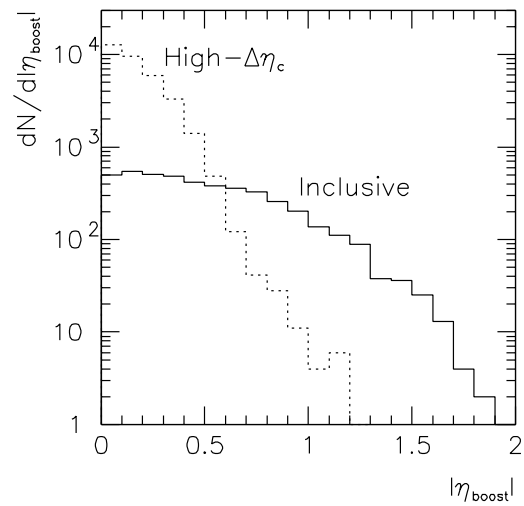

Figure 5-8: The $|\eta_{boost}|$ distribution for $\Delta\eta_c > 2.6$ for the inclusive trigger (solid line) and high-$\Delta\eta$ trigger (dotted line).

second jet (see Fig. 5-1). The trigger does not accept certain multijet events—for example, an event containing three jets with $E_T = 30$, 20, and 10 GeV—whereas the inclusive trigger would accept these events.

The high-$\Delta\eta$ trigger has a small additional acceptance bias due to the limited level 1 trigger coverage of $|\eta| < 3.2$. This constraint leads to a lack of acceptance for very large $\Delta\eta_c$ (~ 5) as evident in Fig. 5-4 compared to the inclusive trigger. However, since only a small fraction of jets have $|\eta| \gtrsim 3.2$, this bias is small.

5.4 Event Selection

Offline cuts are made on each trigger sample to yield a relatively unbiased event sample for the rapidity gap fraction measurement. It is important that the cuts do not preferentially select or exclude rapidity gap events since this would directly bias the measured fraction. Clearly the samples from both triggers are not purely inclusive (as mentioned in above sections), and the gap fraction measurement can be indirectly affected. Therefore in calculating the gap fraction these effects are

either corrected for or treated as a systematic error.

5.4.1 Removal of Bad Data Runs

A small portion of the data taken by the two triggers had systematic problems related to the detector or collider. Suspect data runs were logged as questionable at the time and subsequently removed from the data sample. In addition, a portion of the data was reconstructed without part of the information used to find spurious jets; these runs were also removed from the data sample. Duplicate data runs or events that occurred due to bookkeeping problems during reconstruction have also been removed.

5.4.2 Removal of Events with Spurious Jets

In this analysis, any event with one or more spurious jets is removed from the sample, since spurious jets could severely bias the measurement. The standard cuts, described in detail in §4.4, are used to flag spurious or "fake" jets. These cuts remove approximately 15% of the events, and less than 1% of the events in the final sample are estimated to contain a spurious jet.

5.4.3 Rejection of Multiple Interactions

Due to the relatively large instantaneous luminosities of the Fermilab Tevatron, it is possible that more than one inelastic collision can occur in a proton-antiproton bunch crossing. At the Tevatron, the average number of minimum bias interactions per beam crossing is given by $\bar{N}_{mb} = 0.15\mathcal{L}$, where $\mathcal{L}$ is the instantaneous luminosity in units of $10^{30}\mathrm{cm}^{-2}\mathrm{sec}^{-1}$. In addition, the number of interactions per crossing is Poisson distributed leading to an exponential probability for single interactions of $P(single) = \mathrm{e}^{-0.15\mathcal{L}}$, and a probability for multiple interactions of

$P(multiple) = 1 - e^{-0.15\mathcal{L}}$. Events with multiple interactions contain a source of particles not associated with the triggering interaction.

The level 0 scintillator hodoscope counters are used to flag and reject these events [45, 63]. Each hodoscope measures the time distribution of particles (or hits) passing through its scintillator (§3.2.5). The deviation of the time distribution in each counter is calculated and combined in quadrature to give an overall width for each event. Events containing only one inelastic collision generally have a narrower width than events with several interactions since additional interactions significantly increase the width in each counter. Therefore, an appropriate cut on the width can be used to produce a relatively pure sample of events with single interactions.

The behavior of this cut as a function of instantaneous luminosity is shown in Fig. 5-9 (a) and compared to the expected probability for a single interaction and for multiple interactions. The cut follows the single interaction expectation and therefore rejects a large portion of the events with additional interactions. The efficiency for tagging events with only one interaction is shown in (b) and indicates that the cut is only 75% efficient for typical luminosities. In addition, less than 5% of events satisfying this cut are expected to contain multiple interactions [63].

5.4.4 Final Cuts and Data Sample

In order to make the gap fraction measurement as a function of $\Delta\eta_c$, each event is required to have at least two jets with $E_T > 30\,\text{GeV}$, since both triggers are reasonably efficient for jets with $E_T > 30\,\text{GeV}$ (70% and 85% for the inclusive and high-$\Delta\eta$ triggers respectively; see §5.3.1). The two leading (highest) jets in each event with $E_T > 30\,\text{GeV}$ are subsequently used to determine $\Delta\eta_c$. Events with $\Delta\eta_c < 0$ are removed since the cones of the two leading jets overlap in pseudorapidity. In addition, the two leading jets of the high-$\Delta\eta$ trigger each are

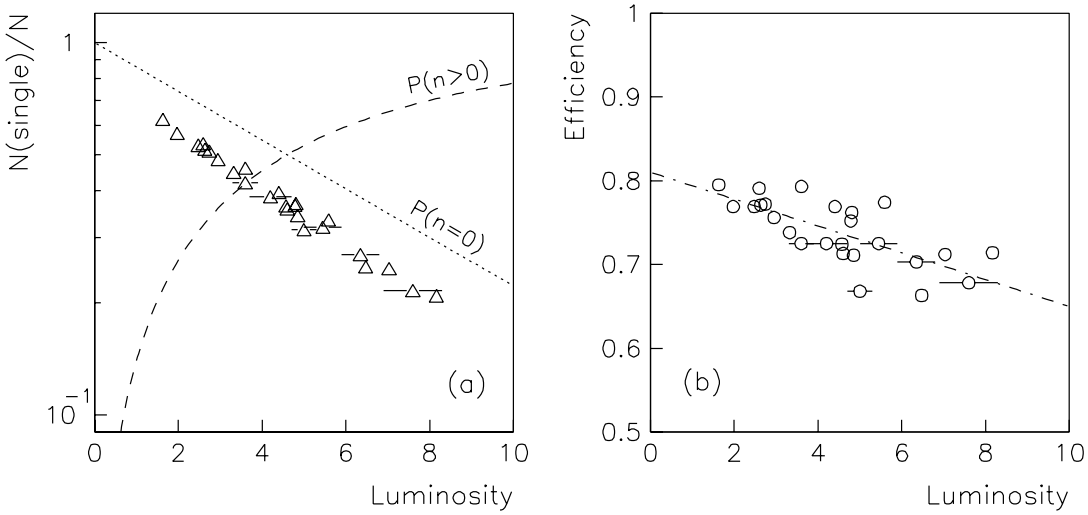

Figure 5-9: Behavior of the level 0 single-interaction cut versus instantaneous luminosity. Figure (a) shows the fraction of events which satisfy the cut as a function of instantaneous luminosity (in $10^{30}\mathrm{cm}^{-2}\mathrm{sec}^{-1}$) compared to that expected for single interactions (solid line) and for multiple interactions (dotted line). Figure (b) shows the efficiency for flagging single interactions versus luminosity.

required to have $|\eta| > 2.0$, which implicitly imposes a requirement of $\Delta\eta_c > 2.6$.

Additional fiducial cuts are made on both trigger samples to assure that the events are well measured by the detector. Events are required to have a measured vertex within 50 cm of the average vertex position. This ensures that the event is contained well within the fiducial volume of the detector. The z-vertex distribution for both triggers is shown in Fig. 5-10 (a). The inclusive trigger has the expected narrower width than the high-$\Delta\eta$ trigger due to the level 0 z-vertex requirement. The region between the arrows corresponds to the accepted values of the z-vertex position.

In addition, events are required to have $|\eta_{boost}| = |\eta_1 + \eta_2| < 0.8$ in order to ensure that the rapidity interval between the jets has a large overlap with the central calorimeter. This maximizes the particle tagging efficiency, which is best in the central calorimeter (§2.7.4). The $|\eta_{boost}|$ distribution for both triggers is

shown in Fig. 5-10 (b). The inclusive trigger has a much wider distribution than the high-$\Delta\eta$ trigger due to its less restrictive pseudorapidity requirements. The offline cut is shown by the arrow. The high-$\Delta\eta$ trigger is not affected.

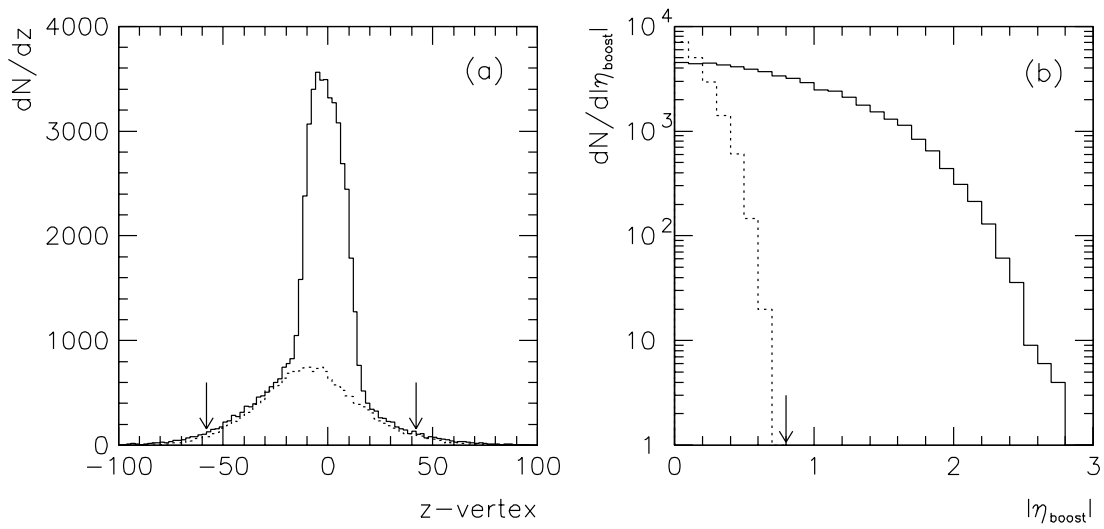

Figure 5-10: The z-vertex and $|\eta_{boost}|$ distributions for the inclusive trigger (solid line) and high-$\Delta\eta$ trigger (dotted line). For the vertex distribution the region between the vertical lines denotes the accepted values of the z-vertex. For the $|\eta_{boost}|$ distribution, only events with values to the right of the arrow are accepted.

The data from the two triggers are combined into one data sample by using the inclusive trigger for events with $\Delta\eta_c < 2.7$ and the high-$\Delta\eta$ trigger for events with $\Delta\eta_c \geq 2.7$. The final data sample contains 30,612 events with $\Delta\eta_c < 2.7$ from the inclusive trigger and 18,029 events with $\Delta\eta_c \geq 2.7$ from the high-$\Delta\eta$ trigger. The $\Delta\eta_c$ distribution for the combined data sample is plotted in Fig. 5-11 and shows a clear enhancement in statistics for $\Delta\eta_c \geq 2.7$ (see also Table 5-1). This inclusive dijet sample is subsequently used to search for rapidity gap events (Chapter 6), to determine the experimental rapidity gap fraction (Chapter 7), and to place an upper limit on the fraction of events with no particles between the jets (Chapter 8).

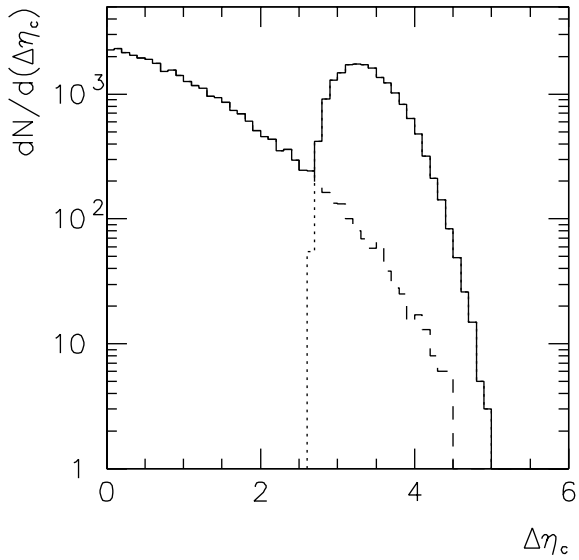

Figure 5-11: The $\Delta\eta_c$ distribution for the final combined data sample (solid line). The dashed and dotted lines correspond to the $\Delta\eta_c$ distributions for the inclusive and high-$\Delta\eta$ triggers respectively.

$\Delta\eta_c$	Inclusive	High-$\Delta\eta$
$0.0 - 2.7$	30612	60
> 2.7	1194	18029

Table 5-1: The statistics of the final data sample from the inclusive and high-$\Delta\eta_c$ triggers for $0 < \Delta\eta_c < 2.7$ and $\Delta\eta_c > 2.7$.

Chapter 6

Experimental Rapidity Gap Definition and Sample

Observation of a true rapidity gap signal, that is jet events with no particles between the jets, would be simple with an ideal detector. Since an ideal detector would perfectly measure both the presence and absence of particles, it would perfectly identify events containing a rapidity gap, if such events existed.

In contrast, any real detector has intrinsic particle detection inefficiencies and noise which can obscure the observation of rapidity gaps. Noise can introduce spurious "particles" that contaminate a rapidity gap, and events containing a rapidity gap can be lost due to these artificial "particles" spoiling the gap. Conversely, particle detection inefficiencies can result in some real particles not being detected. Thus a region of rapidity containing particles that are not detected would be misidentified as a rapidity gap.

Clearly, in order to search unambiguously for rapidity gap events, perfect particle detection is necessary. Since no real detector can achieve this, identification of rapidity gaps on an event-by-event basis is not possible. Inefficiencies result in an indeterminate background contribution which cannot be distinguished from the signal at the event level (see §2.10.1). In addition, noise results in an artificial loss of rapidity gap events. Thus, the rapidity gap signal must be measured by

statistical methods, incorporating all known physics and detector effects that can contribute a background or cause the loss of rapidity gap events. Since many aspects of rapidity gap "production" and "survival" in hard scattering interactions are not understood (§2.9), determining the existence of a rapidity gap signal is difficult experimentally.

An upper limit can be placed on the signal, however, by measuring an *experimental* rapidity gap "signal". Since an experimental measurement includes the true signal plus background contributions from inefficiencies (§2.10.1), it can be used to place a conservative upper limit on the rapidity gap signal. The DØ detector is used for this purpose by defining an experimental rapidity gap as a region of pseudorapidity containing no *tagged* (observed) particles.

The DØ detector was designed for high-p_T physics, for which it has good high-p_T particle and jet identification. However, DØ is also suitable for low energy particle detection since there is no central magnetic field (which would allow measurement of particle charge and momentum) causing an effective transverse momentum cut-off for low energy charged particles. This allows detection of charged particles down to the intrinsic limits of the tracking detector. In addition, the calorimeter is also useful for low energy particle detection due to its fine longitudinal and transverse segmentation. The calorimeter is sensitive to both neutral and charged hadrons as well as photons, muons and electrons. Thus the calorimeter offers an excellent complement to the tracking system for detection of low energy particles.

6.1 Tagging Particles with the Calorimeter

A special compressed data sample was used in this analysis. The data sample contains only the most important event information: reconstructed jet, electron, photon, muon, neutrino and tau information; the event vertex and multiple interaction information; and the jet triggering information and calorimeter tower

information. Due to its compact size, however, it does not contain all reconstructed particle tracking information since it retains tracks only associated with reconstructed electrons, muons and taus. In addition, the calorimeter tower information is stored in a zero suppressed format that contains only electromagnetic and hadronic towers above transverse energy thresholds of 200 MeV and 400 MeV respectively.

Since the tracking information is incomplete, the calorimeter tower information is used to find low energy particles in each event. The EM section of the calorimeter is particularly useful for identifying low energy particles due to its low level of noise and ability to detect both charged and neutral pions. In addition, the EM section is sensitive to minimum ionizing particles, which deposit about 200 MeV in an EM tower [64]. The hadronic section is only marginally useful for low energy particle detection due to its larger noise level and significantly smaller detection efficiency.

In this analysis, *a particle is tagged by the deposition of more than 200 MeV transverse energy in an EM calorimeter tower.* Although the EM section has many advantages over the hadronic section of the calorimeter, it is not fully instrumented at all pseudorapidities. The electromagnetic coverage versus η_d (detector η) is shown in §3.2.2, Fig. 3-6. In the region between the central and endcap calorimeters, the EM section is not fully instrumented for $1.1 < |\eta_d| < 1.4$.

In the region where the EM section is fully instrumented, this method for tagging particles has a geometric acceptance of about 95% due to ϕ cracks between intra-calorimeter modules which cause a loss of visible energy [65]. The overall geometric acceptance (including the uninstrumented region) for tagging particles varies between 80% and 95% depending on the size and location of the pseudorapidity interval between the two leading jets ($\Delta\eta_c$).

6.2 Tagging Efficiency

While the particle tagging definition is clearly not ideal because it only uses calorimeter tower information above a threshold, the resulting efficiency for detecting low energy particles is sufficient for imposing an interesting upper limit on the rapidity gap fraction. Clearly, any improvement in tagging efficiency (such as including full calorimeter and tracking information) would yield a lower, more restrictive upper limit, but the tagging method described above is sufficient.

It must be noted that knowledge of the tagging efficiency is not necessary for placing an upper limit on the rapidity gap fraction since no attempt is made to subtract the indeterminate background contribution resulting from detection inefficiencies. Thus the efficiency is provided as information to the reader to illustrate the relative response of the tagging definition to both charged and neutral particles as a function of particle energy.

6.2.1 Test Beam Efficiency

A calorimeter particle library was used to study the calorimeter response to particles of various energy [66]. This library contains the calorimeter cell energy information of test beam electrons and charged pions with incident energies ranging from 2 to 150 GeV. Zero suppression and pedestal subtraction was implemented to simulate actual online running of the DØ detector.

The particle library contains the benchmark test beam data which was centered at $\eta_d = 0.05$ and $\phi = 3.16$ of the test calorimeter cryostat. The particle test beam had a roughly flat distribution across the face of the test calorimeter that covered the benchmark calorimeter tower, parts of surrounding towers, and the cracks between these towers [67]. The library contains calorimeter cell information for a square window of towers centered on the nominal tower. For electrons this read-out

section consisted of 5×5 towers, while for pions the read-out was a larger 15×15 window of towers. All longitudinal (depth) calorimeter information is retained for pions, while for electrons only the electromagnetic layers and the first hadronic layer is stored.

The efficiency for tagging particles was determined by constructing EM towers from the particle library calorimeter information and imposing a cut of E_T >200 MeV on all towers. The resulting efficiency for tagging electrons and charged pions as a function of test beam particle energy is shown in Fig. 6-1. The efficiency for tagging 2 GeV electrons is about 97% while the efficiency for tagging 2 GeV charged pions is about 73%.

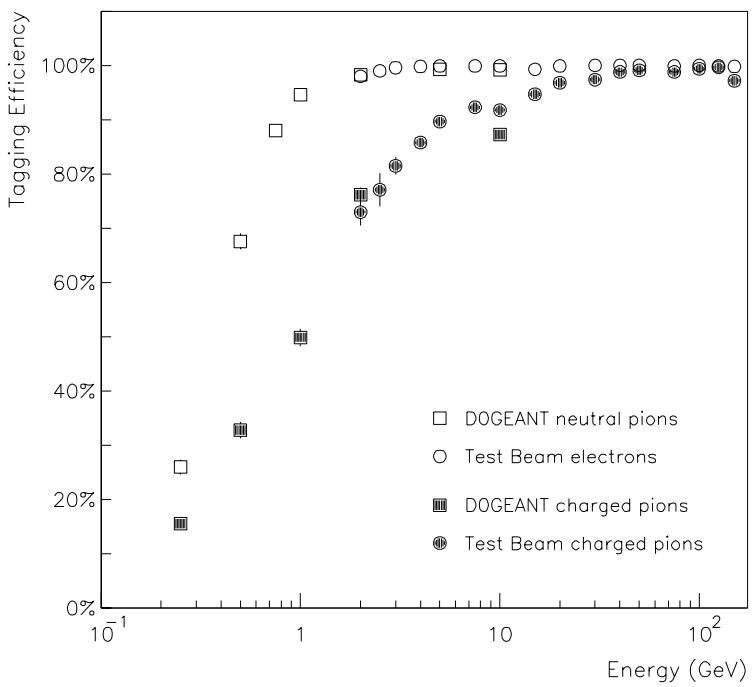

Figure 6-1: The efficiency of tagging electrons/neutral pions (open points) and charged pions (solid points) for energies ranging from 250 MeV to 150 GeV. The DØGEANT efficiencies are represented by squares, while the test beam efficiencies ($E > 2$ GeV) are denoted by circles.

6.2.2 DØGEANT Efficiency

The test beam particle library contains only a limited low energy sample (down to 2 GeV) at one location in the calorimeter. To determine the efficiency for tagging particles at lower energies and in other parts of the calorimeter, Monte Carlo simulations must be used. The DØ detector simulator program DØGEANT (§3.2.4) was used to simulate the detector response to low energy neutral and charged pions at $\eta_d \approx 0$. Figure 6-1 shows the efficiency obtained for particle energies of 0.25, 0.5, 0.75, 1.0, 2.0, 5.0 and 10.0 GeV. The DØGEANT efficiencies are reasonably consistent with those from the test beam in the region of overlap.

6.2.3 Particle Response in Minimum Bias Events

Minimum bias events (§2.7.4) provide a good means of assessing the relative response (or efficiency) for tagging low energy particles as a function of pseudorapidity in the detector. Minimum bias events have an approximately uniform average charged particle multiplicity distribution in η-ϕ space for $|\eta| \lesssim 3.0$ [23, 24] with an average p_T per particle of approximately 500 MeV[68]. Thus the minimum bias rapidity plateau can be used to determine the detector η dependence of the particle tagging efficiency.

For this study, a sample of events satisfying the minimum bias trigger (a coincidence in the level 0 hodoscopes—see §3.2.5) was used. For each event the detector η position of tagged particles was determined. The resulting distribution is plotted in Fig. 6-2.

Figure 6-2 clearly shows a flat response for $|\eta_d| < 1.0$ and the geometric acceptance loss between the central and forward calorimeters (see Fig. 3-6). In addition, the response in the forward calorimeters becomes drastically reduced at large $|\eta_d|$ compared to the central calorimeter. This is most likely due to two effects. In the forward region ($|\eta_d| > 1.3$), additional upstream material in front of the calorime-

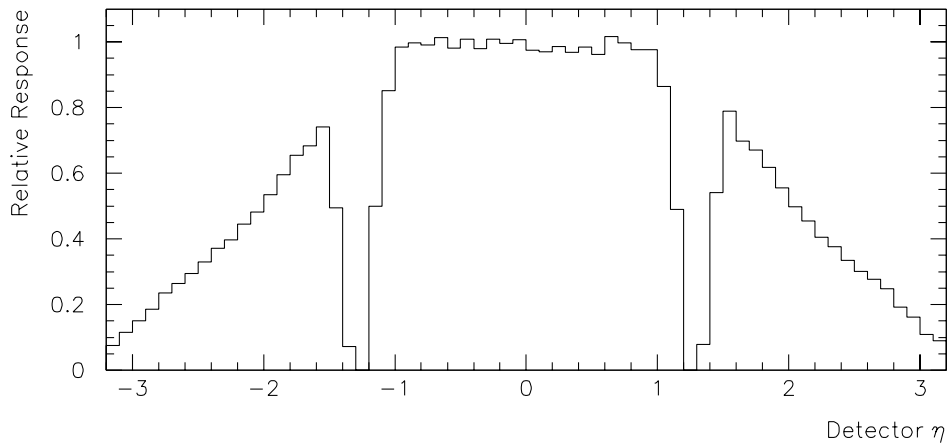

Figure 6-2: Distribution of tagged particles in minimum bias events versus detector η.

ter can cause the loss of energy, and the projective tower size becomes smaller relative the calorimeter shower size. These two effects combine to give a falling response to low energy particles with increasing $|\eta_d|$.

Tagged Particle Position

The efficiencies given above do not take into account the dispersion of the tagged particle position compared to the true particle position:

$$\sigma = \sqrt{(\eta_{true} - \eta_{tag})^2 + (\phi_{true} - \phi_{tag})^2}.$$

Low energy particles can be tagged at a position significantly away from the original particle position due to multiple scattering in the central detector and calorimeter shower broadening. Although the tagged particle position is affected in both η and ϕ, only the dispersion in η is a concern.

Multiple scattering in the central detector is not a large effect due to the particle tagging threshold in the calorimeter. The mean scattering angle from multiple

Coulomb scattering is given by [69]

$$\theta_0 \approx q\sqrt{\frac{x}{X_0}}\frac{13.6\,\mathrm{MeV}}{\beta \mathrm{cp}}$$

where p, βc, and q are the momentum, velocity and charge number of the incident particle respectively, and x/X_0 is the thickness of the scattering medium in radiation lengths [40]. The thickness of the beam pipe and central detector is approximately $\lesssim 0.3$ radiation lengths in front of the central calorimeter and $\lesssim 1.0$ in front of the endcap calorimeters. Therefore, for charged pions with $p_T > 200\,\mathrm{MeV}$ (the transverse energy threshold for tagging a particle in the calorimeter), the scattering angle is $\theta_0 \lesssim 2°$. Thus multiple scattering does not produce a large deviation in the tagged particle position.

The η dispersion in the calorimeter (due to scattering and shower broadening) has been determined from DØGEANT for neutral and charged pions at $\eta_d \approx 0$. Table 6-1 shows the resulting η dispersion (σ_η) and the η dispersion that contains at least 95% of all tagged particles ($\sigma_\eta^{95\%}$). The relatively large dispersion of the low energy neutral pions is mostly due to the angular separation in the decay $\pi^0 \to \gamma\gamma$ as opposed to calorimeter shower broadening. Although other short-lived resonances (such as η and ρ) are expected to produce larger dispersions in the calorimeter due to their decay to other particles, these resonances are produced (from hadronization) much less frequently than pions.

Although the study was done only for $\eta_d \approx 0$, the maximum dispersions in the forward calorimeter region can be estimated assuming that the characteristic calorimeter shower size (in θ) does not significantly increase in the forward region. Table 6-2 shows the estimated dispersions ($\sigma_\eta^{95\%}$) for $|\eta_d| = 2$, 2.5 and 3 for particles with $p_T \gtrsim 200\,\mathrm{MeV}$. However, these should be considered conservative (overestimates) due to the reduced efficiency for tagging particles in the forward region as shown in Fig. 6-2.

Particle Type	Energy	σ_η	$\sigma_\eta^{95\%}$
Neutral Pions (π^0)	250 MeV	0.20	0.6
	500 MeV	0.10	0.3
	1 GeV	0.08	0.2
	5 GeV	0.07	0.1
Charged Pions ($\pi^\pm$)	250 MeV	0.04	0.1
	500 MeV	0.06	0.1
	1 GeV	0.08	0.2
	5 GeV	0.10	0.3

Table 6-1: Dispersion in η of tagged particles in the calorimeter with respect to the actual position.

Particle Type	$\lvert\eta_d\rvert = 2$	$\lvert\eta_d\rvert = 2.5$	$\lvert\eta_d\rvert = 3$
Neutral Pions (π^0)	0.4	0.5	0.7
Charged Pions ($\pi^\pm$)	0.3	0.5	0.8

Table 6-2: Estimated maximum dispersion ($\sigma_\eta^{95\%}$) in η of tagged particles in the forward calorimeter region.

6.2.4 Response to Noise

Before utilizing the calorimeter to tag particles, it is necessary to understand how often noise generates spurious tagged "particles". Noise in the calorimeter can arise from the passive uranium material generating particles that ionize the active argon and produce a measurable amount of deposited energy. In addition, electronics noise can create false energy in calorimeter channels. Although zero-suppression is implemented to reduce these effects, on the average about 5% of the calorimeter cells fluctuate to give positive energy that is not suppressed. If the energy of one or more of these cells in an electromagnetic tower is greater than 200 MeV, noise will be erroneously tagged as a "particle".

To determine the probability that noise is misidentified as a particle, several "noise runs" were analyzed. These runs were taken using a random "zero-bias" trigger which sampled the detector randomly. A total of three zero bias runs were analyzed, two taken with no main-ring or Tevatron beam, and one with the collider

operating at high luminosity.

The no-beam zero-bias runs each contained about 1000 events with all of the calorimeter cell information recorded. Zero-suppression and pedestal subtraction were applied offline to simulate the online zero-suppression and pedestal subtraction. For each event the number of electromagnetic towers with transverse energy above 200 MeV was counted in the pseudorapidity region $|\eta_d| < 3.2$. The multiplicity of EM towers per event for each zero-bias run is shown in Fig. 6-3. The probability per event of noise being tagged as a particle can be determined by counting all events with one or more towers above the threshold. The resulting probabilities for the runs are $(0.2 \pm 0.1)\%$ and $(3.6 \pm 0.6)\%$ respectively.

The zero-bias run that was taken during colliding was analyzed separately. Although the zero-bias "trigger" was random, a large fraction of events could contain inelastic collisions due to proton-antiproton interactions. To eliminate these events, the level 0 scintillator hodoscopes were required to have no "hits" that would indicate the presence of an inelastic collision. The remaining (≈ 3500) events were then analyzed in the same way as the no-beam zero-bias runs. The multiplicity distribution of towers above threshold is shown in Fig. 6-4. The probability per event of noise being tagged as a particle for this run is $(2.6 \pm 0.3)\%$.

These zero bias runs contain limited statistics and cover a limited time span (each lasting a few hours or less). Although the actual contamination rate over the entire data taking run is not well known, it is assumed to be relatively stable. Therefore, in this analysis, the contamination rate of noise is conservatively taken to be $\leq 5\%$. This effect (random noise) should be distinguished from the effect of spurious "noisy" channels. Random noise affects each calorimeter cell in roughly the same way by producing a noise distribution with a certain pedestal (average) and width. In contrast, noisy channels are relatively isolated and behave much more erratically than normal cells. These cells are flagged and removed before

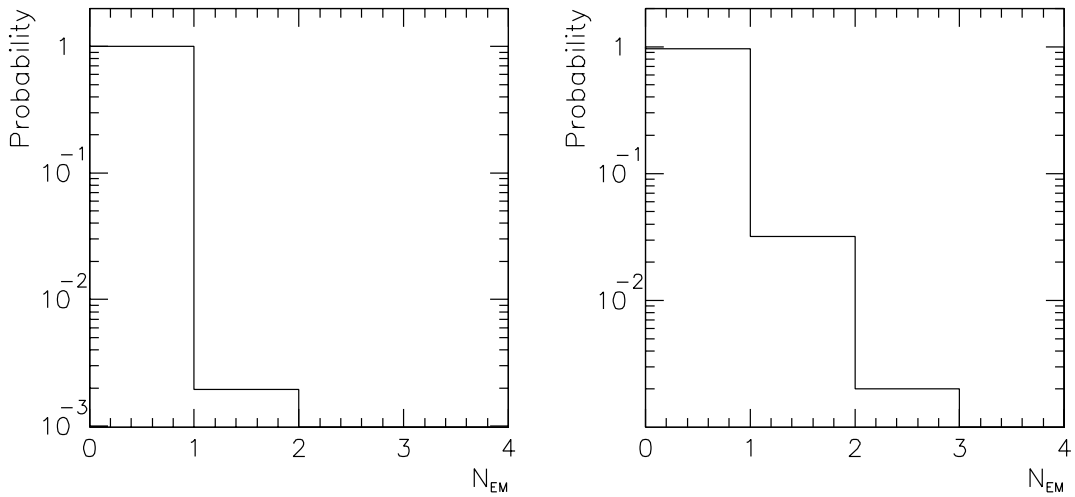

Figure 6-3: Tagged particle multiplicity of noise runs with no beam.

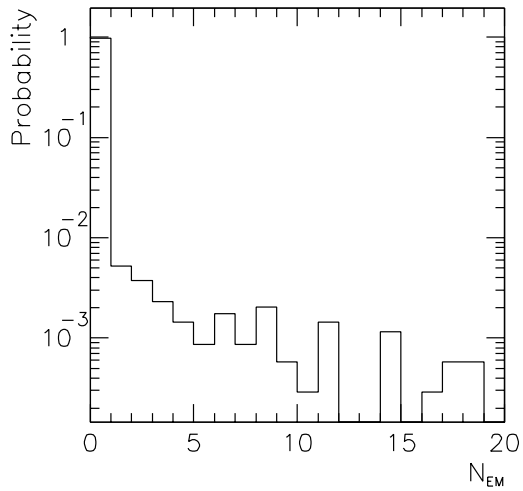

Figure 6-4: Tagged particle multiplicity of a noise run with beam.

searching for rapidity gaps (see next section).

6.3 Removal of Noisy Calorimeter Channels

The particle tagging definition is not immune to erratic, noisy channels. Although random noise is rarely misidentified as a particle in the calorimeter, pathologically noisy or "hot" channels are a concern since they can be misidentified much more often. To minimize the impact on the gap fraction measurement, electromagnetic towers that have been identified as noisy are ignored.

Noisy towers are identified by first determining the number of times each EM tower is above 200 MeV (called the tower occupancy) using a large data sample ($\sim 10^6$ events obtained from the jet standard triggers). The occupancy of each tower is then compared to the occupancy of its neighbors to determine if the tower is noisy. If the occupancy of a tower differs by more than 3σ from the mean occupancy of towers at the same detector η, the tower is considered "hot". In order to find "hot" towers that are relatively short lived, the data sample is split into various time intervals.

Figure 6-5 shows the EM tower occupancy obtained from the entire data sample. Hot channels are evident as spikes in the occupancy. While some channels are hot over a long period of time (months), other more intermittent hot towers could not be found using the entire data sample. Shorter lived pathological towers were found by splitting the sample into a range of smaller intervals in time. The smallest allowed time interval encompassed one physics run, which typically lasted four hours. On the average 10-20 towers per event were flagged as "hot", resulting in a geometric acceptance loss of less than 2%. After removal of identified noisy towers, less than 5% of events are estimated to contain an unidentified noisy tower as determined from varying the "hot" (number of σ) requirement.

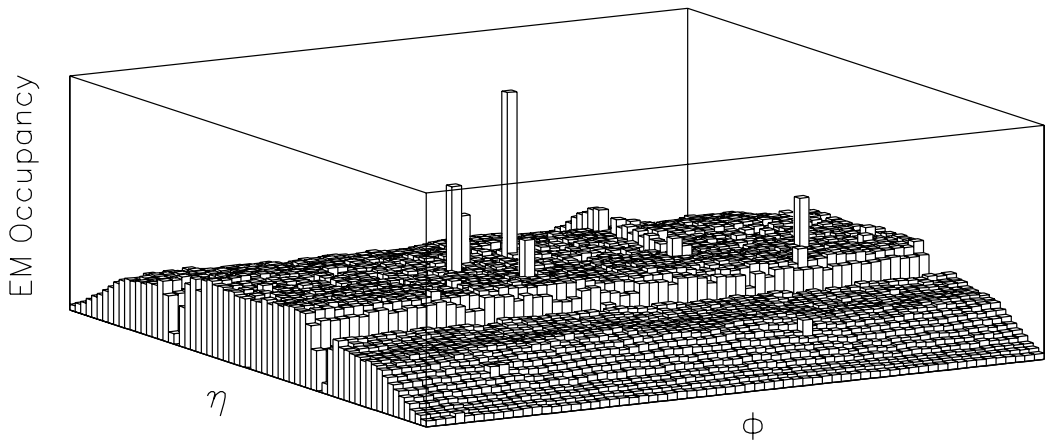

Figure 6-5: The EM calorimeter tower occupancy showing "hot" towers. The overall shape in η is due to the (jet) triggers used in the sample and the particle tagging efficiency of Fig. 6-2.

6.4 Experimental Rapidity Gap Sample

After noisy towers have been removed, a subsample of events that have no tagged particles between the two leading jets is obtained. This experimental rapidity gap sample is used to determine the experimental rapidity gap fraction as a function of $\Delta\eta_c$, the pseudorapidity interval between the two leading jets. This measurement will be discussed fully in Chapter 7.

The number of rapidity gap events in the subsample as a function of $\Delta\eta_c$ (denoted $N_{gap}^{exp}(\Delta\eta_c)$) is shown in Fig. 6-6. For small $\Delta\eta_c$, the number of events is large but falls rapidly as $\Delta\eta_c$ increases until $\Delta\eta_c > 2.7$, where there is a significant enhancement due to the high-$\Delta\eta$ trigger. The number of events in the total inclusive dijet sample (i.e. the final data sample described in Chapter 5) versus $\Delta\eta_c$ is shown for comparison. The data in the figure is summarized in Table 6-3.

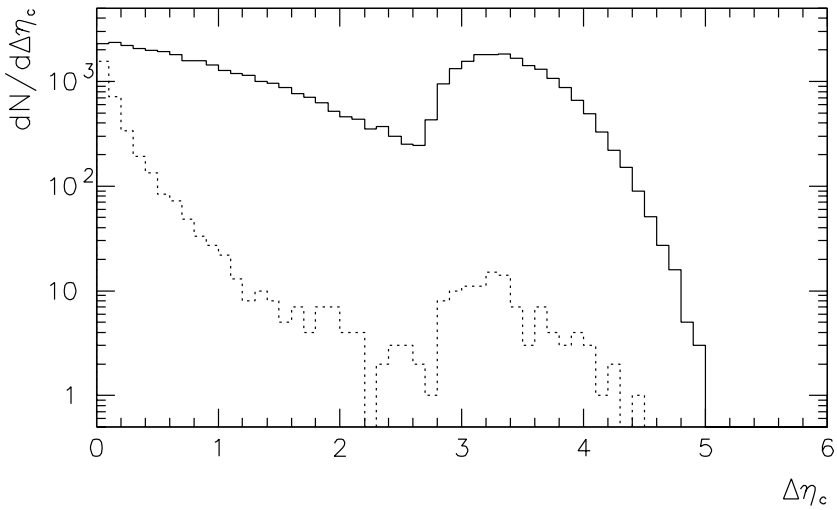

Figure 6-6: The number of events versus $\Delta\eta_c$ for the total inclusive sample (solid line) and the subset with a rapidity gap (dotted line). The statistics are enhanced for $\Delta\eta_c > 2.7$ due to the high-$\Delta\eta$ trigger.

6.4.1 Comparison of Inclusive and Rapidity Gap Samples

Although a rapidity gap is defined in this analysis as no EM towers above an E_T threshold between the two leading jets, gap events typically also have very few hadronic towers or charged tracks between the jets. This "quiet" event topology is apparent in Fig. 6-7 and Fig. 6-8, which show the "detector event display" and "calorimeter tower E_T lego display" respectively, of a typical rapidity gap event with large $\Delta\eta_c$. The detector event display (Fig. 6-7) shows the side view of the DØ tracking system and calorimeter along with the reconstructed vertex position, charged particle tracks, and calorimeter energy deposition. The calorimeter tower E_T lego display (Fig. 6-8) shows the calorimeter η-ϕ "E_T lego" in which the transverse energy deposition in the calorimeter is represented by lego "towers" whose height is proportional to the deposited E_T.

The quiet event topology shown in Figs. 6-7 and 6-8 is strikingly different from that in typical dijet events. An event from the inclusive dijet sample is

$\Delta\eta_c$ Range	$N_{gap}^{exp}(\Delta\eta_c)$	$N(\Delta\eta_c)$
0.0 - 0.1	1558	2286
0.1 - 0.2	712	2345
0.2 - 0.3	335	2194
0.3 - 0.4	191	2063
0.4 - 0.6	217	3904
0.6 - 0.8	120	3357
0.8 - 1.0	60	3020
1.0 - 1.3	43	3602
1.3 - 1.6	23	2820
1.6 - 2.0	25	2611
2.0 - 2.4	10	1616
2.4 - 3.0	27	3498
3.0 - 3.6	61	10045
3.6 - 4.2	22	4717
4.2 - 5.0	3	563

Table 6-3: Number of events in the gap and inclusive samples as a function of $\Delta\eta_c$.

shown in Figs. 6-9 and 6-10 for comparison. In contrast to gap events, typical dijet events have a substantial amount of calorimeter energy between the jets (i.e. many towers) and contain many more charged tracks. The differences between the inclusive sample and the gap subsample are discussed further below.

The rapidity gap subsample has several interesting features that distinguish it from the inclusive sample. As mentioned above, gap events typically have very few hadronic towers and charged particle tracks between the two leading (highest E_T) jets. Figure 6-11 (a) shows the number of hadronic towers above 400 MeV between the jets for events with $\Delta\eta_c > 3$. The gap sample (dotted line) is compared to the inclusive sample (solid line). Also shown is the number of charged particle tracks between the jets originating from the reconstructed vertex position in Fig. 6-11 (b). To reduce background from charged particles that do not originate from the vertex, limits of 2 cm and 10 cm were imposed on the impact parameter and distance from the reconstructed vertex position along the z-axis, respectively. The "quietness" of the rapidity gap sample implies that the gap requirement utilizing the EM

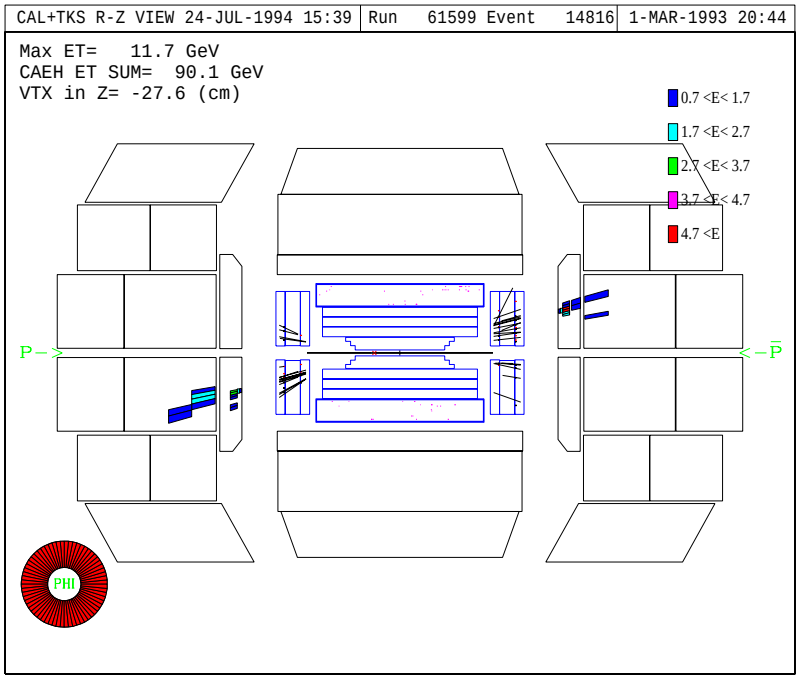

Figure 6-7: Detector event display (side view) of an event from the rapidity gap sample. The display shows reconstructed charged particle tracks in the tracking system and energy deposition in the calorimeter.

calorimeter particle tagging method is sufficient for finding rapidity gap candidate events and that the sample does not contain events with a significant undetected particle flow between the jets.

The rapidity gap subsample has some additional interesting properties that distinguish it from the inclusive sample. The gap sample contains a much larger fraction of exactly two-jet events than the inclusive sample. The jet multiplicity is shown in Fig. 6-12 (a) for the gap sample and the inclusive sample. The gap sample again is much "quieter" due to the explicit requirement of no tagged particles between the jets, which typically excludes additional jets between the two leading jets. In addition, the two leading jets are generally more back-to-back in ϕ than those in the inclusive sample as shown in Fig. 6-12 (b). The jets in the gap sample are also more back-to-back than a sample consisting of events with only two jets

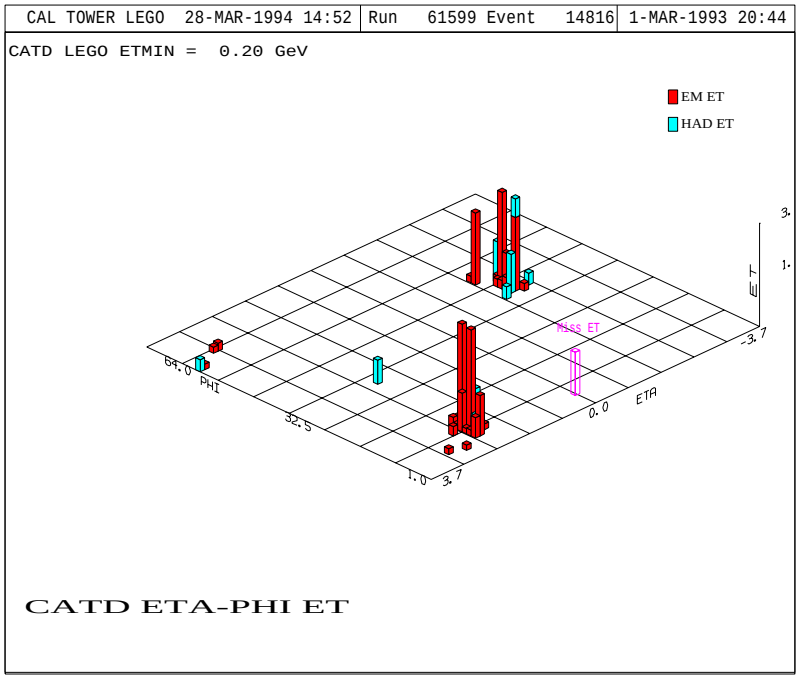

Figure 6-8: Calorimeter η-ϕ "E_T lego" of an event from the rapidity gap sample (same as in Fig. 6-7). The height of each "tower" ($\Delta\eta \times \Delta\phi = 0.1 \times 0.1$) is proportional to the deposited transverse energy.

(with $E_T > 8\,\mathrm{GeV}$). This again indicates that the gap sample has substantially lower particle flow than typical jet events.

In order to make sure that events in the gap sample were not produced by some pathological detector condition, several checks were made on the sample. These included scanning the detector event displays by eye to find any obvious problem with the sample and also comparing the shapes of the jets in the sample to those from the inclusive sample. No event in the sample was found to be the result of an unusual detector effect. This experimental rapidity gap sample is subsequently used for the experimental rapidity gap fraction measurement (next chapter).

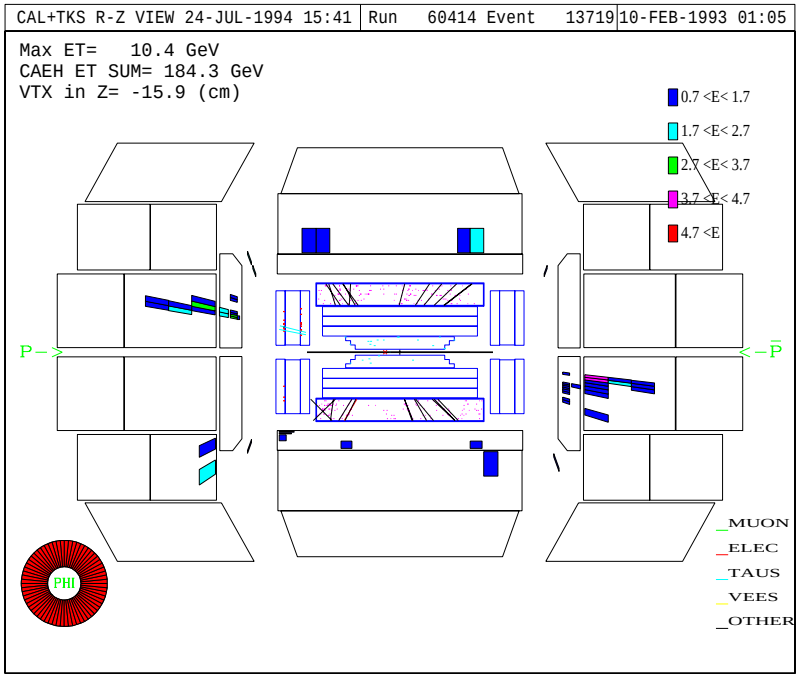

Figure 6-9: Detector event display (side view) of a typical jet event.

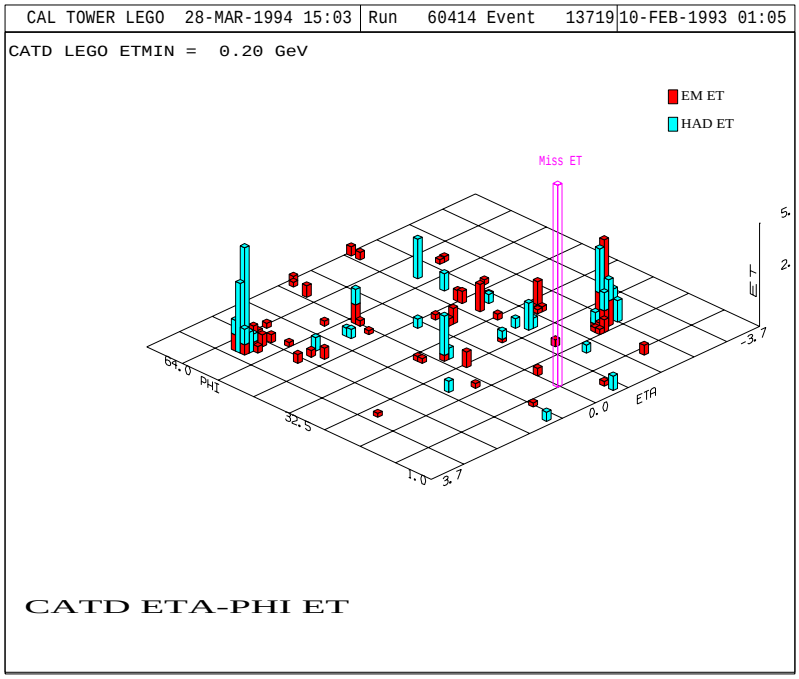

Figure 6-10: Calorimeter η-ϕ "E_T lego" of a typical jet event (same as in Fig. 6-9).

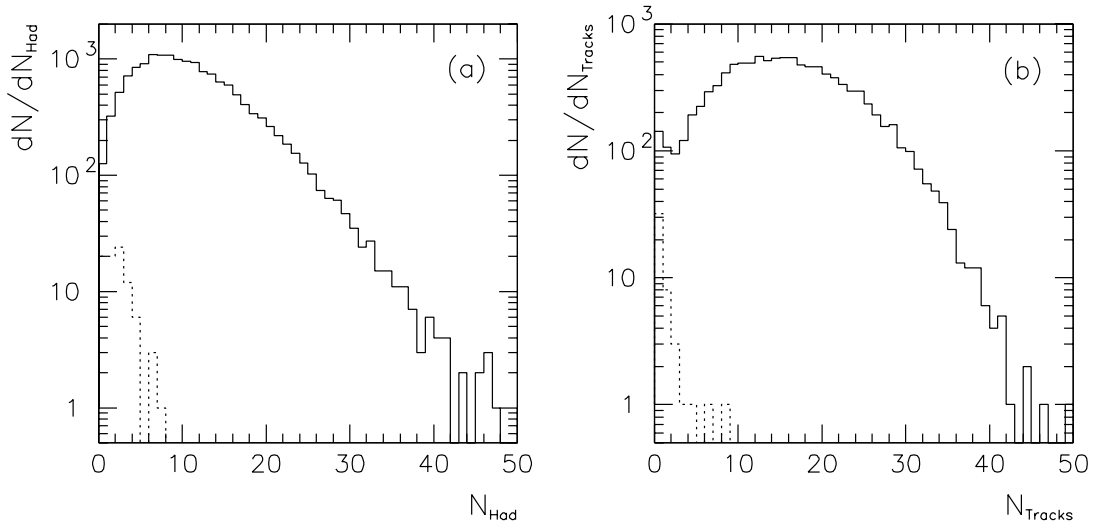

Figure 6-11: The number of hadronic towers (a) and charged tracks (b) for gap events (dotted line) and inclusive events (solid line) with $\Delta\eta_c > 3$.

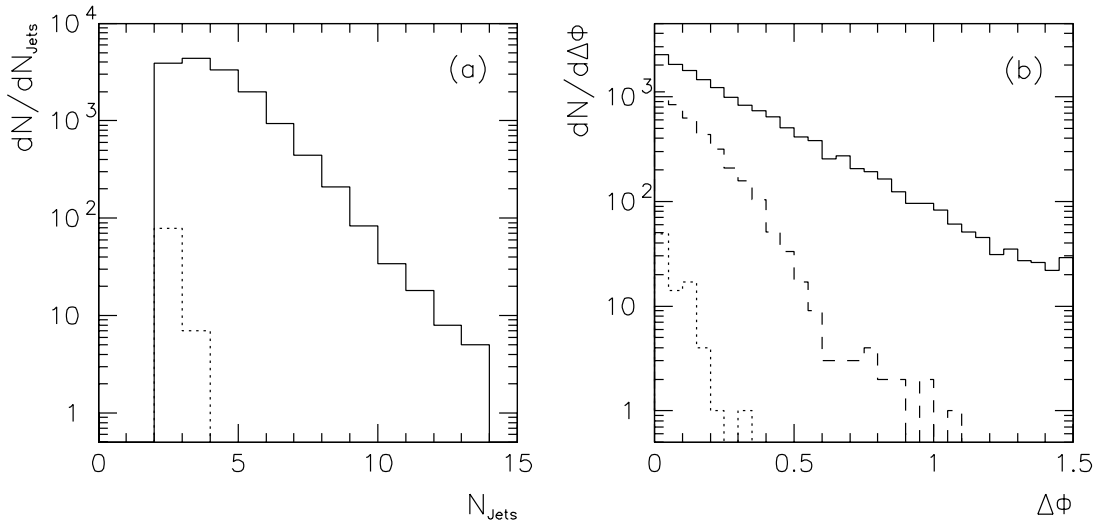

Figure 6-12: The number of jets (a) and the $\Delta\phi = |\phi_1 - \phi_2 - \pi|$ distribution (b) for the rapidity gap sample (dotted line) and inclusive sample (solid line) for events with $\Delta\eta_c < 3$. The dashed line shows the $\Delta\phi$ distribution for events with exactly two jets with $E_T > 8\,\mathrm{GeV}$.

Chapter 7

Rapidity Gap Fraction Measurement

7.1 Experimental Rapidity Gap Fraction

For an ideal detector, the rapidity gap fraction (Eq. 2.3) can be rewritten as

$$f(\Delta\eta_c) \;=\; \frac{N_{gap}(\Delta\eta_c)}{N(\Delta\eta_c)} \;\equiv\; \frac{N_{n=0}(\Delta\eta_c)}{N(\Delta\eta_c)} \tag{7.1}$$

where $N(\Delta\eta_c)$ is the number of events that have jet cones separated by $\Delta\eta_c$, and the subscript $n = 0$ refers to the subset of the sample with no particles between the two leading (highest E_T) jets.

As mentioned in §2.10 however, a direct measurement of $f(\Delta\eta_c)$ is difficult due to the intrinsic inefficiencies of a real detector. Therefore in this analysis the rapidity gap fraction is defined experimentally as the fraction of events with no *tagged* particles between the jets:

$$f(\Delta\eta_c)^{exp} \;=\; \frac{N_{gap}^{exp}(\Delta\eta_c)}{N(\Delta\eta_c)} \;\equiv\; \frac{N_{tagged=0}(\Delta\eta_c)}{N(\Delta\eta_c)} \tag{7.2}$$

where $N_{tagged=0}(\Delta\eta_c)$ is the number of events with no EM towers above a 200 MeV transverse energy threshold between the jets.

7.1.1 "Inclusive" Gap Fraction Measurement

The experimental gap fraction measurement is clearly not an "inclusive" measurement of the rapidity gap fraction due to the particular trigger and offline requirements used in this analysis. A truly inclusive measurement would trigger on only one jet above an E_T threshold, with no η requirements on the jet. Offline, the two leading (highest E_T) jets in each event would be used to determine $\Delta\eta_c$. In this way, the measurement would be unbiased by offline or trigger requirements.

Realistically, however, a truly inclusive trigger is not sufficient to obtain adequate statistics for large $\Delta\eta_c$. Therefore, as mentioned in §5.2, an inclusive trigger is used for small $\Delta\eta_c$, while the high-$\Delta\eta$ trigger, which is non-inclusive, is used for large $\Delta\eta_c$. Although the final combined data sample described in Chapter 5 is non-inclusive, it is possible to use the experimental gap fraction measurement to place an upper limit on the "inclusive" fraction of events with no particles between the jets.

7.1.2 Uncorrected Experimental Gap Fraction

The experimental rapidity gap fraction of Eq. 7.2 is plotted in Fig. 7-1 as a function of $\Delta\eta_c$, where the error bars show the statistical error only (binomial errors). The measurement has not been corrected for effects that have biased it to a systematically lower or higher value with respect to an inclusive measurement. These systematic biases are discussed further below in relation to the experimental gap fraction measurement and the upper limit.

7.1.3 Interpretation of Experimental Gap Fraction

The uncorrected experimental gap fraction exhibits the expected qualitative behavior discussed in §2.10: for small $\Delta\eta_c$ (< 2) it falls steeply with increasing $\Delta\eta_c$

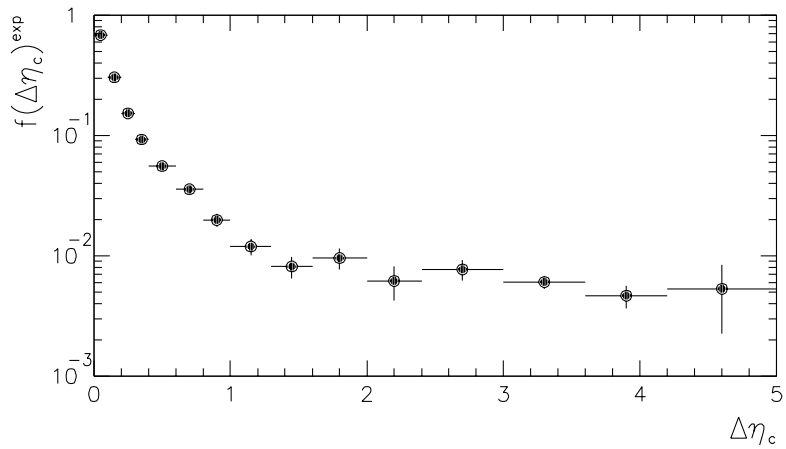

Figure 7-1: The uncorrected experimental rapidity gap fraction. The fraction of events having no tagged particles between the two leading jets is measured as a function of $\Delta\eta_c$. The error bars show the statistical error only.

as expected for color-octet exchange, while for larger $\Delta\eta_c$ the fraction is relatively constant as expected for color-singlet exchange. However, due to systematic biases in the measurement (discussed in §7.2 below) it is not possible to attribute the flattening in $f(\Delta\eta_c)^{exp}$ solely to color-singlet exchange. In addition, uncertainty in the contribution from color-octet exchange (§2.9.3) and the effect of particle detection inefficiencies (§2.10) also make it difficult to attribute the flattening to pure color-singlet exchange.

7.1.4 "Color-Octet" Gap Fraction Measurement

Although the experimental gap fraction is subject to systematic biases and theoretical uncertainties, comparison with an experimental "color-octet" gap fraction is possible, thus allowing a qualitative interpretation of the shape (flattening). By comparing the experimental gap fraction to a "color-octet" gap fraction from the same data sample, experimental biases and uncertainties are largely taken into account.

The color-octet sample is obtained by requiring a third jet ($E_T > 8\,\mathrm{GeV}$) in

the $\Delta\eta_c$ region between the two leading jets. This jet effectively "tags" color-octet events by virtue of the hard radiation (jet) between the jets. A color-octet "gap" subsample is obtained by requiring no tagged particles between the two leading jets, exclusive of the multiplicity from the third jet itself (within a cone of $R = 0.7$). By removing the tagged particle multiplicity from the jet, only the remaining "color-octet" radiation between the jet is measured in order to obtain the gap fraction. Figure 7-2 shows the resulting "color-octet" gap fraction compared to the "nominal" gap fraction measurement. Unlike the nominal measurement, the "color-octet" gap fraction continues to fall for $\Delta\eta_c > 2$, indicating that in these events—which presumably have no color-singlet contribution—there is no significant flattening at large $\Delta\eta_c$.

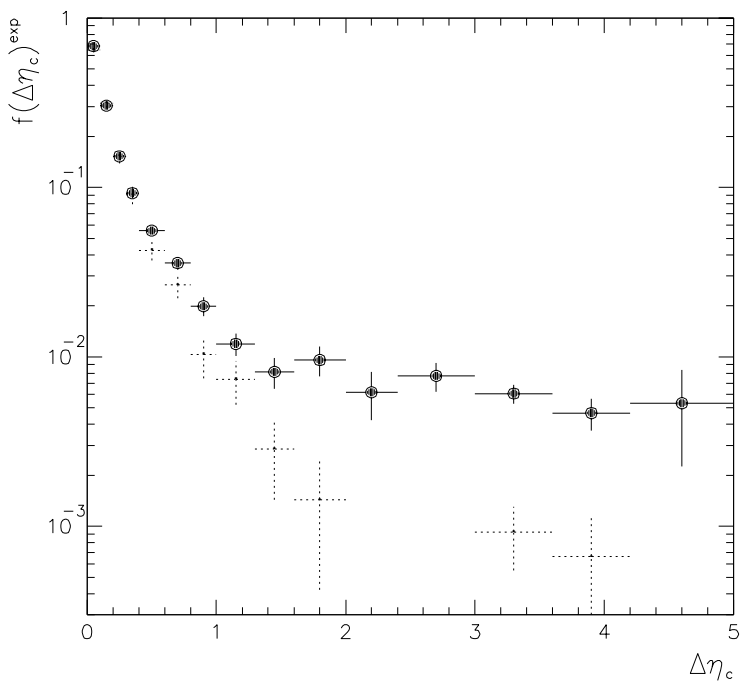

Figure 7-2: Experimental gap fraction compared to the "color-octet" gap fraction. The nominal measurement (solid circles) is compared to the measurement for events containing a third jet between the leading jets whose tagged particle multiplicity is removed within a cone of $R = 0.7$ (dotted).

Although the qualitative disagreement in the shapes from the two measurements is suggestive of the observation of color-singlet exchange, the "color-octet" sample used here is clearly a subsample of all color-octet events, since a third jet with sufficient E_T is required to obtain the sample. However, if the "color-octet" sample is representative of all color-octet jet events, then the flattening is very likely due to color-singlet exchange.

7.1.5 Upper Limit Considerations

Due to the flattening in the experimental gap fraction and the large suppression of the color-octet contribution expected large $\Delta\eta_c$, an upper limit will be placed on the true rapidity gap fraction using the experimental gap fraction for $\Delta\eta_c > 3$, which is measured to be

$$f(\Delta\eta_c > 3)^{exp} \quad = \quad (5.6 \pm 0.6^{(stat)}) \times 10^{-3}.$$

This value has not been corrected for the systematic biases described in the sections below. Corrections for these biases are discussed in Chapter 8, and the corrected experimental gap fraction is subsequently used to place an upper limit on $f(\Delta\eta_c)$ for $\Delta\eta_c > 3$.

7.2 Systematic Biases

The measurement of the gap fraction can be biased by trigger requirements, offline cuts, reconstruction methods, various physical processes, or undesirable detector effects. Effects that artificially reduce the gap fraction can cause a measured upper limit that is too small. These must be corrected for before determining the upper limit. Conversely, effects that artificially increase the gap fraction result in a higher, less restrictive upper limit, but do not affect the validity of the limit. Systematic

effects that can potentially bias the gap fraction measurement include:

- Particle tagging inefficiency
- Level 1 trigger requirements
- High-$\Delta\eta$ trigger requirements
- Jet trigger E_T inefficiency
- Offline E_T requirements
- Jet reconstruction uncertainties
- Spurious jets
- Calorimeter noise contamination
- Multiple interaction contamination
- Out-of-cone effects

These effects are discussed in detail in the following sections.

7.2.1 Particle Tagging Inefficiency

Effects that increase the measured gap fraction are not a large concern for this analysis since they result in an increased upper limit but do not affect the validity of the limit. The largest effect increasing the measured gap fraction arises from particle detection inefficiencies, which are inherent in any real detector. Inefficiencies can cause events with particles between jets to be misidentified as rapidity gap events, i.e. $N_{gap}^{exp} > N_{gap}$. Since this effect cannot be corrected without *a priori* knowledge of the underlying particle multiplicity distribution, the measured gap fraction is necessarily higher than the true gap fraction.

Particle Tagging "Definition" Dependence

This analysis uses the lowest EM tower transverse energy threshold of 200 MeV (see §6.1) in order to maximize particle tagging efficiency and obtain the lowest unbiased gap fraction measurement possible. However, it is instructive to vary the threshold

to illustrate the dependence of the gap fraction measurement on particle detection efficiency. The gap fraction is shown in Fig. 7-3 for EM tower E_T thresholds of 200, 300, 500, 750 MeV, and 1 GeV. The estimated tagging efficiency for the various E_T thresholds compared to the 200 MeV threshold is shown in Table 7-1.

The qualitative agreement of Fig. 7-3 with Figs. 2-23 and 2-24, indicates that for the higher thresholds color-octet fluctuations dominate, while for the lower thresholds they are substantially reduced. In addition, for lower thresholds the gap fraction begins to "flatten" at lower $\Delta\eta_c$, which is consistent with expectations for color-singlet exchange. Thus, although a lower threshold is expected to give a lower gap fraction, the gap fraction obtained from the 200 MeV tagging threshold is sufficient to place an interesting upper limit on the true gap fraction, since the contribution from color-octet exchange is largely reduced.

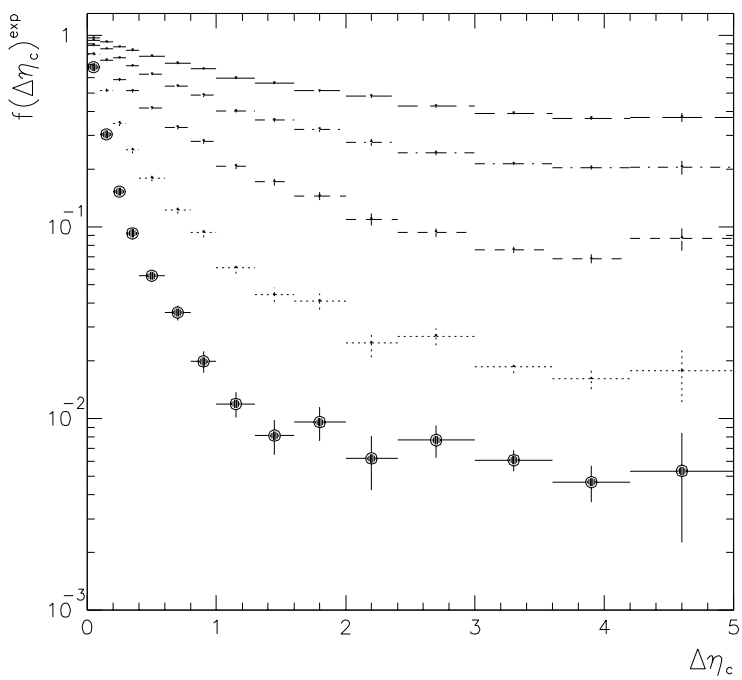

Figure 7-3: The dependence of the experimental rapidity gap fraction on particle tagging threshold. The gap fraction is plotted for EM tower transverse energy thresholds of 200, 300, 500, 750 MeV, and 1 GeV (bottom to top, respectively).

Threshold	Efficiency
300 MeV	51 %
500 MeV	24 %
750 MeV	12 %
1 GeV	7%

Table 7-1: Estimated tagging efficiencies for various EM tower thresholds relative to the 200 MeV threshold.

7.2.2 Trigger Biases

As mentioned in §5.3 and §5.3.2, the trigger requirements are not purely inclusive and result in a biased sample that can affect the rapidity gap fraction measurement. The possible biases are discussed below.

Level 1 Trigger Bias

As mentioned in §5.3.2, the level 1 jet triggers may bias the sample towards quark jets when the jet triggers are not fully efficient, especially for jets with $E_T < 35$ GeV. This can potentially artificially decrease the measured gap fraction since quark and gluon jet events may have different gap "production" cross sections. However, since the magnitude of the quark bias is difficult to determine, its effect can not be accounted for. The possible effect of this bias is discussed in Appendix A.

High-$\Delta\eta$ Trigger Acceptance Loss

The pseudorapidity requirements of the high-$\Delta\eta$ trigger causes an acceptance loss near the $\Delta\eta_c$ threshold resulting in a biased η_{boost} distribution. For events with $\Delta\eta_c \gtrsim 2.6$ these requirements do not accept events with large η_{boost} and therefore cause a significant acceptance loss (see Figs. 5-8, 5-10(b) and 5-11). Although this bias has a negligible effect on the gap fraction measurement as a function of $\Delta\eta_c$, it can affect the value if large bins in $\Delta\eta_c$ are used since points at lower $\Delta\eta_c$ are

weighted less than they would be from an inclusive measurement.

The acceptance loss for the final sample is determined by first assuming that the $\Delta\eta_c$ distribution of the inclusive trigger is unbiased and truly inclusive, given the offline requirements of Chapter 5. The acceptance of the high-$\Delta\eta$ trigger is calculated by taking the ratio of the fits to the $\Delta\eta_c$ distributions of the two triggers. The resulting "acceptance" curve for the high-$\Delta\eta$ trigger as a function of $\Delta\eta_c$ is shown in Fig. 7-4. Also shown is the acceptance corrected $\Delta\eta_c$ distribution for the high-$\Delta\eta$ trigger, which will be used in the subsequent upper limit determination of Chapter 8.

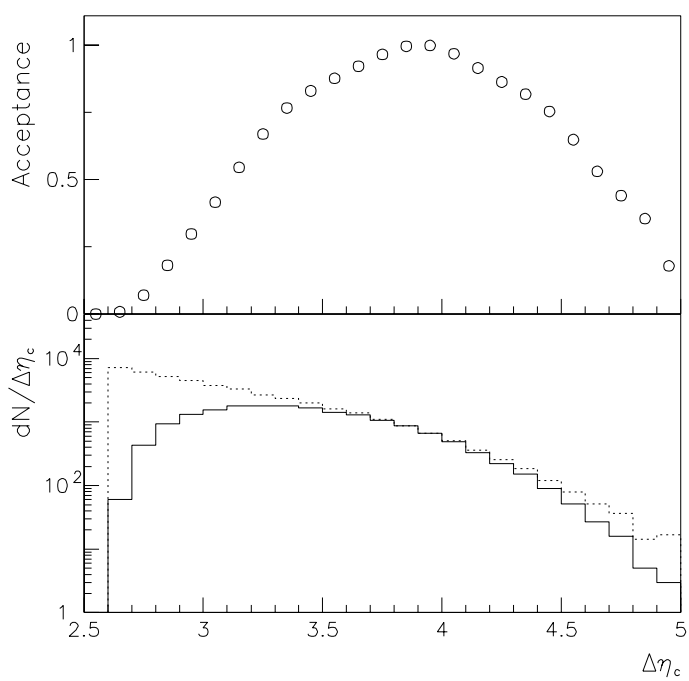

Figure 7-4: The $\Delta\eta_c$ acceptance (top) for the high-$\Delta\eta$ trigger as a function of $\Delta\eta_c$. The bottom plot shows the $\Delta\eta_c$ distribution for the high-$\Delta\eta$ trigger (solid curve) and the distribution corrected for the acceptance loss (dotted curve).

High-$\Delta\eta$ Trigger η_{boost} Bias

The biased η_{boost} distribution in the high-$\Delta\eta$ trigger can indirectly affect the gap fraction measurement by biasing the initial parton distributions. However, since this bias is expected only to increase the measured gap fraction, it will not be accounted for. The possible effect of this bias is discussed in Appendix A.

Comparison of the Inclusive and High-$\Delta\eta$ Triggers

Although the jet pseudorapidity requirements of the high-$\Delta\eta$ trigger produce a biased sample compared to the inclusive trigger, the gap fraction is not very sensitive to the differences in the triggers. The gap fraction obtained from the combined sample (which contains both triggers) is compared to the gap fraction from the inclusive trigger sample in Fig. 7-5. The gap fraction obtained from the inclusive and high-$\Delta\eta$ triggers in the region of overlap ($\Delta\eta_c > 2.7$) is consistent within statistical errors.

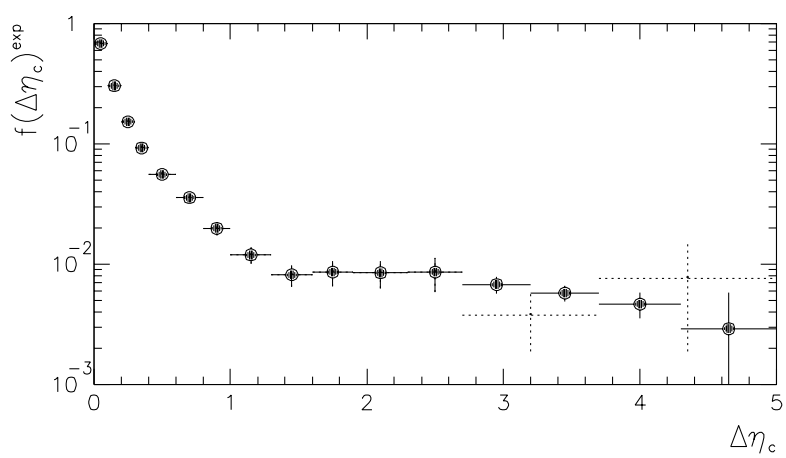

Figure 7-5: The experimental rapidity gap fraction from the combined final data sample (solid points) compared to that from the inclusive trigger only (dotted). The gap fraction from the combined data sample has been rebinned for $\Delta\eta_c > 2.7$ in order to allow comparison of the two measurements (triggers) bin by bin.

7.2.3 Jet E_T Effects

Jet E_T Dependence

The jet trigger inefficiency as a function of the second leading jet E_T (especially for $E_T < 40\,\mathrm{GeV}$) can affect the gap fraction measurement via a possible level 1 bias or a bias in the shape of the E_T distribution. To determine if there is a significant bias on the the gap fraction caused by trigger inefficiency and/or if there is a significant E_T dependence, the gap fraction is measured in three jet E_T bins: $E_T = 30 - 35\,\mathrm{GeV}$, $E_T = 35 - 40\,\mathrm{GeV}$, and $E_T > 40\,\mathrm{GeV}$.

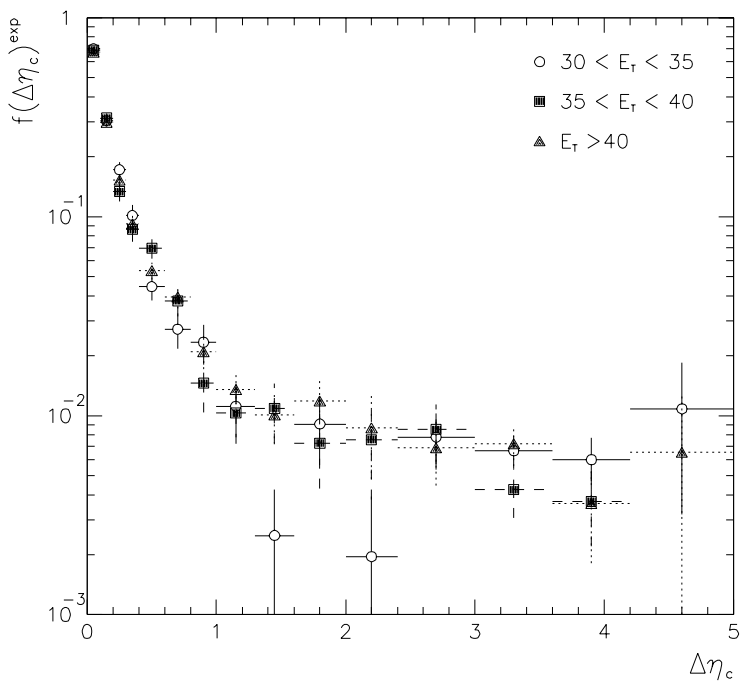

Figure 7-6: The gap fraction measurement versus jet E_T. The fraction is shown for three jet E_T bins (in GeV): $30 < E_T < 35$ (open circles), $35 < E_T < 40$ (squares), and $E_T > 40$ (triangles).

The resulting gap fraction for each E_T bin is shown in Fig. 7-6. The fractional difference in the gap fraction measurement compared to the standard gap fraction measurement (for $\Delta\eta_c > 3$) is shown in Table 7-2. Although the different E_T

bins differ slightly from the nominal measurement, they are reasonably consistent within statistical errors indicating that:

- the gap fraction is weakly dependent on jet E_T and the trigger inefficiency biases discussed above; or
- the effects roughly cancel each other; or
- the effects are masked by the relatively large statistical errors.

In this analysis it is assumed that the bias in the gap fraction measurement due to the trigger inefficiency is not significant and that the data sample used for the gap fraction measurement is unaffected.

Jet E_T	% Difference
30 – 35 GeV	17 ± 14
35 – 40 GeV	-31 ± 12
> 40 GeV	10 ± 20

Table 7-2: The fractional difference $(f - f_{E_T})/f$ between the nominal gap fraction measurement and the measurement binned in jet E_T for $\Delta\eta_c > 3$.

Offline Jet E_T Requirement

The gap fraction measurement is not inclusive due to the nature of the trigger and offline requirements on the jets. Therefore, the offline cuts on the jets ($E_T >$ 30 GeV) are used with the understanding that direct comparison to theory must be made using the same requirements. Nevertheless, the offline cuts do not affect the validity of placing an upper limit on an inclusive sample since at worst the requirements only increase the observed gap fraction.

The offline jet E_T requirement biases the data sample towards two-jet events. The high-$\Delta\eta$ trigger is already biased due to its jet E_T requirements. To illustrate this bias and its effect on the gap fraction, the second leading jet E_T requirement was decreased from 30 GeV to 20 GeV. This less restrictive requirement allows a

larger fraction of multijet events into the sample. Figure 7-7 shows the fractional increase in the jet multiplicity distribution resulting from the lower jet E_T requirement. This enhancement of multijet events is expected to cause a decrease in the measured gap fraction.

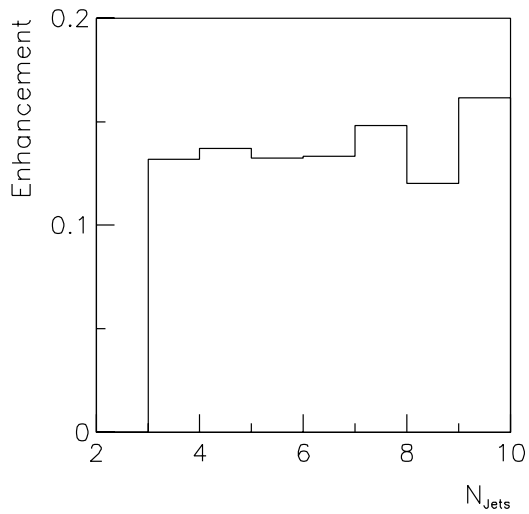

Figure 7-7: The fractional enhancement in multijet multiplicity for events with a second leading jet $E_T > 20\,\mathrm{GeV}$ compared to events with the standard offline cuts. Zero denotes no enhancement.

Figure 7-8(a) shows the effect on the measured gap fraction of reducing the E_T requirement on the second leading jet. The effect is significant for the inclusive trigger, which is $(53 \pm 25)\%$ lower than the nominal measurement. In contrast, the effect on the high-$\Delta\eta$ trigger is negligible since this bias is already imposed by the high-$\Delta\eta$ trigger due to its two-jet requirement.

To further illustrate the effect of reducing the E_T requirement on the second leading jet, Fig. 7-8(b) shows the measured gap fraction obtained from events containing at least three jets ($E_T > 8\,\mathrm{GeV}$). The resulting gap fraction is decreased significantly compared to the standard gap fraction measurement due to the increased probability of additional particles between the jets. In contrast, the gap fraction for events with exactly two jets is significantly higher than the nominal

measurement.

Therefore, although the offline jet E_T requirement (on both jets) biases the sample towards two-jet events, the sample can still be used to place an upper limit on the true inclusive rapidity gap fraction since it only increases the measured gap fraction.

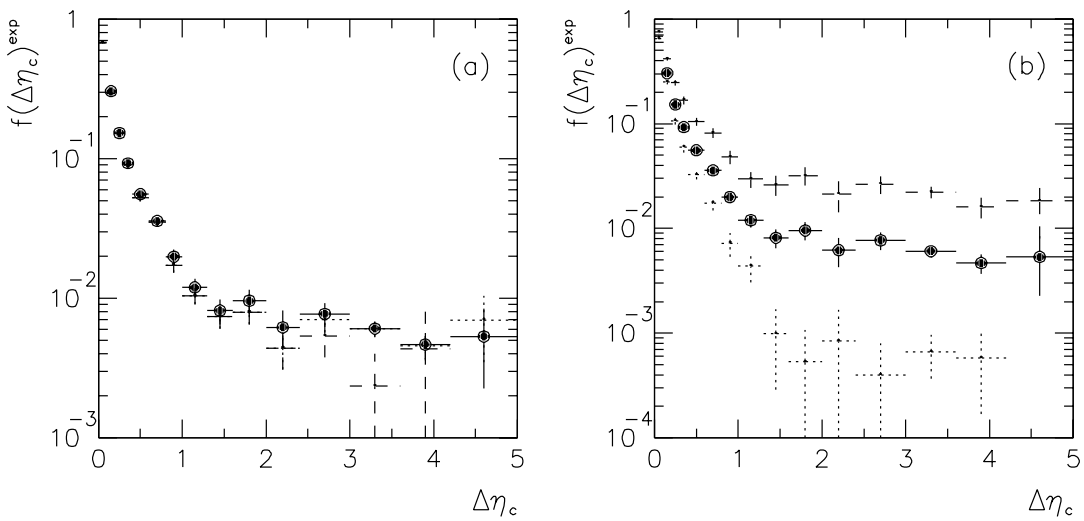

Figure 7-8: Effect on the measured rapidity gap fraction of the lower E_T requirement on the second leading jet, and the dependence of the gap fraction on number of jets in each event. Figure (a) shows the nominal measurement (solid circles) compared to the measurement with $E_T > 20\,\mathrm{GeV}$ for the combined data sample (dotted) and the inclusive trigger only (dashed). Figure (b) shows the nominal measurement (solid circles) compared to the measurement for events containing at least three jets (dotted) and exactly two jets (dashed).

7.2.4 Jet Reconstruction Biases

The experimental gap fraction is implicitly dependent on the measured E_T and η of the two leading jets. However, the reconstructed jet E_T and η position can have systematic deviations from the true values in addition to a finite resolution, which can possibly affect the gap fraction measurement.

Jet Energy Scale Correction Uncertainty

The jet energy scale correction, described in §4.5, has an uncertainty arising from the statistical and systematic error of the jet energy scale measurement. These errors account for the possible error in the nominal energy scale correction. Mismeasurement of jet transverse energy can affect the gap fraction measurement if it is strongly dependent on jet E_T. However, as discussed previously, the measured gap fraction has little observed dependence on jet E_T, and the error in the jet energy scale correction is therefore not expected to affect the measured gap fraction significantly.

For completeness the gap fraction was calculated using jets which were corrected using the "low" and "high" error bands shown in Fig. 4-2. The resulting gap fraction measurements were virtually identical and were well within the statistical uncertainty. To determine the maximum effect of the error in the energy scale, the ratio of the low and high gap fraction measurements was calculated. For $\Delta\eta_c > 3$ the gap fraction changed by $(2 \pm 3)\%$. As discussed in §7.2.3 above, the measured gap fraction has no obvious dependence on jet E_T, therefore, the jet energy scale correction is assumed not to bias the measurement.

Jet Position Uncertainty

As mentioned in §4.3, the reconstructed jet position in η has an associated resolution (uncertainty) and systematic shift from the true value. The estimated effect on the jet η position due to jet reconstruction has been determined to be approximately 0.02 to 0.06 in η, depending on the particular Monte Carlo event generator used. This presumably can affect the accuracy of $\Delta\eta_c$ and the resulting gap fraction measurement. However, this effect is assumed to be negligible for large $\Delta\eta_c$ since the measured gap fraction is roughly constant.

Spurious Jets

As discussed in §4.4, certain anomalous energy depositions can be reconstructed as jets. These spurious jets are largely removed from the event sample (Chapter 5) in order to obtain a pure sample of real jet events, and less than 1% of events are expected to contain a spurious jet.

Spurious jets contamination in the event sample is not likely to significantly affect the measured gap fraction. Figure 7-9 shows the gap fraction obtained from events that contain an identified spurious jet, compared to the nominal measurement. For $\Delta\eta_c > 3$ the gap fraction changes by only $(-3 \pm 22)\%$, and the 1% spurious jet contamination is not expected to significantly affect the measurement.

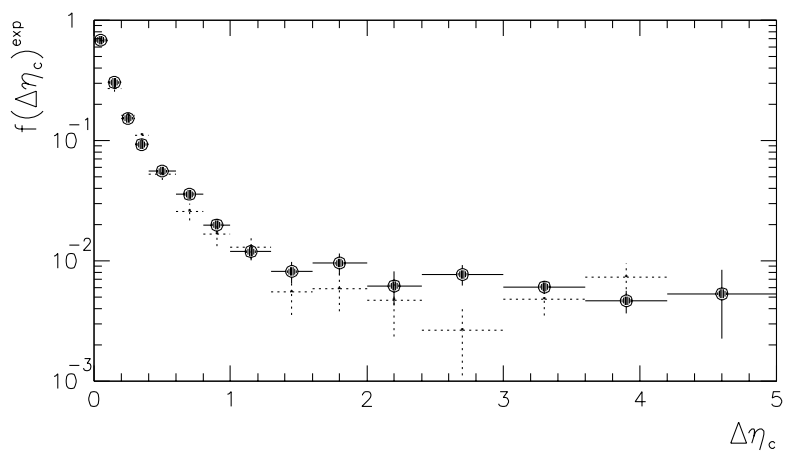

Figure 7-9: The effect of spurious jet contamination on the measured gap fraction. The standard gap fraction measurement (solid circles) is compared to the measurement with identified spurious jets in each event (dotted).

7.2.5 Multiple Interaction Contamination

The gap fraction measurement can also be biased by events that contain more than one inelastic collision per $p\bar{p}$ bunch crossing. These events are likely to cause an artificial loss of rapidity gap events since they include a large source of particles

not associated with the triggering (jet) interaction.

To illustrate this effect, the gap fraction was measured for events that did not satisfy the level 0 single interaction requirement of §5.4.3. Figure 7-10 shows the effect of multiple interactions on the measured gap fraction compared to the standard gap fraction. The measured gap fraction is significantly lower due to particles from additional interactions filling the gap. As discussed in §5.4.3, these events are largely excluded from the final data sample, and less than 5% of events in the sample are expected to contain multiple interactions.

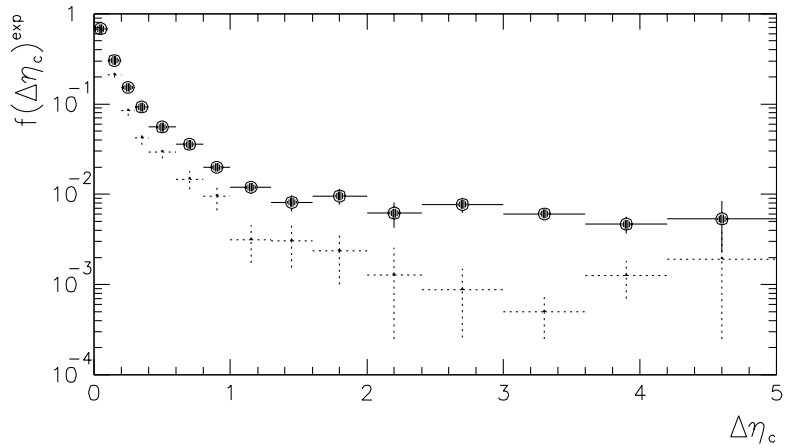

Figure 7-10: The effect of multiple interactions on the measured gap fraction. The standard gap fraction measurement with the single interaction requirement (solid circles) is compared to the measurement with a large fraction of multiple interactions (dotted).

7.2.6 Calorimeter Noise Contamination

Noise that produces spurious or "fake" tagged particles in a rapidity gap can cause the loss of rapidity gap events and thus bias the measured gap fraction. As mentioned in §3.2.2, the particular method for tagging particles in this analysis produces only a small noise contamination, and less than 5% of gap events are expected to contain a "fake" tagged particle. In addition to normal calorimeter

noise, especially "noisy" calorimeter channels can significantly affect the the gap fraction. These have been largely suppressed (see §6.3), and less than 5% of gap events are expected to have some "hot" channel contamination.

7.2.7 Out-of-cone Effects

Jet out-of-cone calorimeter showering can also significantly decrease the experimental gap fraction. Particles within a fixed jet cone can deposit energy outside the cone due to calorimeter shower broadening (η smearing) and thus contaminate rapidity gap events. In the calorimeter, this effect is indistinguishable from out-of-cone radiation (discussed in §2.8.3), in which jets from color-singlet exchange events hadronize producing particles outside of a fixed jet cone between the jets. Although both effects can reduce the observed gap fraction by producing tagged particles between the jets, out-of-cone calorimeter showering is a purely instrumental effect that should be corrected for before determining an upper limit.

One method of reducing the instrumental out-of-cone effect is to increase the cone radius used in the definition of $\Delta\eta_c = |\eta_1 - \eta_2| - 2R$. Although a sufficiently large radius could be chosen to significantly reduce this effect, the measured gap fraction would include a larger contribution from color-octet fluctuations (§2.9.3) due to the smaller η-ϕ region between the jets. The measured gap fraction would therefore increase due to the reduced out-of-cone detector effects as well as the increased contribution from color-octet fluctuations.

A method which is less sensitive to color-octet fluctuations utilizes the event η-ϕ topology shown in Fig. 7-11(a). The out-of-cone effect can be determined by excluding cones of various size around the two leading jets. The shaded region between the jets exclusive of the extended cone region around the jet is used to measure the gap fraction as a function of excluded cone size. Figure 7-12(a) shows the resulting gap fraction for $R = 0.7$, 1.1, and 1.5. For cone sizes larger

than nominal (0.7), the measured gap fraction increases due to excluding tagged particles in the $\Delta\eta_c$ region associated with the leading jets. For small $\Delta\eta_c$ ($\lesssim 2$) the gap fraction increases substantially due to the proportionally large region of η-ϕ space excluded by the cones between the jets, which allows a substantially color-octet contribution from fluctuations.

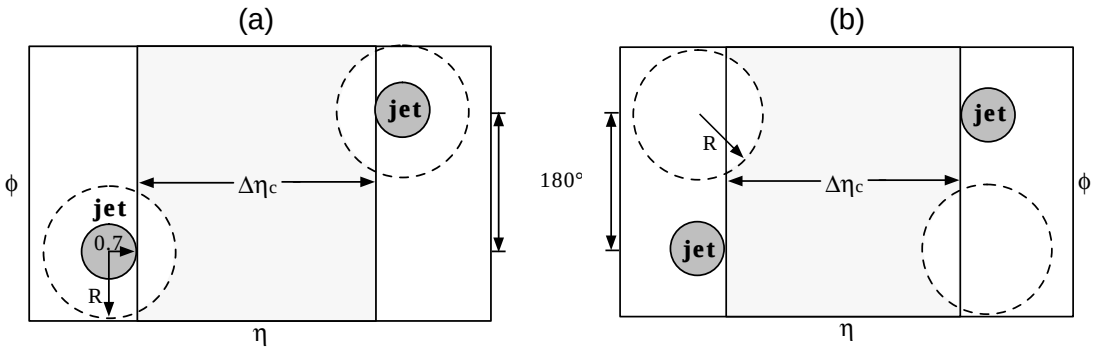

Figure 7-11: The "out-of-cone" (a) and "away-cone" (b) gap η-ϕ topology. The shaded region between the jets and not inside the extended cones is used to determine the out-of-cone effect (a) or the away-cone effect (b) on the measured gap fraction where $\Delta\eta_c$ is defined using $R = 0.7$.

It is not obvious that the "out-of-cone" effect observed for large $\Delta\eta_c$ in Fig. 7-12(a) does not arise solely from the reduced area in η-ϕ space between the jets caused by excluding large cones. To show that the increase arises primarily from out-of-cone effects associated with the jets, the gap fraction is measured excluding similar cones 180° away in ϕ from the two leading jets (Fig. 7-11(b)). In this case, the gap fraction, shown in Fig. 7-12(b), has a much smaller increase indicating that additional particles near the $\Delta\eta_c$ edge are more likely to be associated with the leading jets. Figure 7-13 shows the increase in the measured gap fraction for $\Delta\eta_c > 3$ resulting from the "out-of-cone" and "away-cone" gap topologies.

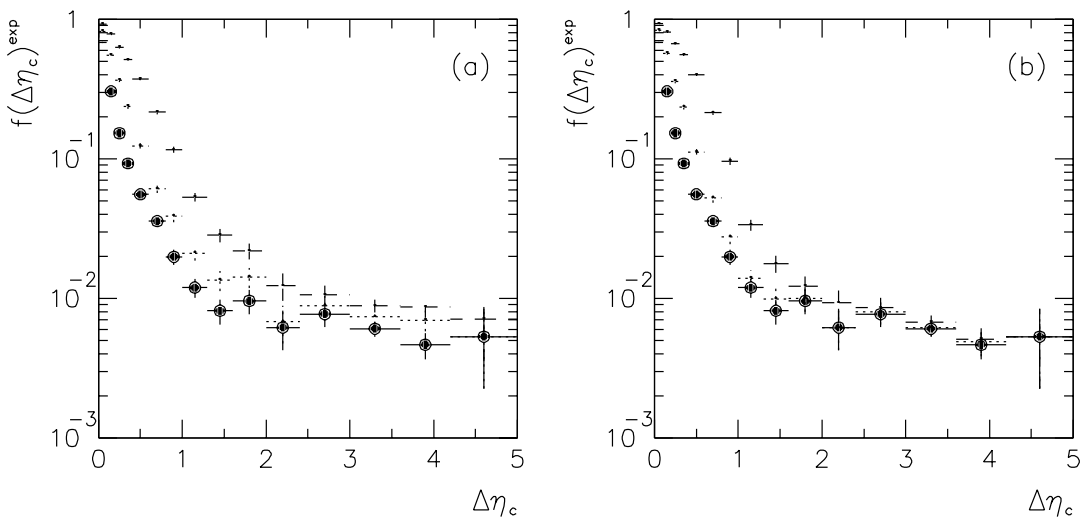

Figure 7-12: The effect of excluding "out-of-cone" (a) and "away-cone" (b) tagged particles on the measured gap fraction. The standard gap fraction with $R = 0.7$ (solid circles) is compared to the gap fraction using $R = 1.1$ (dotted) and $R = 1.5$ (dashed).

Components of the Out-of-cone Effect

The out-of-cone effect observed in Fig. 7-13 has contributions from different sources. These are described below:

- For gap events in which all particles associated with the jets are inside the jet cones (i.e. true rapidity gaps), out-of-cone effects arise from out-of-cone calorimeter showering and showering in the central detector in front of the calorimeter. Since these are *instrumental* effects, they must be corrected for before placing an upper limit on the gap fraction. These "true" gap events are expected to occur in a large portion of color-singlet events and some portion of color-octet events.

- In color-singlet events (if they exist), there is an additional contribution from out-of-cone radiation into the $\Delta\eta_c$ region. As mentioned in §2.8.3, this radiation is expected to become rapidly suppressed for $R > 0.7$. Correcting

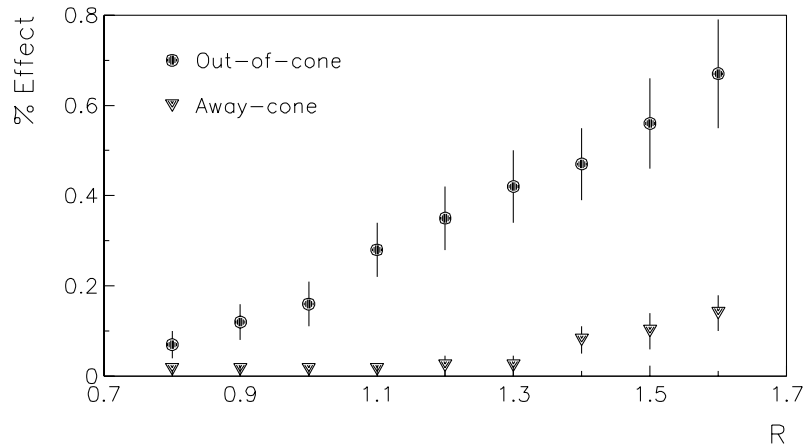

Figure 7-13: The effect of the "out-of-cone" and "away-cone" gap topologies on the measured gap fraction for $\Delta\eta_c > 3$. The fractional increase in the measured gap fraction is shown as a function of cone radius R.

for this *physics* effect allows comparison to parton level predictions for color-singlet exchange.

- In color-octet events, the out-of-cone "radiation" is substantial due to particle production (hadronization) between the jets. Color-octet fluctuations are expected to significantly increase the observed out-of-cone effect.

- Additional particles from spectator interactions (§2.3.5 and §2.9.5) can also increase the observed out-of-cone effect for both color-singlet and color-octet events. Ideally particles from the underlying event should be accounted for in determining the out-of-cone effect.

Figure 7-14 illustrates the expected qualitative behavior for each component as a function of cone radius, R. For small cones, the out-of-cone effect is small but increases rapidly with R due to the increased probability for out-of-cone tagged particles in the larger cones. For sufficiently large cones, however, both out-of-cone calorimeter showering and color-singlet out-of-cone radiation are expected to flatten out. Spectator interactions are expected to add a small rising contribution

to all processes. In contrast, the contribution from color-octet fluctuations is expected to be large and continue increasing with R. The total observed out-of-cone effect depends on the relative contributions from each effect.

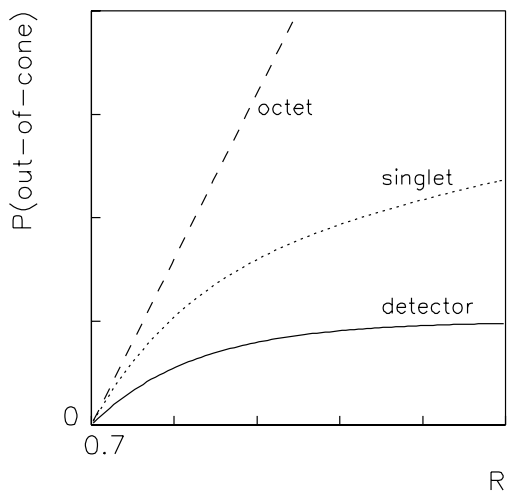

Figure 7-14: The expected qualitative behavior of the contributions to the out-of-cone effect. The solid line illustrates the effect of out-of-cone calorimeter showering while the dotted line shows the behavior for color-singlet events when spectator interactions and out-of-cone radiation are included. The dashed line illustrates the out-of-cone effect from fluctuations in color-octet events.

Out-of-cone Measurement

The "out-of-cone" effect shown in Fig. 7-13 is sensitive to color-octet fluctuations and spectator interactions which can significantly increase the observed effect. In order to minimize these contributions, a subsample of "loose" gap events is used. This sample is obtained by taking events with $\Delta\eta_c > 3$ which have no particles between the jets for $\Delta\eta_c{}' = |\eta_1 - \eta_2| - 2(1.7)$ where the cone size is $R = 1.7$ as opposed to the nominal radius of 0.7. Figure 7-15 shows this event topology. The "out-of-cone" region is denoted by the shaded region A, and the "away-cone" region is denoted by B.

The out-of-cone effect is defined as the probability that a tagged particle in

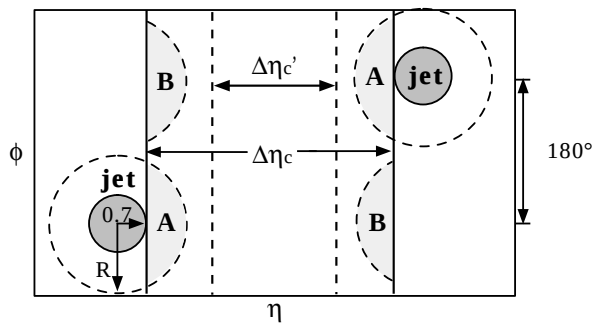

Figure 7-15: The event topology used to determine detector out-of-cone effect. Region B is used to measure the underlying tagged particle probability while region A is used to determine the tagged particle probability near the jets. Only events with no particles in the $\Delta\eta_c' = |\eta_1 - \eta_2| - 2(1.7)$ region are used.

region A is associated with the nearest leading jet. However, region A can contain an additional "underlying" event tagged particle contribution. Therefore, region B is used to determine the underlying contribution since it has the same particle tagging efficiency as region A and is well separated from the jet in ϕ. The probability that a tagged particle in region A is correlated to the jet is then

$$P(\text{out-of-cone}) \quad = \quad 1 - P_A(n_{tag} = 0)/P_B(n_{tag} = 0)$$

where $P(n_{tag} = 0)$ is the probability that no tagged particle is in the particular region. Figure 7-16 shows the resulting out-of-cone probability as a function of the cone radius. This probability is significantly smaller than the effect shown in Fig. 7-13. In addition, the flattening indicates a reduced contribution from color-octet fluctuations and spectator interactions.

Although the measured out-of-cone effect shown in Fig. 7-13 is much more representative of the actual effect, since the color-octet contribution has been largely reduced, it should be considered an upper limit on the instrumental effect since it is not possible to totally exclude the contribution from color-octet fluctuations. In addition, the sample used for the measurement is expected to contain almost

all color-singlet events (if they exist) due to the rather loose gap requirement. Therefore, the measured out-of-cone effect is also expected to contain out-of-cone radiation effects in color-singlet events. Consequently, the measured out-of-cone effect can either be considered an upper limit on the instrumental effect or a measurement of both the instrumental and color-singlet out-of-cone effects.

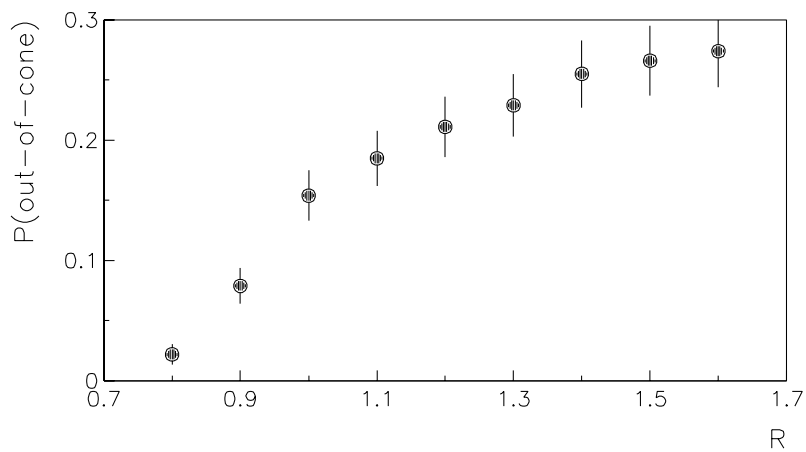

Figure 7-16: The out-of-cone effect as a function of cone radius for $\Delta\eta_c > 3$.

7.2.8 Summary of Biases

The biases in the measured gap fraction given above are summarized in Table 7-3. For each bias, the expected size and direction of its effect is shown relative to an unbiased gap fraction measurement. Effects which bias the gap fraction to an artificially larger measured value are at the top of the table. These effects do not need to be corrected for, since they do not affect the validity of an upper limit. However, effects which bias the gap fraction to a lower value must be accounted for before determining an upper limit.

Origin of Bias	Direction	Size of Effect
Offline E_T Requirement	up	unknown
Particle Tagging Inefficiency	up	unknown
High-$\Delta\eta$ η_{boost} Bias	up	Appendix A
Jet E_T Distribution	unknown	assumed small
Level 1 Trigger	down	Appendix A
Jet Position (η) Uncertainty	down	assumed small
Particle η Smearing	down	assumed small
Jet Energy Scale Uncertainty	down	negligible
Spurious Jets	down	negligible
Multiple Interaction Contamination	down	$\leq 5\%$
Calorimeter Noise Contamination	down	$\leq 5\%$
"Hot" Channel Contamination	down	$\leq 5\%$
High-$\Delta\eta$ Acceptance Loss	down	$\lesssim 20\%$
Out-of-cone Effects	down	$\lesssim 30\%$

Table 7-3: Systematic biases in the measurement of the rapidity gap fraction. For each bias, the expected size and direction of its effect is shown, compared to an unbiased gap fraction measurement.

Chapter 8

Results

The experimental gap fraction measurement is used to place on upper limit on the fraction of events with no particles between the jets for $\Delta\eta_c > 3$. In order to obtain a valid upper limit, all effects that bias the measured value to a lower value either must be corrected for or included in the systematic error on the gap fraction.

8.1 Corrected Experimental Gap Fraction

Systematic biases that reduce the measured gap fraction for $\Delta\eta_c > 3$ are summarized in Table 8-1. The corrections for these biases are given below:

- **Contamination Effects:** Contamination from gap events from multiple interactions, calorimeter noise, and "hot" calorimeter cells is corrected for before determining the upper limit. The largest possible effect of these biases results in a combined correction factor of 1.17.

- **High-$\Delta\eta$ Trigger Acceptance Loss:** The acceptance loss in the high-$\Delta\eta$ trigger is not a concern for sufficiently small $\Delta\eta_c$ bins. However, in order to obtain an upper limit for $\Delta\eta_c > 3$, the acceptance loss must be corrected for. The correction factor for the acceptance loss is 1.05 ± 0.09. The error is due to the increased statistical error introduced by the acceptance correction.

Origin of Bias	Size of Effect
Multiple Interaction Contamination	$\leq 5\%$
Calorimeter Noise Contamination	$\leq 5\%$
"Hot" Channel Contamination	$\leq 5\%$
High-$\Delta\eta$ Acceptance Loss	5%
Out-of-cone Effects ($R = 1.5$)	$(27 \pm 3)\%$

Table 8-1: Systematic biases affecting the upper limit on the rapidity gap fraction.

- **Out-of-cone Effects:** The out-of-cone effect determined in §7.2.7 is used to correct the gap fraction for both out-of-cone calorimeter showering and out-of-cone radiation in color-singlet events. The out-of-cone effect obtained for $R = 1.5$ is used since this radius is large enough to contain the out-of-cone showering (see §6.2.3). This gives a correction factor of 1.36 ± 0.05.

These corrections are applied to the measured gap fraction (§7.1.5) to obtain a corrected gap fraction of $f(\Delta\eta_c > 3)^{exp}_{corr} = (9.4 \pm 1.3^{(stat)} \pm 0.4^{(sys)}) \times 10^{-3}$, where the systematic error is due only to the out-of-cone correction. It should be noted that this value is not a true measurement of the experimental gap fraction due to the conservative corrections; it is used only to obtain an upper limit on the true gap fraction.

8.2 Upper Limit

The corrected experimental gap fraction is used to place an upper limit on the fraction of events with no particles between the jets. The upper limit obtained for $\Delta\eta_c > 3$ is

$$f(\Delta\eta_c > 3) \quad < \quad 1.1 \times 10^{-2}$$

at the 95% confidence level.

8.3 Interpretation of Upper Limit

This upper limit puts a constraint on the product of σ_{gap}/σ and S for $\Delta\eta_c > 3$:

$$\frac{\sigma_{gap}}{\sigma} \cdot S \quad < \quad 1.1 \times 10^{-2}.$$

Figure 8-1 shows the values of σ_{gap}/σ and S excluded by the upper limit. Also shown is the theoretical estimate for σ_{gap}/σ assuming a QCD color-singlet [3] and the range of expected values for the survival probability S [8]. Although the theoretical predictions are subject to large uncertainties, this limit provides a significant constraint on the possible values, independent of the indeterminate contribution from color-octet exchange and the background from particle detection inefficiencies.

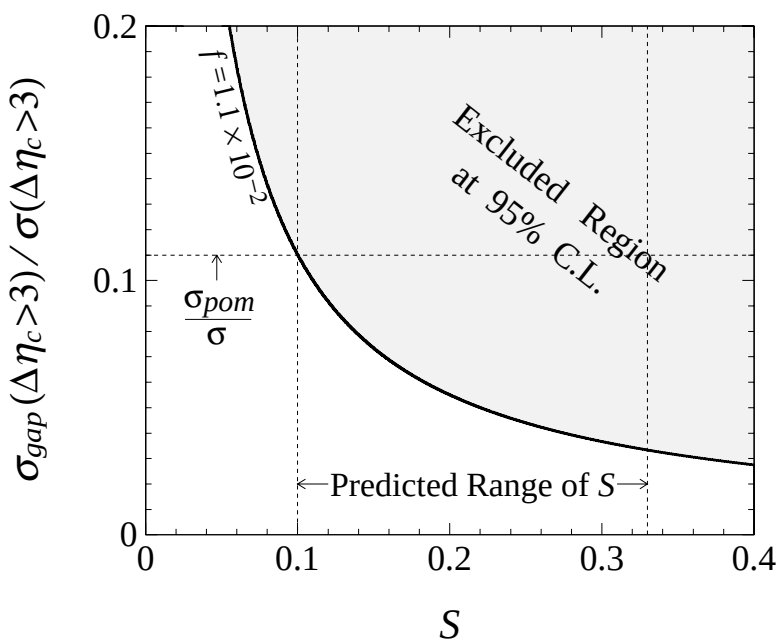

Figure 8-1: A plot of σ_{gap}/σ versus S for $\Delta\eta_c > 3$ showing the values excluded by the upper limit (shaded region). The horizontal line shows the estimated value of σ_{gap}/σ assuming Pomeron exchange [3], while the vertical lines show the predicted range of S [8].

Chapter 9

Conclusions

This dissertation expands substantially upon the first published experimental results on rapidity gaps between jets by the DØ Collaboration [7]. Although color-singlet exchange in jet events has not been unambiguously observed, this work contains a comprehensive analysis leading to an important upper limit on rapidity gap "production" between jets. This non-trivial measurement adds significantly to our limited understanding of particle production from both spectator interactions and hadronization in hard scattering jet events.

The DØ detector has provided an excellent means to make this measurement since it possesses the two elements essential for measuring rapidity gaps between jets: large jet pseudorapidity acceptance and sufficient low energy particle detection. DØ's comprehensive trigger system allowed a significant sample of jet events with a large pseudorapidity separations between the jets to be obtained for this analysis. Without a special trigger a much less restrictive upper limit would have been obtained.

The experimental rapidity gap sample obtained in this analysis has been shown to have very different characteristics from an inclusive event sample. Gap events have significantly reduced hadronic calorimeter energy deposition and very few charged particle tracks between the jets. In addition, the events contain very few jets compared to the inclusive sample, with the leading two jets being more back-

to-back than in typical jet events. These properties confirm that the experimental gap events contain very little energy flow between the jets, as expected from color-singlet exchange.

Although the experimental gap sample is interesting in itself, a measurement of the rapidity gap fraction allows comparison to theoretical predictions. The experimental gap fraction measured in this dissertation is shown to have the qualitative behavior expected for color-singlet exchange, i.e. a flattening for large jet separations. Comparison with a color-octet enhanced gap fraction measurement indicates that the flattening may indeed be evidence for color-singlet exchange. Unfortunately, it is not possible to positively draw this conclusion due to uncertainties in the color-octet contribution and background from particle detection inefficiencies.

While the experimental gap fraction shows qualitative agreement with color-singlet exchange, quantitative comparison with theory is only possible by determining an upper limit on the true gap fraction, i.e. the fraction of events with no particles between the jets. A large portion of the analysis has dealt with understanding the systematic effects on the experimental gap fraction due to the trigger biases, offline cuts, instrumental effects, and various physical processes. Effects that increase the observed value, such as particle detection inefficiencies, can not be corrected for without detailed understanding of the underlying particle multiplicities. However, these effects are not important for determining an upper limit. In contrast, effects that decrease the observed value, such as particle contamination between the jets, have been accounted for in order to determine a valid upper limit.

The upper limit obtained in this dissertation (and Ref. [7]) provides the first experimental information on σ_{gap}/σ and S. The limit significantly constrains the range of values for these quantities, but does not exclude a strongly interacting color-singlet (two-gluon Pomeron) exchange process. It does, however, provide

an improved understanding of hadronization between jets and particle production from spectator interactions in proton-antiproton collisions.

In conclusion, these first results should provide an incentive for both theorists and experimentalists to obtain additional information on color-singlet exchange and rapidity gap production between jets. However, further analysis of the data described in this dissertation already is providing more convincing evidence for a strongly interacting color-singlet in jet events [70, 71].

Appendix A

Possible Trigger Biases in the Gap Fraction Measurement

As mentioned in Chapter 7, the triggers may indirectly affect the observed rapidity gap fraction. The trigger biases can affect the measured gap fraction due to its expected dependence on parton distribution functions as derived by Del Duca and Tang [35] (see §2.10.2). They calculate the gap probability

$$R(\mu) = \frac{\sigma_{gap}(\mu)}{\sigma_{tot}} \equiv \frac{\sigma^{sing} + \sigma^{oct}_{gap}(\mu)}{\sigma_{tot}} \tag{A.1}$$

where σ^{sing} is the cross section for two-gluon color-singlet BFKL Pomeron [26] exchange, $\sigma^{oct}_{gap}(\mu)$ is the cross section for color-octet exchange with no parton radiation with $p_T > \mu$ between the jets, and σ_{tot} is the inclusive jet cross section.

This equation can be rewritten in terms of the partonic cross sections:

$$R(\mu; x_1, x_2) = w(x_1)w(x_2)\frac{\hat{\sigma}^{sing}}{\hat{\sigma}_{tot}} + \frac{\hat{\sigma}^{oct}_{gap}(\mu)}{\hat{\sigma}_{tot}},$$

where w is the relative weight of parton distribution functions,

$$w(x) = \frac{G(x) + (\frac{4}{9})^2 \sum_f Q_f(x)}{G(x) + \frac{4}{9} \sum_f Q_f(x)}.$$

The trigger biases only affect the measured value if the QCD color-singlet (BFKL Pomeron) exists, that is $\sigma^{sing} > 0$.

To illustrate the maximum potential effect, the color-octet contribution is assumed to be negligible (i.e. $\mu \to 0$):

$$R(\mu; x_1, x_2) \quad = \quad w(x_1)w(x_2)\frac{\hat{\sigma}^{sing}}{\hat{\sigma}_{tot}}.$$

Therefore, trigger conditions that change the relative weights of the quark and gluon distribution functions can bias the measurement.

A.1 Parton Distribution Functions

The parton distribution functions which enter into Eq. 2.5 depend on both x and the energy scale Q^2 of the hard partons. For this study the KMRS B0-190 parton distribution functions are used with $Q^2 = p_T^2/2$. The partons are fixed at $p_T = 30\,\mathrm{GeV}$.

Figure A-1 shows the ratio of quarks (all flavors) to gluons (for a single jet) as a function of $\Delta\eta_c$ for several values of $\eta_{boost} = \eta_1 + \eta_2$. For small $\Delta\eta_c$ gluons are dominant, while for large $\Delta\eta_c$ the quark distribution function becomes dominant.

A.2 Trigger Biases

There are two trigger biases that can cause a bias in the parton distribution functions. One can arise from the level 1 trigger requirements which can cause a bias towards quarks jets. The other occurs in the high-$\Delta\eta$ trigger which is biased towards small values of η_{boost}. These potential biases are discussed in greater detail below.

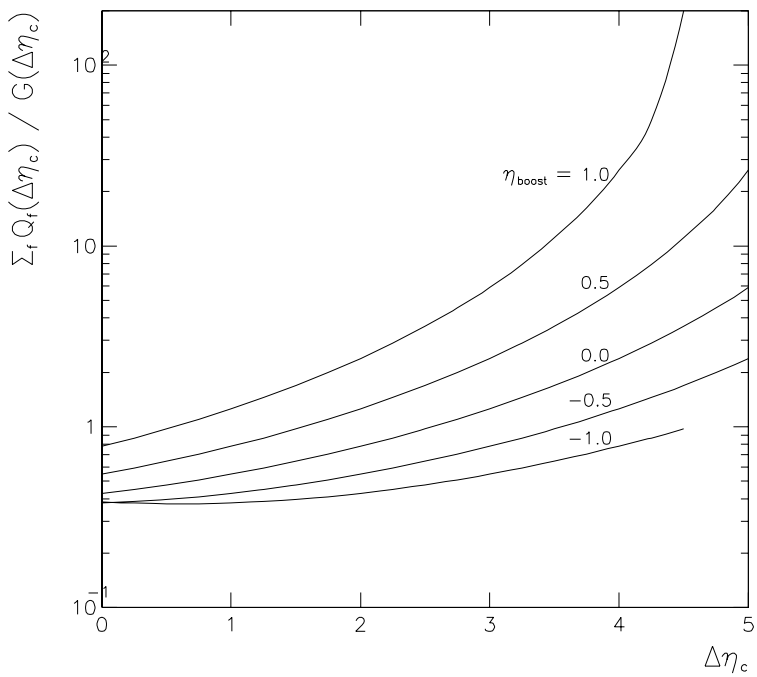

Figure A-1: The ratio of quark (all flavors) to gluon jets as a function of $\Delta\eta_c$ for several values of η_{boost}. The KMRS D0-190 parton distribution functions are used with $Q^2 = p_T^2/2$ and $p_T = 30$ GeV.

A.2.1 Level 1 Trigger Bias

As discussed in §5.3.2 (see Fig. 5-7), the level 1 trigger can bias the trigger towards quark jets when the trigger is not fully efficient. Although the bias is not well determined for the triggers used in this analysis, it is instructive to determine the potential effect on the measured gap fraction.

The quark trigger bias β is the trigger enhancement of the quarks compared to gluons: $\beta = \epsilon_q/\epsilon_g$, where ϵ_i is the efficiency for triggering on a jet originating from a parton with flavor i. Any bias ($\beta \neq 1$) affects the initial parton distribution by artificially weighting the quark distribution, resulting in the relative weight of parton distribution functions w given by

$$w(x) \quad = \quad \frac{G(x) + (\frac{4}{9})^2\beta \sum_f Q_f(x)}{G(x) + \frac{4}{9}\beta \sum_f Q_f(x)}.$$

Therefore, for a quark bias ($\beta > 1$), the quark distribution is enhanced leading to a different cross section for color-singlet exchange.

The effect of a quark bias on the measured gap fraction can be illustrated by plotting $w(x_1)w(x_2)_\beta / w(x_1)w(x_2)_{\beta=1}$ for various values of $\beta > 1$. Figure A-2 shows the resulting effect on the measured gap fraction assuming $\eta_{boost} = 0$. For small quark biases, the effect is negligible for all $\Delta\eta_c$, while for larger biases the effect becomes substantial, especially for large $\Delta\eta_c$.

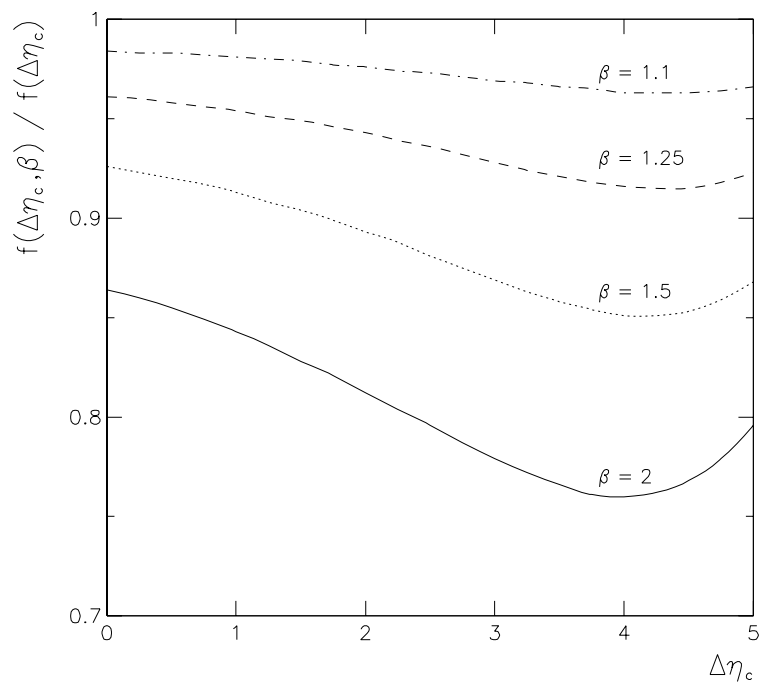

Figure A-2: The effect of a quark bias on the measured gap fraction as a function of $\Delta\eta_c$ for several values of β.

The maximum effect on the measured gap fraction occurs for $\eta_{boost} = 0$ and is reduced for $\eta_{boost} \neq 0$. The maximum effect on the measured gap fraction as a function of β is shown in Fig. A-3.

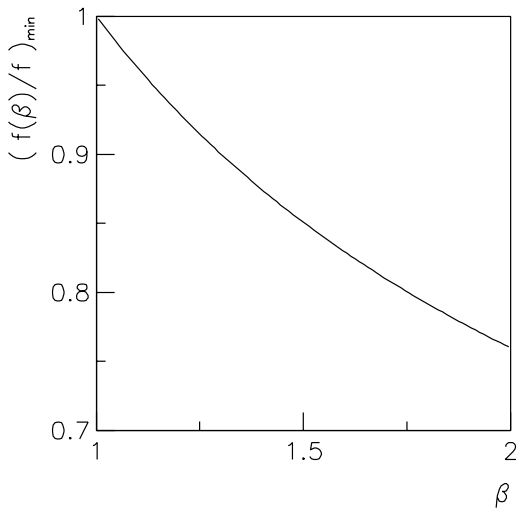

Figure A-3: The maximum effect of a quark bias on the measured gap fraction as a function of β.

A.2.2 High-$\Delta\eta$ Trigger η_{boost} Bias

As mentioned in §5.3.2, the high-$\Delta\eta$ trigger is biased towards events with small η_{boost} compared to the inclusive trigger. However, this bias results in an increase in the gap fraction and is not a concern for the upper limit. Figure A-4 shows the effect of η_{boost} on the measured gap fraction. Larger $|\eta_{boost}|$ values result in a decreased measured gap fraction compared to smaller values.

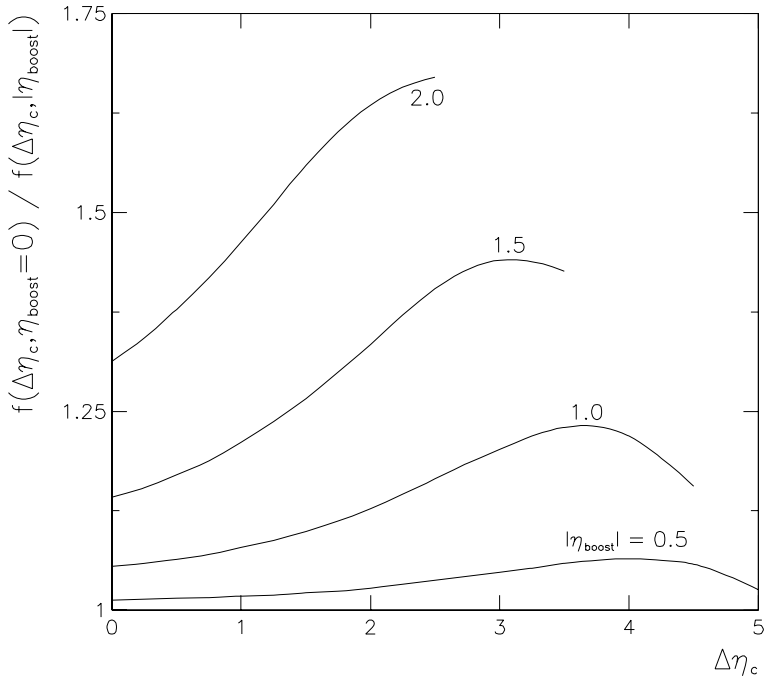

Figure A-4: The effect of η_{boost} on the measured gap fraction as a function of $\Delta\eta_c$.

REFERENCES

[1] M. Derrick *et al.* (Zeus Collaboration), Phys. Lett. **B315**, 481 (1993).

[2] Y. Dokshitzer, V. Khoze and S. Troyan, "Proceedings of the 6th International Conference on Physics in Collisions" (1986), ed. M. Derrick, 417 (World Scientific, Singapore, 1987);
Y. Dokshitzer, V. Khoze and T. Sjöstrand, Phys. Lett. **B274**, 116 (1992).

[3] J. D. Bjorken, Phys. Rev. **D47**, 101 (1992).

[4] R. S. Fletcher and T. Stelzer, Phys. Rev. **D48**, 5162 (1993).

[5] H. Chehime and D. Zeppenfeld, MAD/PH/814 (1994).

[6] A. Brandt *et al.* (UA8 Collaboration), Phys. Lett. **B297**, 417 (1992).

[7] S. Abachi *et al.* (DØ Collaboration), Phys. Rev. Lett. **72**, 2332 (1994).

[8] E. Gotsman, E. M. Levin and U. Maor, Phys. Lett. **B309**, 199 (1993).

[9] V. Barger and R. Phillips, *Collider Physics*, p. 155 (1987).

[10] J. Collins, D. Soper and G. Sterman, "Factorization of Hard Processes in QCD", in *Perturbative Quantum Chromodynamics*, ed. A.H. Mueller, p. 1 (1989).

[11] S. Ellis, Z. Kunzst and D. Soper, Phys. Rev. Lett. **69**, 1496 (1992); Phys. Rev. Lett. **64**, 2121 (1990); Phys. Rev. **D40**, 2188 (1989); Phys. Rev. Lett. **62**, 726 (1989).

[12] R. Field, *Applications of Perturbative QCD*, p. 93 (1989).

[13] Y. Dokshitzer, V. Khoze, A. Mueller and S. Troyan, *Basics of Perturbative QCD*, p. 91 (1991).

[14] B. Andersson *et al.*, Z. Phys. **C20**, 317 (1983); Phys. Rep. **97**, 33 (1983); Phys. Lett. **B94**, 211 (1980).

[15] G. Arnison *et al.* (UA1 Collaboration), Phys. Lett. **172**, 461 (1986); Phys. Lett. **177**, 244 (1986); Nucl. Phys. **B276**, 253 (1986); CERN EP/85-196 (1985).

[16] J. Huth *et al.* (Snowmass Jet Accord), "Proc. of the 1990 Summer Study on HEP", 134 (1990).

[17] R. Astur, "QCD Physics with the k_T Jet Algorithm", DØNote 2163 (1994) (unpublished).

[18] W. Bartel *et al.* (JADE Collaboration), Phys. Lett. **B134**, 275 (1984); Phys. Lett. **B101**, 129 (1981);
H. Aihara *et al.* (TPC Collaboration), Phys. Rev. Lett. **54**, 270 (1985); Z. Phys. **C28**, 31 (1985);

[19] G. Gustafson, Phys. Lett. **B175**, 453 (1986);
G. Gustafson and U. Pettersson, Nucl. Phys. **B306**, 746 (1988).

[20] L. Lonnbald and U. Pettersson, LU-TP 88-15.

[21] T. Regge, Nuovo Cimento **14**, 951 (1959).

[22] G. Ingelman and P. Schlein, Phys Lett. **B152**, 256 (1985).

[23] G. Alner *et al.* (UA5 Collaboration), Phys. Rep. **154**, 247 (1987).

[24] F. Abe *et al.* (CDF Collaboration), Phys. Rev. **D41**, 2330 (1990).

[25] F. Low, Phys. Rev. **D12** 163 (1975);
S. Nussinov, Phys. Rev. **D14** 246 (1976);
N. Nikolaev and B. Zakharov, DFTT-5/91 (1991) and references therein;
E. Berger, J. Collins, G. Sterman and D. Soper, Nucl. Phys. **B286**, 704 (1987).

[26] Ya. Balitsky and L. Lipatov, Sov. J. Nucl. Phys. **28**, 822 (1978);
L. Lipatov, Sov. Phys. JETP **63**, 904 (1986).

[27] J. D. Bjorken, Phys. Rev. **D45**, 4077 (1992).

[28] H. Chehime *et al.*, Phys. Lett. **B286**, 397 (1992).

[29] P. Abreu *et al.* (DELPHI collaboration), Z. Phys **C50**, 185 (1991);
P.D. Acton *et al.* (OPAL collaboration), Z. Phys **C53**, 539 (1992).

[30] E. Malaza and B. Webber, Nucl. Phys. **B267**, 702 (1986);
B. Andersson, P. Dahlqvist and G. Gustafson, Phys. Lett. **B214**, 604 (1988).

[31] K. Fialkowski, B. Wosiek and J. Wosiek, Acta Phys. Pol. **B20**, 639 (1989);
I. Dremin, submitted to Physics Uspekhi, FIAN TD-6, (1994).

[32] H. Bengtsson and T. Sjöstrand, Comput. Phys. Commun. **46**, 43 (1987).

[33] T. Sjöstrand and M. van Zijl, Phys Rev. **D36**, 2019 (1987).

[34] R.S. Fletcher, private communication.

[35] V. Del Duca and W. K. Tang, SLAC-PUB-6310 (1993).

[36] L. Lipatov, Sov. J. Nucl. Phys. **23**, 338 (1976);
E. Kuraev, L. Lipatov and V. Fadin, Sov. Phys. JETP **44**, 443 (1976); Sov. Phys. JETP **45**, 199 (1977).

[37] S. Abachi *et al.* (DØ Collaboration), Nucl. Instrum. and Meth. **A338**, 185 (1994).

[38] F. Abe *et al.* (CDF Collaboration), Nucl. Instrum. and Meth. **A271**, 387 (1988).

[39] A. Clark *et al.*, CONF-8806235-8-mc (microfiche), 1988.

[40] A radiation length corresponds to the effective thickness of material that causes an electromagnetic particle to lose all but $1/e$ of its energy through bremsstrahlung.

[41] The interaction length for hadronic showers corresponds to the effective thickness of material that causes a hadron to lose all but $1/e$ of its energy.

[42] S. Abachi *et al.* (DØ Collaboration), Nucl. Instrum. and Meth. **A324**, 53 (1993).

[43] A. Jonckeere, "Proceedings of the Argonne National Laboratory Detector Simulation Workshop" (1987); DØNote 638 (1987) (unpublished).

[44] M. Bhattacharjee, private communication.

[45] F. Nang and R. Partridge, "Level 0 Detector Layout", DØNote 998 (1990) (unpublished);
J. Bantly *et al.*, "The Level 0 Trigger for the DØ Detector", DØNote 1996 (1993) (unpublished).

[46] R. Astur and H. Weerts, "Level 1 Jet Trigger and Level 2 Jet Tool", DØNote 1044 (1990) (unpublished).

[47] N. Hadley, "Cone Algorithm for Jet Finding", DØNote 904 (1989) (unpublished).

[48] R. Avery, private communication.

[49] Q. Li-Demarteau, private communication.

[50] A. Milder, Ph.D. Dissertation, University of Arizona (1993) (unpublished).

[51] F. Paige and S. Protopopescu, "ISAJET", BNL-31987.

[52] D. Elvira, Ph.D. Dissertation, Universidad de Buenos Aires (1994) (unpublished).

[53] G. Marchesini and B.R. Webber, Nucl. Phys. **B310**, 461 (1988); Nucl. Phys. **B330**, 261 (1988);
I. G. Knowles, Nucl. Phys. **B310**, 571 (1988);
G. Abbiendi, *et al.*, Comp. Phys. Comm. **67**, 465 (1992).

[54] R. Astur, "Study of Fake Jets in the DØ Detector", DØNote 1662 (1993) (unpublished).

[55] R. Astur, J. Blazey and D. Elvira, "A Study of Standard Jet Cuts and their Efficiencies Using DØ Collider Data", DØNote 1763 (1993) (unpublished).

[56] B. Kehoe, "Resolution Bias in Jet Response Measurement", DØNote 2052 (1994) (unpublished).

[57] B. Kehoe, R. Astur, J. Yu, " Jet Response from the Missing E_T Projection Fraction", DØNote 2053 (1994) (unpublished).

[58] F. Abe *et al.* (CDF Collaboration), Phys. Rev. Lett. **69**, 2896 (1992).

[59] B. Kehoe, private communication.

[60] G. Alexander *et al.* (OPAL Collaboration), Phys. Lett. **B265**, 462 (1991).

[61] B. May and G.E. Forden, "Fragmentation Dependence of Level 1 Jet Trigger Efficiencies", DØNote 1475 (1992) (unpublished).

[62] T. Sjöstrand, CERN-TH.7112/93 (1993).

[63] J. Bantly, "Multiple Interaction Tool Study", DØNote 1849 (1993) (unpublished).

[64] J. Kotcher, Ph.D. Dissertation, New York University (1992) (unpublished).

[65] D. Owen, private communication.

[66] J. Borders, Ph.D. Dissertation, University of Rochester (1994) (unpublished).

[67] B. Hirosky, private communication.

[68] F. Abe *et al.* (CDF Collaboration), Phys. Rev. Lett. **61**, 1819 (1988).

[69] K. Hikasa *et al.* (Particle Data Group), "Review of Particle Properties", Phys. Rev. **D45**, Part II (1993).

[70] A. Brandt and T. Taylor, private communication.

[71] B. May (for the DØ Collaboration), submitted to "Proceedings of the 8th Meeting of the American Physical Society, Division of Particles and Fields '94" (Albuquerque, 1994); AZ-PH/EXP-02 (1994); DØNote 2243 (1994).